Accelerated Monte Carlo simulation for scatter correction in SPECT

Hugo de Jong

Colophon

This book was typeset by the author using LaTeX2$_\varepsilon$.

ISBN 90–393–2870-6

Printed by Febodruk BV, Enschede.

ACCELERATED MONTE CARLO SIMULATION FOR SCATTER CORRECTION IN SPECT

VERSNELDE MONTE CARLO SIMULATIE
VOOR VERSTROOIINGSCORRECTIE IN SPECT
(MET EEN SAMENVATTING IN HET NEDERLANDS)

PROEFSCHRIFT

TER VERKRIJGING VAN DE GRAAD VAN DOCTOR AAN DE UNIVERSITEIT UTRECHT
OP GEZAG VAN DE RECTOR MAGNIFICUS, PROF. DR. W. H. GISPEN, INGEVOLGE
HET BESLUIT VAN HET COLLEGE VOOR PROMOTIES IN HET OPENBAAR TE
VERDEDIGEN OP VRIJDAG 30 NOVEMBER 2001 DES MIDDAGS TE 2:30 UUR

DOOR

HUGO WILHELMUS ANTONIUS MARIA DE JONG

GEBOREN OP 16 JULI 1973 TE BERKEL ENSCHOT

Promotor: **Prof. dr. ir. M. A. Viergever**
Universitair Medisch Centrum Utrecht

Co-promotoren: **Dr. F. J. Beekman**
Universitair Medisch Centrum Utrecht

Dr. P. P. van Rijk
Universitair Medisch Centrum Utrecht

The research described in this thesis was carried out at the Image Sciences Institute, University Medical Center Utrecht (Utrecht, The Netherlands), under the auspices of ImagO, the Graduate School for Biomedical Image Sciences.

Financial support for publication of this thesis was kindly provided by TYCO Healthcare/Mallinckrodt, ADAC laboratories, Siemens Medical Systems, Röntgen Stichting Utrecht, Le Jeune Maisons des Vacances, ImagO and Utrecht University.

Contents

Abbreviations

1D	one-dimensional
2D	two-dimensional
3D	three-dimensional
SPECT	single photon emission computed tomography
ECT	emission computed tomography
CT	computed tomography
PET	positron emission tomography
DI	dual isotope
Tc-99m	technetium
Tl-201	thallium
MBq	megabecquerel = 27.03 μCi
mCi	millicurie = 37 MBq
VXHR	Vertex extra high resolution (collimator)
LEGP	low energy general purpose (collimator)
MC	Monte Carlo
UMCS	Utrecht Monte Carlo System
RMC	rotation-based Monte Carlo
FD	forced detection
CFD	convolution-based forced detection
pdf	probability distribution function
VRT	variance reduction technique
pixel	picture element
voxel	volume element
PSF	point source function
SDSE	slab derived scatter estimation
NaI	sodium iodine (crystal)
Pb	Lead
MCAT	mathematical cardiac antromorphic thorax
FWHM	full width at half maximum
FWTM	full width at tenth maximum
NMSE	normalized mean square error
NSD	normalized standard deviation
SNR	signal to noise ratio

Chapter 1

Introduction

1.1 Motivation

Single Photon Emission Computed Tomography (SPECT) is one of the major methods to visualize and analyze the distribution of radio-labelled bio-molecules (radio-pharmaceuticals) in patients. SPECT is based on the detection of single gamma photons that are emitted from a radio-pharmaceutical; these photons are generally in the energy range of several tens to a few hundred keV. SPECT images mainly portray functional properties of organs and tissues by the aid of associated distributions of radio-pharmaceutical molecules. For example, SPECT is able to non-invasively measure organ perfusion, metabolic function, receptor density and drug delivery. Important clinical areas for SPECT imaging are cardiology, neurology and oncology. For instance, the objective in cardiac SPECT is to assess regional or global ventricular function, and the severity of perfusion defects and viability of the myocardium. The radio-pharmaceuticals are generally administered to the patient by injection, where after tomographic images can be reconstructed from projection data acquired at discrete angles around the patient. The quality of the reconstructed SPECT image is degraded by factors such as photon attenuation, collimator blurring and the detection of scattered photons. To obtain high-quality and quantitatively accurate SPECT images, correction for these image-degrading factors by including a physical model of the formation of the projections during SPECT reconstruction. To achieve higher quantitive accuracy, scatter models are proposed in the first part of this thesis.

The second part of this thesis is focussed on a special topic in cardiac SPECT. Various cardiac SPECT protocols are clinically used nowadays, of which many involve a separate SPECT acquisition of the patient in rest and under stress. A relatively new and promising protocol is simultaneous Tc-99m/Tl-201 Dual-Isotope cardiac SPECT. In this protocol the rest and stress images are acquired in one scan, which has some interesting advantages over sequential protocols. Patients, for instance, spend less time in the imaging department, a factor which reduces costs and patient waiting lists. Furthermore, patient discomfort is reduced, which helps to prevent motion artifacts in the images, and the rest and stress image are perfectly registered. However, down-scatter of Tc-99m photons into the Tl-201 image is a significant problem in this protocol. Reduction of this down-scatter will be the main focus of the second part of the thesis.

1.2 SPECT

A SPECT scanner uses a *gamma camera* to detect the photons emitted from the radio-pharmaceutical. The modern gamma camera (fig.1.1) consists of a collimator, a large-area NaI(Tl) crystal, a light guide for optically coupling the photo-multipliers to the crystal and circuits for position encoding and pulse-height analysis. The entire camera is surrounded by a lead shield in order to prevent the measurement of background radiation from outside the field of view of the camera.

Most SPECT systems consist of one or more gamma cameras which are mounted on a frame in such a way that they can rotate around the patient. The data required for the reconstruction of the source distribution are obtained by the acquisition of planar gamma camera images at a sufficient number of angles around the patient. Because of the large field of view of these scintillation cameras (typically 40×50 cm), a large part of the patient can be examined in one scan. Since the scintillation detectors used in this modality are incapable of determining the direction of the incoming photons, SPECT system cameras are always provided with a collimator. A collimator is usually a slab of lead with several tens of thousands of holes covering the entire detector surface. These holes are typically a few centimeter long and a few millimeter in diameter. Since few photons are able to traverse the lead, it is mainly the photons traversing the holes which are detected. The elongated geometry of the holes ensures that the direction of the detected photons is well determined. This information is essential in order to reconstruct the distribution of the radio-pharmaceuticals. Unfortunately, this directional information is achieved at great cost, namely a tremendous loss of sensitivity (number of detected photons). The typical sensitivity of a gamma camera is 5×10^{-4}, meaning that 5 out of 10,000 emitted photons will actually traverse the collimator and be detected. Accordingly, collimation is the major reason why counting statistics in SPECT images are poor.

1.2.1 Scintillation Detection

Scintillation detection is currently the main technique for γ-radiation detection in nuclear medicine imaging. It is based on the emission of visible or near-visible light from scintillation crystals when energy is absorbed from ionizing radiation. This emission of light is a result of inelastic collisions between secondary electrons and other atomic electrons. The photo-multipliers (PM) tubes amplify the light and convert it into electrical pulses.

A property of many inorganic scintillators is that the light emission is proportional to the energy deposit in the material. This allows the energy of the detected photons to be measured. A typical value of the energy resolution of scintillation detectors used in modern gamma cameras is about 10% for photon energies of 100-200 keV [110]. This means one can discriminate only to a limited extent by applying a photo-peak window, between unscattered photons (*primary photons*) and photons which have scattered and have thereby lost energy. So that a large fraction of primary photons can be collected, the width of this window is normally 15-20% of the photo-peak energy. As a consequence, a significant part of the photons detected in the photo-peak window, have undergone scattering.

1.2.2 Collimation

Because each clinical study has different requirements field of view (FOV), the choice of radio-pharmaceutical and associated dose, the best method for collimation differs for each type of study. Therefore several types of collimators have been developed to achieve an adequate compromise between spatial resolution, sensitivity and accuracy. For the studies described in this thesis we use the *parallel-hole collimator*, which is the most widely used collimator in nuclear medicine. This collimator is suitable for almost all studies and permits the use of relatively simple and fast reconstruction techniques. Other collimator types include fan-beam, cone-beam and pin-hole collimators.

1.2.3 Image degrading effects in SPECT

The detection of photons in SPECT is seriously affected by collisions of the photons with atoms inside the patient (photon attenuation and scatter), and the inevitable inaccuracy of the collimator used (collimator blurring). The images are also severely degraded because of noise, partly due to the Poisson nature of the photon emission. Accordingly, it is very difficult to obtain high quality and quantitative accurate SPECT images. As will be shown in the following subsections, each factor is a well understood physical phenomenon, and therefore corrections can be made for each of these image degrading effects during reconstruction.

Collimator blurring

Because collimator holes are not infinitely narrow, the photons that traverse the collimator will not all come from a direction that is exactly aligned with the holes. This leads to a substantial loss of resolution in the gamma-camera images and in the reconstructions. The acceptance angle of a collimator is defined by the fraction of the hole size and the hole diameter. Although decreasing the acceptance angle would decrease the collimator blurring, it would also greatly decrease the sensitivity of the collimator. It can be shown that a twofold increase of the collimator resolution, would decrease the sensitivity by a factor of about 4. Therefore, a compromise has to be found between collimator resolution and sensitivity. Since the collimator resolution depends almost linearly on the distance between the source and the camera, it is important to position the camera as close as possible to the patient. Accurate mathematical descriptions of collimator blurring can be found in [90, 114, 115].

Photon interaction with matter

An important image degrading effect in SPECT is the scattering of photons in tissue. Scatter results in the detection of 'incorrect' photons and is also the cause of the attenuation effect. These effects are explained in Fig. 1.1.

A photon can penetrate matter without interaction, it can be absorbed and it can scatter and thereby lose a certain amount of energy. If a photon is scattered and then detected in the photo-peak energy window, this may lead to detection at a detector position which suggests an incorrect emission point (e.g. photon 4 in Fig. 1.1). This causes severe

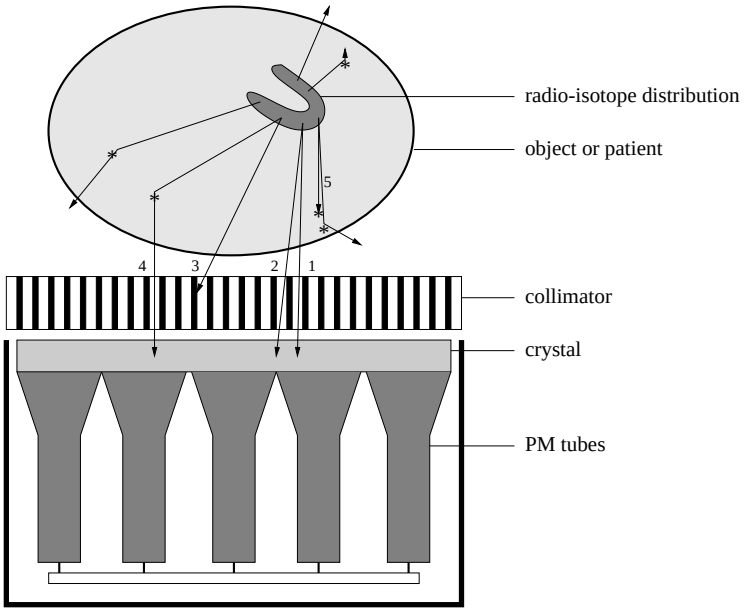

Figure 1.1: Schematic view of acquisition of a projection using a gamma camera. The scatter interactions in the patient are represented by $*$. Photon 1 and 2 are directly detected, although photon 2 under a slight angle from the collimator hole axis, causing blurring of the projection. Photon 3 is rejected by the collimator. Photon 4 is detected after scattering. Photons 5 are not detected due to scatter and absorption which causes the attenuation effect.

degradation of the contrast and quantitative accuracy of the reconstructed image if scatter events are not corrected for.

The interactions of photons with matter are described mainly by four processes: photo-electric absorption, Compton scattering, coherent scattering and pair production [110]. Each process will occur with a probability which strongly depends on parameters like photon energy, the electron density of the material or the differential cross-section per atom. The total probability for the occurrence of any of the processes is therefore the sum of the cross-sections. Figure 1.2 shows the cross-sections of the aforementioned interactions and the total cross-section. From Fig. 1.2 it is clear that for photons with an energy of 50-1000 keV, the most probable interaction process is Compton scattering. In heavier materials such as the collimator lead and at at low energies below 100 keV, photo-electric absorption also becomes significant. Hence only Compton scattering and photo-electric absorption need to be modeled for an accurate description of photon interaction in SPECT.

Compton Scattering *Compton scattering* is an interaction between a photon and an atomic electron. Since the energy of the incoming photon is very high compared to the binding energy of the electron, the interaction can be interpreted as a collision between

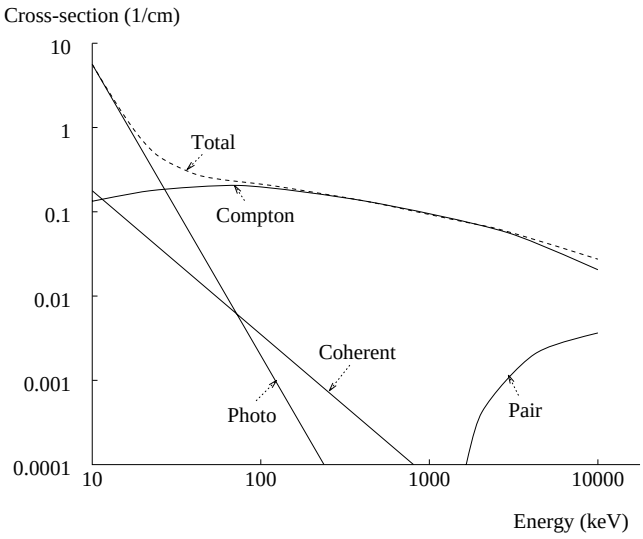

Figure 1.2: Differential cross-sections of the photo-electric effect, Compton scattering, coherent scattering and pair production and total cross-section for H_2O as a function of photon energy.

the photon and a free electron.

The photon is scattered by an angle θ relative to its incident direction and loses energy which is then transferred to the electron. The scattered photon energy E_{sc} is given by the Compton formula [28]:

$$E_{sc} = \frac{E_0}{1 + \frac{E_0}{m_0 c^2}(1 - \cos\theta)} \tag{1.1}$$

where E_0 is the incident photon energy and $m_0 c^2$ is the rest energy of the electron. From eq.(1.1) it is evident that the maximum amount of energy is transferred to the electron when the photon is backscattered ($\theta = 180^\circ$) and that little energy is lost by the photon when $\theta \approx 0^\circ$. The angular distribution can be described by the Klein-Nishina formula, which relates the differential cross-section $\frac{d\sigma}{d\Omega}$, or scatter probability, to the scatter angle θ. A comprehensive description of Compton scatter is given in Evans [42].

Photo-electric interaction When a photo-electric interaction occurs, the energy of the photon is transferred completely to the atomic electron. If the energy of the incoming photon is higher than the binding energy of the electron, the electron can be ejected from the electron shell (most often the K-shell). This results in a vacancy in the electron shell, which will be filled rapidly by an electron from one of the outer shells. The difference in binding energy between the two electron shells can be emitted as a characteristic X-ray photon. Characteristic X-ray emission is more probable for high-Z materials, such as lead (Pb-82). The binding energy of the lead K-shell is 88 keV and the energies of the

relevant characteristic X-rays (Pb X-rays) are 75 keV, 73 keV and 85 keV. For instance, this can result in the absorption of a 140 keV causing the emission and possible detection of an x-ray with much lower energy. This is important in simultaneous Tc-99m/Tl-201 dual-isotope SPECT in which two energy windows are used (see section 1.4.2).

Attenuation

Another effect of scattering is that many photons are diverted on their way to the detector (see photon 2 in Fig. 1.1); this causes *attenuation* of the photon flux directed towards the detector. Attenuation is mainly the result of Compton scattering (and some photo-electric interaction) and depends on the total length of the tissue which has to be traversed and on the type of tissue involved. The attenuation of a narrow beam of photons passing through a non-homogeneous medium of thickness d is given by

$$\Psi = \Psi_0 \exp\left(-\int_0^d \mu(r)\, dr\right) \tag{1.2}$$

where Ψ is the photon flux after attenuation, Ψ_0 is the incident photon flux and $\mu(r)$ is the linear attenuation coefficient (the total sum of all possible differential cross-sections). For water, the linear attenuation coefficient μ_l is approximately 0.152 cm^{-1} for 140 keV gamma rays [89].

Noise

The emission of photons in radioactive decay is a Poisson process. This implies that the measurements of the projections also include Poisson noise. Since the variance of Poisson noise is proportional to the mean activity, the acquisition of a high number of counts will increase the signal-to-noise ratio. However, for other reasons the number of counts is small. Decreasing the duration of the scan decreases costs, patient discomfort and the possibility of patient movement. Decreasing the radiation dose, likewise decreases costs and patient discomfort. This implies that for financial and health reasons, the quality of a SPECT image is minimized to the point were interpretation becomes questionable ('As Low As Reasonable Achievable'). Therefore, a low signal-to-noise ratio is inherent to a SPECT image and noise thus is major cause of image degradation.

Other image degrading effects

Other instrumentation-related processes influencing the quality of SPECT images are non-linearities and non-uniformities of the detector and inaccuracy of the center of rotation of the detector. Correction methods for these effects exist. Therefore, their influence is relatively small compared to effects of collimator blurring, attenuation, photon scattering and noise. Finally, image quality can be significantly affected by biological factors such as tracer kinetics and target specificity, and by patient and/or organ movement during image acquisition.

1.3 SPECT reconstruction

The purpose of tomographic reconstruction is to obtain cross-sections of an object from projections of that object. Two different approaches are commonly used for SPECT reconstruction. Until recently, *Filtered back-projection* (FBP) was the universal method because of its simplicity and speed. *Iterative reconstruction techniques* permit the modeling of all image degrading factors and are therefore more accurate, but require much longer computation time. The acceleration that has been accomplished for these techniques over the last decade, has brought them into the range of clinical application.

1.3.1 Iterative Reconstruction

In iterative algorithms, using an initial estimate of the activity distribution (image), estimated projection data are generated by means of a forward projector. These calculated projections are compared to the measured projections. On the basis of this comparison, one can obtain a better estimate of the image using an update step. This process of forward projection, comparison and updating can be iterated until an acceptable image is obtained. The model of forward projection is represented by the *transition matrix* which is used in the iterative algorithm. The more accurate this transition matrix is modeled, the better the agreement will be between the estimated images and the real activity distribution.

SPECT projection data are severely affected by Poisson noise, which implicates that low pixel count values give a less accurate prediction of the time-average photon flux received in the pixel. A possible way to model the Poisson nature of the measurements is to treat the data as stochastic variables and not as exact measurements; noise-free projections are taken as the mean of the Poisson distributions. Calculating the *maximum likelihood* estimate of the emission distribution that generated the measured projections takes into account the Poisson nature of the projections. Without making any a priori assumptions about about the activity distribution, the statistically most likely emission distribution can be calculated using the Maximum Likelihood Expectation Maximization (ML-EM) algorithm [39, 107, 80]. The ML-EM algorithm updates all image elements i of the estimated image at iteration $k+1$ according to

$$\tilde{\lambda}_i^{k+1} = \frac{\tilde{\lambda}_i^k}{\sum_j c_{ij}} \sum_j \frac{c_{ij} p_j}{\sum_i c_{ij} \tilde{\lambda}_i^k} \tag{1.3}$$

where $\tilde{\lambda}_i^k$ represents the k-th image estimate, $C = \{c_{ij}\}$ represents the transition matrix, $P = \{p_j\}$ represents the measured data, and $\sum_i c_{ij} \tilde{\lambda}_i^k$ is the projection bin j after forward projection of the k-th image estimate.

This algorithm has the following important properties: (i) In every iteration, the algorithm increases the likelihood that the image estimate will generate the measured data (according to the transition matrix used!); (ii) Image elements in each iteration are constrained to remain positive; (iii) The algorithm takes into account the Poisson nature of the noise in the projection data. These features of the ML-EM algorithm lead to images which are less noisy than, for example, images reconstructed using FBP.

A drawback of ML-EM is that reconstruction is extremely slow, especially when accurate transition matrices are used. In order to render ML-EM fast enough to be used in a clinical setting, the scheme is often accelerated, for example using block iterative methods like the Ordered Subsets Expectation Maximization (OS-EM) algorithm of Hudson and Larkin [59]. OS-EM involves grouping projection data into an ordered sequence of subsets. The EM algorithm is then applied to each subset, and the result is used as the starting estimate for processing the next estimate. It has been shown that OS-EM can reach acceleration factors that are close to the number of subsets used [59, 70], while achieving image quality that is similar to standard ML-EM. An additional decrease of the reconstruction time can be achieved using a less complex transition matrix for the update step than for the forward projection step [71]. This approach is also known as the dual-matrix method. An overview of accelerated EM algorithms are given in [61] and [81].

1.3.2 Calculation of the transition matrix

The transition matrix describes the forward projection and re-projection used in iterative SPECT reconstruction. In order to generate an accurate transition matrix one requires an accurate method for calculating photon transport in SPECT and an estimate of the density distribution of the patient, which can be represented by a transmission CT map. Acquisition of a transmission CT image has become a common part of the total SPECT acquisition protocol, especially in cardiac SPECT. Other arguments for acquisition of a transmission CT image are improved anatomical localization of activity (e.g. in tumors and infectious foci), registration with other imaging modalities and dose calculations.

Transmission CT in nuclear medicine

A straightforward way of acquiring a transmission CT (TCT) image would be to make a separate scan of the patient on an X-ray CT scanner. However, this is an expensive option and it requires accurate registration of the CT and SPECT images, which is non-trivial in many cases. Much effort has been spent on developing ECT systems that acquire transmission CT data simultaneously with the emission data (ECT-TCT scanning). The simultaneous acquisition of these scans immediately solves the registration problem, and which renders the accurate attenuation correction possible. It has been shown for example that the use of such ECT-TCT systems can significantly improve the diagnostic accuracy of cardiac SPECT for the detection and localization of coronary heart disease [44].

Although there have been some advances in the development of combined ECT-TCT scanners that use X-ray tubes, most commercial ECT-TCT systems use radio-active sources to generate the TCT data, and a large variety of source materials (e.g. Gadolinium [113], Technetium [50], Tellurium [122], etc.), source shapes (sheet sources, line sources and one or more point sources) and collimator geometries (parallel hole, fan-beam, asymmetric fan-beam) are currently available. An example of such a system is shown in Fig. 1.3.

Figure 1.3: Example of an ECT-TCT system. This system uses two scanning line sources containing Gadolinium to acquire the transmission data.

Photon transport modeling

Modeling photon transport in SPECT (i.e. scatter, attenuation and collimator blurring) for use in iterative reconstruction is often considered to be challenging, since the calculation method must be accurate for acceptable quality of the image reconstruction and at the same time efficient if it is to be used in clinical practice.

One class of methods, which includes anatomy-dependent scatter in the reconstruction, first calculates and stores in tables the scatter responses of point sources behind slabs for a range of thicknesses, and then tunes these responses to various object shapes with uniform density [8, 47, 15]. A disadvantage of this method is that it cannot accurately include the effects of non-uniform densities, such as found in the thorax, on wide angle scatters (chapter 2).

A second class of methods, which can readily handle media of non-uniform density and large angle scatters, is based on Monte Carlo (MC) simulation [46]. A drawback of MC simulation is that it can take several days to calculate accurate, almost noise-free data. This was the motivation to focus the research described in this thesis on the development of acceleration methods for MC simulation of SPECT. These accelerated methods were implemented in the Utrecht Monte Carlo System, a general MC simulation framework developed in our group. Together with the powerful PCs that are available nowadays, MC simulation thus becomes feasible for use in clinical image reconstruction.

Monte Carlo Simulation

Monte Carlo (MC) simulation can be described as a statistical simulation method based on random sampling of probability density functions (PDF). Such a $PDF(x)$ can, for example, describe the photon path length x up to the next interaction with matter. MC

simulation was first used during the World War II Manhattan project. Von Neumann named it Monte Carlo simulation because of the similarity between statistical simulation and games of chance, and because the city in the principality of Monaco was a center for gambling [126].

Sampling a $PDF(x)$, normalized by integration over its definition range $[a, b]$, can be performed by constructing a cumulated probability density function ($CPDF(x)$):

$$CPDF(x) = \int_a^x PDF(x')dx' \tag{1.4}$$

A random variable x can be sampled by substituting a random number in the range of [0,1) for $CPDF(x)$ and solve the equation for x. If $PDF(x)$ is analytically integrable, x can be sampled in a straightforward manner. Often the $PDF(x)$ is too complex to allow analytic integration, as in the case of the Klein-Nishina formula which describes the probability of Compton scattering over angle θ. In such cases the $CPDF(x)$ can be described numerically. A number of papers give an overview of the MC method and its application to SPECT scatter simulation [102, 2, 85, 126].

Acceleration of Monte Carlo Simulation To make the - notoriously slow - MC simulation feasible for scatter correction in SPECT, acceleration methods denoted by variance reduction techniques (VRTs) are often used [57]. A very popular VRT to increase photon yield on the detector is forced detection (FD) [4, 84]. In the present work several acceleration methods are developed; these have been designed particularly for fast scatter calculation of extended distributions in SPECT.

Utrecht Monte Carlo System Many MC programmes are in use in the field of nuclear imaging. These include EGS4 [96], MCNP [23], SIMSET [55] and SIMIND [82]. Some of them can simulate not only transport of photons in detail, but also electrons or neutrons. Since these programmes are often designed to permit the study of a large range of photon transport problems, they are often complex to use and computationally inefficient. This inefficiency is a direct cause of the generality of the programs. Furthermore, existing codes VRTs often don't allow to include other VRTs or acceleration methods designed for a specific SPECT imaging situation into existing codes.

The Utrecht Monte Carlo System (UMCS) [33] was designed to overcome these problems and to accelerate photon transport simulation in SPECT. The code is written in C++. The simulations of photon transport include effects of Compton scatter and photoelectrical absorption. As input for the calculations, UMCS requires a digital representation of the activity distribution (activity or source map) and mass density distribution (attenuation or TCT map) in the patient.

UMCS was validated using measurements of line-sources in uniform and non-uniform phantoms, and projections and energy spectra of extended source distribution were generated with the SIMIND MC code [83]. The results of these validations are reported in [32]. A comprehensive description of the various features and how they can be used is given in the UMCS manual [33].

1.4 Simultaneous Dual Isotope SPECT

In SPECT a radio-pharmaceutical is administered to the patient; it is then distributed through the body in a way determined by the properties of that radio-pharmaceutical and by the anatomy and physiology of the patient. Sometimes, it is important to monitor two different physiological functions or one function under different physical or medical conditions. This can achieved by acquiring two SPECT studies using the same radio-isotope in both studies or using two different radio-isotopes; the latter is called Dual-Isotope SPECT. When two different radio-pharmaceuticals are used with distinguishable emission energies, both SPECT studies can also be acquired simultaneously using different energy windows. This is called simultaneous Dual-Isotope SPECT. A significant advantage of having only one SPECT acquisition is the shorter time needed for the study. This doubles the throughput of the hardware and reduces patient discomfort, which in turn reduces the likelihood of artifacts due to patient movement. Furthermore, simultaneous acquisition ensures perfect co-registration between the images for each isotope.

Dual-Isotope SPECT studies have a wide range of uses; these include the evaluation of myocardial viability and perfusion (e.g. [76, 3, 19, 94, 52] and brain function [100, 43]. The radio-pharmaceuticals used for these studies include a number of combinations, e.g. Tc-99m/Tl-201, Tc-99m/In-111, Tl-201/In-111, Tc-99m/I-123, Tc-99m/Kr-81m, F-18/Tc-99m. This thesis focuses on down-scatter correction in simultaneous Tc-99m/Tl-201 stress/rest myocardial perfusion imaging. The proposed methods, however, are fairly generic, and therefore can be adapted easily for use with other isotope combinations and imaging applications.

1.4.1 Simultaneous Tc-99m/Tl-201 myocardial SPECT imaging

Myocardial SPECT imaging is employed to evaluate patients with known or suspected coronary artery disease. In most protocols, Tl-201 or a radio-pharmaceutical based on Tc-99m (e.g. Tc-99m sestamibi) is used. Tc-99m has a photon emission energy of 140 keV while Tl-201 emits most photons in the energy range of 70-80 keV and has some abundancies at 135 keV and 167 keV. Ideally, the uptake of the radio-pharmaceutical in the myocardium (left ventricular wall) is proportional to the perfusion of the tissue. In order to assess the condition of the myocardial tissue, perfusion is often measured at rest and under stress. In a typical rest Tl-201/stress Tc-99m Dual-Isotope SPECT study 3 - 4 mCi (112 - 148 MBq) of Tl-201 is injected intravenously with the patient at rest. Next, the patient is prepared for stress, for example by exercise on a home-trainer. A 25 mCi (900 MBq) dose of Tc-99m is injected at the peak stress. It is assumed that the resting Tl-201 distribution remains unchanged during exercise. The Dual-Isotope SPECT study can be acquired shortly after the Tc-99m injection (Fig. 1.4). Comparison of the Tl-201 and Tc-99m distributions gives information about the viability of the myocardium.

More specifically, the uptake of Tl-201 in the cells depends on the integrity of the cell-membrane. Directly after injection ischemic tissue will show decreased Tl-201 uptake, which improves in time due to redistribution of the Tl-201 towards ischemic areas. A myocardial infarct will show no uptake or a very low uptake which is indistinguishable from the background.

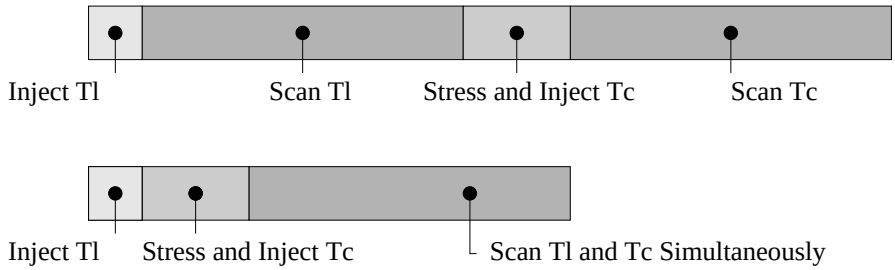

Figure 1.4: Time frame of a typical simultaneous Dual-Isotope SPECT protocol (Bottom). For comparison of the total time involved in the study, a time frame of a sequential Dual-Isotope SPECT protocol is also shown (Top). The white areas indicate time reserved for the necessary metabolus of the radio-labeled molecules.

Tc-99m sestamibi accumulates within the myocytes of the myocardial cells. The Tc-99m distribution differs from the Tl-201 distribution in that it hardly redistributes to ischemic regions. Because Tc-99m is injected during stress at high perfusion of the myocardium, there will be a large contrast in well perfused tissue and defects. Both viable and non-viable (infarct) defects will be visible in the stress Tc-99m images. A viable defect, however, will disappear in the Tl-201 image, and is therefore referred to as a reversible defect (Fig. 1.5).

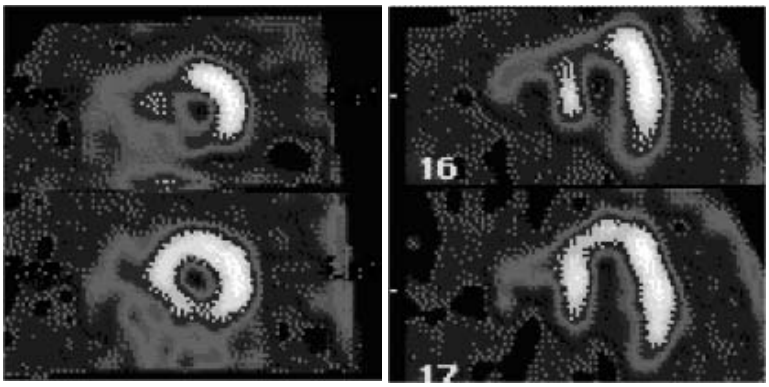

Figure 1.5: Example of a reversible perfusion defect in a cardiac SPECT study. Shown are tomographical cross-sections through the short (left) and long (right) myocardial axes. Stress images (Top) show a defect, while the rest images (Bottom) show normal perfusion.

The different re-distribution features of Tc-99m and Tl-201 are used in dual-isotope SPECT, to distinguish between viable and non-viable defects. The two isotopes differ also with respect to their more general imaging characteristics. The fraction of Tc-99m sestamibi which is extracted from the blood into the myocardial cells is approximately

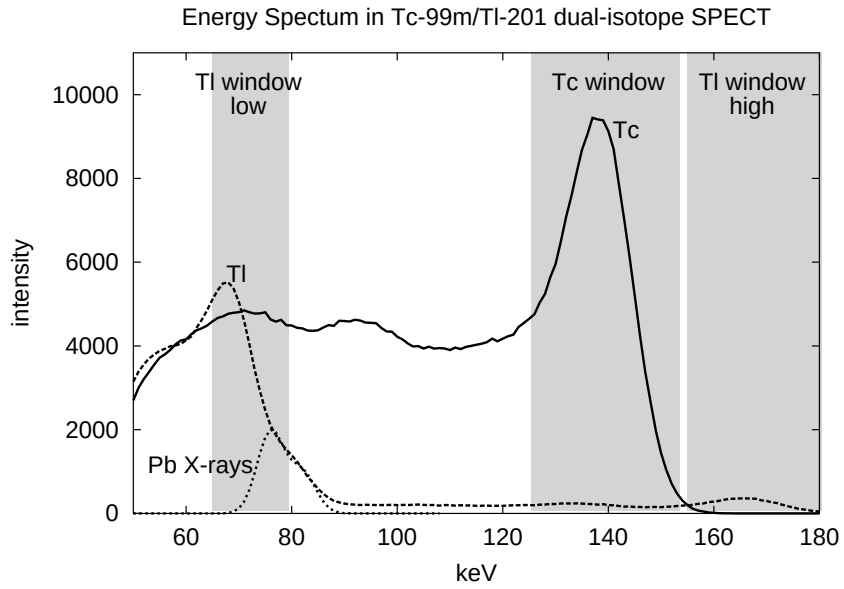

Figure 1.6: Sample energy spectrum indicating detected Tc-99m photons, Tl-201 photons and Pb x-rays. Photopeak energy windows for Tc-99m and Tl-201 (high and low) are indicated.

60%, which is lower that the 80% value seen for Tl-201. Generally about 1% of the injected Tc-99m dose accumulates in the myocardium, as compared to 3% for Tl-201. The major part of the injected dose accumulates in the rest of the body such as the liver, gall bladder and lungs, depending on the condition of the patient. A disadvantage of Tl-201 over Tc-99m is the lower photon emission energy, which increases the probability that photons will scatter in the patient and degrade the image. Furthermore, Tl-201 has a half-life of 72 hours, much longer than the 6 hour half-life of Tc-99m. Together with the fact that Tl-201 is more poisonous than Tc-99m, this means that much less Tl-201 activity can be used than Tc-99m.

1.4.2 Down-scatter

A major image degrading effect in Dual Isotope SPECT is the appearance of photons of one isotope in the energy window of the other isotope. In the case of simultaneous Tc-99m/Tl-201 imaging, there is substantial down-scatter from Tc-99m into the Tl-201 photopeak window in the region of 70-80 keV. This is demonstrated by the sample Tc-99m energy spectrum shown in Fig. 1.6.

This energy spectrum also shows the energy windows used in this thesis. Not shown in this figure is the slight contamination of the Tc-99m data caused by the presence of

the Tl-201 photons at 135 keV and 167 keV. However, due to the low abundance of these emissions and the often high ratio of the administered Tc-99m/Tl-201, the down-scatter of Tl-201 photons into the Tc-99m energy window is relatively insignificant.

The down-scatter of Tc-99m photons into the Tl-201 window is substantial. The largest component of this down-scatter is due to Tc-99m photons losing energy in Compton scatter events in the patient. A second significant source of down-scatter is the detection of fluorescence x-rays (Pb x-rays) produced by photons interacting with the collimator [92, 68].

Down-scatter in Tc-99m/Tl-201 myocardial SPECT imaging can lead to artifacts in the acquired SPECT images; these include grossly inaccurate quantitation of the Tl-201 image as well as reductions in defect size and in contrast [72, 26]. This may cause overestimation of the defect reversibility of the ischemic myocardial region. Therefore, simultaneous Tc-99m/Tl-201 myocardial SPECT imaging is often not recommended for clinical use, until adequate methods of correction for this down-scatter become available [72, 19].

1.4.3 Image reconstruction in Dual Isotope SPECT

In Tc-99m/Tl-201 simultaneous Dual-Isotope SPECT, the Tc-99m image is hardly affected by down-scatter. Therefore, the Tc-99m image can be reconstructed using the same approach as used in Single Isotope SPECT (eq. (1.3)). Next, the Tc-99m down-scatter in the Tl-201 energy window can be estimated by projecting the reconstructed Tc-99m image into the Tl-201 energy window, using a down-scatter model. The Tl-201 image is then corrected for down-scatter by incorporating this down-scatter during iterative reconstruction. The down-scatter term (DS) is added to the ML-EM algorithm as follows:

$$\tilde{\lambda}_i^{k+1} = \frac{\tilde{\lambda}_i^k}{\sum_j c_{ij}} \sum_j \frac{c_{ij} p_j}{\sum_i c_{ij} \tilde{\lambda}_i^k + DS} \tag{1.5}$$

Accurate reconstruction of the Tc-99m image is important because inaccuracies can propagate into the Tl-201 image via the down-scatter estimation. Kadrmas et al. proposed that the Tc-99m and Tl-201 images should be reconstructed simultaneously instead of sequentially as described above. The advantage of this is that both the down-scatter of Tc-99m in the Tl-201 energy window and down-scatter of Tl-201 in the Tc-99m window can be incorporated, although the latter source of down-scatter can be expected to be minor for most imaging situations. A crucial element of the reconstruction of Dual-Isotope SPECT study is the accuracy of the down-scatter model.

1.4.4 Down-scatter Calculation for simultaneous Dual Isotope SPECT

Just as with scatter correction in SPECT (section 1.3.2) the down-scatter estimate can be calculated when the Tc-99m distribution, a CT map and a down-scatter model are available. The ideal down-scatter model provides an accurate description of the down-scatter

process, but is time-efficient. Since large angle scatters and back-scatters play an important role in the down-scatter process, analytical scatter models are less suitable for calculating down-scatter (chapter 2). In this thesis, we suggest that Monte Carlo (MC) simulation should be used for this task. However, MC simulation of down-scatter is computationally even more demanding than MC simulation of scatter in the photo-peak window. This is mainly due to the fact that high order scatter events contribute significantly to down-scatter. In this thesis several acceleration methods for MC down-scatter calculation are proposed.

1.5 Contents of this thesis

In **chapter 2** the influence of backscatter material on Tc-99m and Tl-201 scatter projections is investigated. This investigation is important because in many analytical scatter models backscatter is not taken into account, while backscatter is a significant part of Tc-99m down-scatter in the Tl-201 window. Efficient scatter calculation in photo-peak windows, is possible when analytical models are combined with MC simulation. This is achieved for instance by a combination of correlated photon tracking and convolution-based forced detection, as described in **chapter 3**. Convolution-based forced detection as a stand-alone technique is validated in **chapter 4**.

Acceleration of MC simulation of down-scatter is achieved by Rotation-based Monte Carlo (RMC). RMC is based on the calculation of only a few projections of the total SPECT study using MC and then one takes a short-cut to estimate the other projections. RMC is described and validated in **chapter 5**.

In **chapter 6** a method is explained to incorporate Pb x-rays into the down-scatter calculation. Furthermore, the simulation of down-scatter is validated using experimentally measured data. Application of the model-based down-scatter correction for Tc-99m/Tl-201 Dual-Isotope SPECT is demonstrated in **chapter 7**. The thesis ends with a discussion of the proposed methods, a brief comparison of SPECT with other cardiac imaging modalities, and some concluding remarks (**chapter 8**).

Chapter 2

The influence of backscatter material on Tc-99m and Tl-201 line source responses

H.W.A.M. de Jong[1], F.J. Beekman[1], M. Ljungberg[2] and P.P. van Rijk[1]
[1]University Medical Center Utrecht
[2]Lund University and Helsingborg Hospital, Sweden
Physics in Medicine and Biology, Vol. 44, pp. 665-679, 1999

SPECT projections are contaminated by scatter, resulting in reduced image contrast and quantitative errors. When tissue is present behind the source, some of the detected photons backscatter via this tissue. Especially in Dual Isotope SPECT and in combined Emission-Transmission SPECT, backscatter constitutes a major part of the down-scatter contamination in lower energy windows.
In this paper, the effects of backscatter material were investigated. Planar images of Tc-99m and Tl-201 line sources between varying numbers of perspex slabs were analysed using the photopeak windows and various scatter windows.
In the Tc-99m photopeak window no significant change in total counts due to backscatter material was measured. In the Tl-201 photopeak window an increase of about 10% in total counts was observed. In the scatter windows an even more explicit influence of backscatter material was measured. For instance, at a forward depth of 10 cm, total counts of a Tc-99m source detected in the 72 keV window eventually doubled with increasing backscatter material, compared to the situation without backscatter material. The backscatter contribution plateaud when more than 5 - 10 cm of scatter material was placed behind the source.
In conclusion, backscatter should be taken into account, particularly in model-based down-scatter correction methods in Dual Isotope SPECT and combined Emission-Transmission SPECT.

2.1 Introduction

The gamma cameras commonly used in nuclear medicine have limited energy resolution. To detect sufficient photons, a broad photopeak window is used, which permits the detection of scattered photons. In several situations scatter can account for more than half of all the counts detected in the photopeak window [45], and thus causes degradation in image contrast and quantitative accuracy. For instance, in Tc-99m/Tl-201 Dual-Isotope SPECT, which is used to reduce scan times and allows for better registration between the Tl-201 and Tc-99m images, scatter of Tc-99m photons in the Tl-201 photopeak window causes an overestimation of the Tl-201 distribution (e.g. [72], [124], [53]). In Tc-99m/Gd-153 combined Emission-Transmission CT, which allows for accurate attenuation and scatter correction, down-scatter of Tc-99m photons hampers the reconstruction of the transmission map (e.g. [113], [58], [10]). For model-based down-scatter correction it is therefore mandatory to know the scatter response of Tc-99m (140 keV) in the Tl-201 (72 keV) and Gd-153 (100 keV) photopeak windows (e.g. [65], [12]).

One class of scatter correction methods incorporates the scatter models in iterative reconstruction. This gives a better contrast-to-noise ratio of small cold lesions than do subtraction-based methods [9]. In addition, knowledge of the scatter response can be used to simulate SPECT in a realistic way (e.g. [104], [17]).

The most general scatter correction methods proposed are based on Monte Carlo (MC) simulation [46], [82], or on analytical photon-transport equations including Klein-Nishina (K-N) equations (used by [104], [120], [27]). These methods can readily handle non-uniform attenuating media. However, generation of the transition matrix has to be repeated for every SPECT study and makes excessive demands on computer time and memory, especially when photon cross-talk between slices is being modelled (fully 3D reconstruction).

The response of a source in an arbitrary object can also be approximated from a series of responses of line sources measured behind slabs of various thicknesses (slab-derived scatter compensation as described in [8] and [47]). These models are known to give highly quantitative images when used in iterative scatter correction [13]. Slab-derived scatter models can be regarded as a practical alternative to the time-consuming, but more general MC or K-N-based methods, but such models do not incorporate the detection of photons scattering via material behind the source. To our knowledge no study on the influence of this large-angle scatter on both Tc-99m and Tl-201 responses has yet appeared in the literature. The purpose of this study was to investigate experimentally how scatter material behind the source affects the line source response in Tc-99m and Tl-201 photopeak and scatter windows. The results may be useful for improving future scatter models.

2.2 Theory

In this section a simple analytical description is given of photon transport through uniform media.

The majority of scatter events are detected photons which have undergone Compton interaction in tissue. In the case of Compton interaction, a scattered photon loses energy after collision with an electron. The relation between the initial energy E_0 and final energy E_f of a colliding photon is given by the Compton formula:

$$E_f = \frac{E_0}{[1 + (E_0/E_r)(1 - \cos\theta)]} \tag{2.1}$$

where θ is the angle between the initial and final direction of the photon and the electron rest energy E_r equals 511 keV.

The energy loss $E_0 - E_f$ increases with the scatter angle θ. If the energy range of photons scattered between 90° and 180° overlaps with the energy window of interest, the response in the window can be influenced by backscatter. Only single scatters events are considered here, however, photons detected in a down-scatter window have often scattered more than once. Hence, one should consider their final energy E_f after n times scatter [104]:

$$E_f^n = \frac{E_0}{[1 + (E_0/E_r)(n - \sum_{i=1}^{n} \cos\theta^i)]} \tag{2.2}$$

where θ^i's are the individual scatter angles.

Table 2.1: Energies of Tc-99m and Tl-201 photons after scattering. Final energy E_f depends on scatter order, scatter angles, and initial emission energy E_0.

scatter order	scatter angles	E_o=	140 keV	72 keV	80 keV	167 keV
1	90°		110 keV	63 keV	69 keV	126 keV
	180°		90 keV	56 keV	61 keV	101 keV
2	45°, 45°		120 keV	67 keV	73 keV	140 keV
	60°, 30°		119 keV	66 keV	73 keV	138 keV
	80°, 10°		114 keV	64 keV	71 keV	131 keV
	180°, 180°		67 keV	46 keV	49 keV	72 keV
3	30°, 30°, 30°		126 keV	68 keV	75 keV	148 keV
	5°, 5°, 80°		114 keV	64 keV	71 keV	131 keV
90	1° ($\times 90$)		139.5 keV			

This permits calculation of the minimum energy loss (or maximum E_f) of an n-th order scattered photon. A photon loses minimum energy when its scatter angles are equal

and as small as possible ($\theta_i = \frac{1}{n}\theta_{total}$) [1]. Table 1 shows the E_f of Tc-99m and Tl-201 photons for different scatter orders and total scatter angle θ_{total} of 90° (maximum E_f) and scatter angles of 180° (minimum E_f). In general, the higher the scatter order, the higher the maximum E_f and the lower the minimum E_f. This is illustrated in figure 2.1.

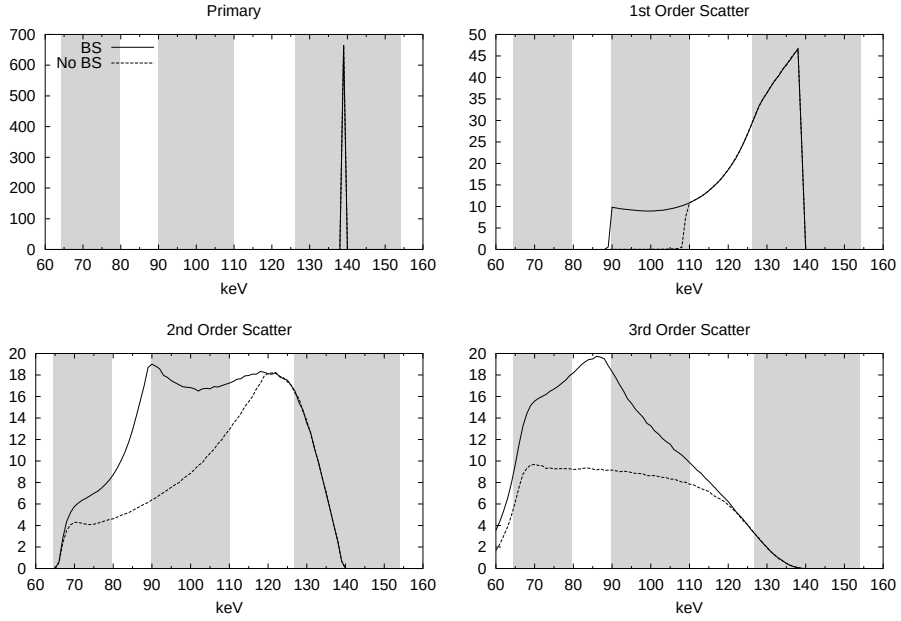

Figure 2.1: Monte Carlo-generated energy spectra of primary, first order, second order and third order scattered Tc-99m photons (E_0=140 keV) in a situation with backscatter material (BS) and without (No BS) using ideal detector resolution. Position of energy windows is illustrated by the shaded boxes. Left box: 72±10% keV, centre box: 100±10% keV, right box: 140±10% keV.

The figure shows energy spectra of a Tc-99m point source in a scattering medium with and without backscatter material, generated with the SIMIND Monte Carlo code [83]. SIMIND was validated by its author using scatter-to-primary ratios, scatter responses and energy spectra. At high energies the spectra in both scatter situations are identical. At energies below maximum E_f, backscattered photons increase the number of detected photons compared to the scatter situation without backscatter material. In reality this spectrum will always be blurred by typically 10%, but these simulations were done with perfect resolution in order to link the calculations to the spectra.

The possibility that a photon will backscatter with maximum ($\theta_i = 180^\circ$) or minimum energy loss ($\sum \theta_i = 90^\circ$) is small. For the latter case, all scatter angles must be

[1] The cosine function is convex on $[0, \frac{1}{2}\pi]$, e.g. increasing θ_1 and decreasing θ_2 by the same amount will decrease $\cos\theta_1 + \cos\theta_2$, and hence E_f will be smaller.

unidirectional[2], all must equal $\theta_i = \frac{1}{n}\theta_{total}$ and the scatter events must lie in one plane. The sum of scatter angles will most probably be in between the two extremes (figure 2.1).

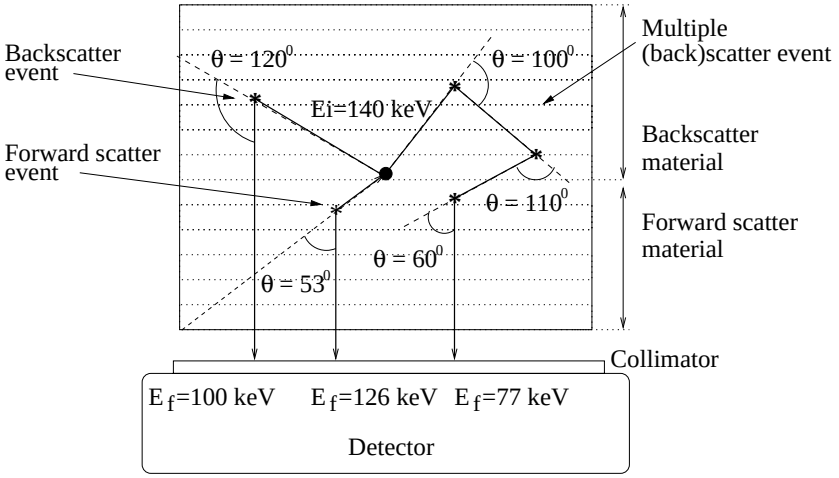

Figure 2.2: A forward single scatter event and a single backscatter event are shown, as are the final energies E_f of the photons. A multiple scatter event (3rd order) is also shown. The backscattered photons cannot be detected in the photopeak window (126 - 154 keV) because they have lost too much energy.

Using the simple analytical descriptions of photon transport, one can predict to a certain extent the influence that backscattered photons will have on responses. From table 1 and figure 2.1, it follows that backscattered Tc-99m photons cannot be detected in the photopeak window (126 - 154 keV), unless they have scattered at least three times. Even then, they are very unlikely to be detected in the photopeak window. This is because of the limited allowed scatter angles for detection (only few photons can backscatter with $\theta_{total} = 90°$, have equally distributed scatter angles, have all scatter events in one plane and satisfy the unidirectional demand). Increasing the scatter angles of these photons from $30°$ to $31°$ brings E_f down to 125 keV and makes their final energy fall outside the energy window[3].

The energies of the majority of backscattered photons correspond with the energy settings of the down-scatter windows; hence the responses in these windows are likely to be influenced by backscatter material. For down-scatter windows the maximum energy loss is important as well as the minimum energy loss of backscattered photons. For example, in the $72 \pm 10\%$ Tc-99m down-scatter window, no first order scatters will be detected. Responses in these windows will be dominated by multiple order scatters and thus will be broader than responses in the photopeak window.

[2]Scatter angles should be summed, taking into account the sign of the direction of the scatter angle, e.g. positive for counter-clockwise scatter.

[3]Limited energy resolution which broadens the energy spectrum is not taken into account, In these considerations.

Calculating the energy loss for backscattered Tl-201 photons is somewhat more involved. The energy spectrum of Tl-201 consists primarily of three abundant x-rays, i.e. 68.9 keV (25.51%), 70.8 keV (43.33%) and 80.1 keV (14.99%) and three gamma-rays of low abundance, i.e. 82.6 keV (4.15%), 135.3 keV (2.49 %) and 167.4 keV (9.53%) (taken from [110]). Table 1 includes three typical Tl-201 emission energies (72 keV, 80 keV and 167 keV). Of the 72 keV photons only a few multiple order scatters but no single scatters are to be expected in the photopeak window (64.8 - 79.2 keV). Especially backscattered 80 keV photons and some very large angle ($\theta_{total} > 180°$) scattered 167 keV photons will be detected in the Tl-201 photopeak window. Thus, the response in the Tl-201 photopeak window will contain backscattered photons.

The previous calculations predict that backscatter will influence responses in all energy windows used in this work, except for the Tc-99m photopeak window. More counts will be detected and the response will be broader due to the backscatter contamination, which consists largely of multiple scatters.

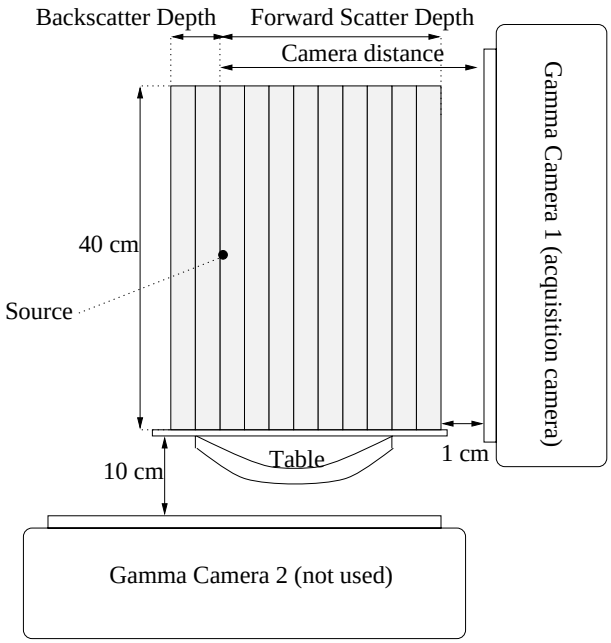

Figure 2.3: Experimental setup used to obtain the line source response at different thicknesses of backward and forward scattering material. Camera 2 is not used for the measurements.

2.3 Methods

In order to investigate the influence of backscatter material, measurements were performed using line sources placed between perspex slabs (Figure 2.3). The dimensions of the square perspex slabs were 40×40 cm and each slab had a thickness of 1.0 cm. The density of the perspex used was 1.19 g/cm^2. The source consisted of a small tube with an inner diameter of 2 mm and a length of 35 cm, containing Tc-99m (100 MBq) or Tl-201 (80 MBq). The tube was placed in a groove with a depth of 3 mm in the centre of a perspex plate. Line source responses were measured for combinations of 1, 4, 10 or 16 cm of perspex forward-scattering material and 0, 1, 2, 3, 5, 10 and 15 cm of perspex placed behind the source as backscatter material. Preliminary measurements showed that the patient table and the second detector had sometimes a marked effect on the scatter response when they were placed behind the source. In order to prevent backscatter from external objects as far as possible, the slabs were placed vertically on the table (Figure 2.3). No scatter objects were present within 4 m behind the source. The second detector, which was not used, was positioned 10 cm under the table, making an angle of 90 $^\circ$ with the used detector. For Tc-99m the following energy windows were used: 140 keV±10% (Tc-99m photopeak), 109 keV±15% (as used for Dual Window scatter correction by [64]), 100 keV±10% (Gd-153 transmission images) and 72 keV±10% (Tl-201 photopeak). The latter two windows are important for down-scatter correction in combined Tc-99m/Gd-153 Emission-Transmission SPECT (e.g. [10]) and Tc-99m/Tl-201 Dual-Isotope SPECT as used in [65]. The effects of Tl-201 backscatter were investigated using the photopeak window (72 keV±10%) and a scatter window (60 keV±7.5%). All data were acquired with an ADAC [4] dual-headed camera (Vertex^{TM}) equipped with high-resolution parallel-hole (VXHR) collimators.

The experiments were carried out with a matrix of 256×256 (pixel size 1.62 mm). After down-sampling by adding 4 pixels to calculate the counts in a 4 times larger pixel, profiles with a width of 18.1 cm were taken from the line source projection. In order to investigate the number of detected counts as a function of backscatter material, two regions were taken from the projections in which the counts were summed. The summed counts in the whole image (38×38 cm) are represented as region 1, whereas region 2 includes only the counts within a narrow region of 3.24×38 cm centered around the maximum. The detected counts in region 2 are not necessarily primary photons. Especially in the down-scatter windows region 2 includes only scattered photons. For example, primary Tc-99m photons will no longer be detected when the higher energy window threshold is lower than 126 keV if the energy resolution of the detector is 10%. [5]

Increases in total counts due to backscatter material are calculated as a percentage of the total counts in the situation where no backscatter material was present. Hence, no increase gives 0%, and 100% means that the total counts have doubled due to backscatter material. Furthermore, the Full Widths at Half Maximum and Full Widths at one Tenth Maximum (FWHM and FWTM) were calculated.

[4] ADAC Laboratories, Alder Drive 540, Milpitas CA, U.S.A.
[5] Collimator X-rays are not into account here.

2.4 Results

2.4.1 Technetium-99m

Figures 2.4 and 2.5 show Tc-99m line source response profiles in the various scatter situations in which the 72, 100, 109, and 140 keV energy windows were used. The forward depths of the source in these graphs were 4 cm and 16 cm. In the 140 keV photopeak window, no significant differences were observed between the line source responses in the various backscatter situations. The responses in the down-scatter windows rise with increasing backscatter material. The increase in counts in the Tc-99m line source projections is shown in the right-hand columns of table 2. In the lower energy windows, the presence of backscatter material clearly increases the number of photons detected. For example, the total counts in region 1 of the line source responses (Tc-99m, 72 keV window, forward depth 4 cm) increase by a factor of 2.68 and 2.13 in region 2 due to the backscatter material.

The increase in total counts in the Tc-99m line source projections as a function of backscatter thickness are shown in figure 2.6. The graphs on the left give the increase in counts in the total image (region 1); the graphs on the right include only the counts within a small region centered around the maximum (region 2). In all energy windows used a strong increase in total counts with increasing backscatter material is measured, except in the photopeak window. This is consistent with the theory which states that backscattered photons lose too much energy to be detected in the photopeak window. The increase in counts due to backscatter material is steep in the first few centimeters of backscatter material but plateaus eventually. The plateau is reached more rapidly in region 2 ($\sim$ 3-5 cm of backscatter material) than in region 1 ($\sim$ 5-10 cm of backscatter material).

Figure 2.7 shows the curves of the width of the responses as a function of backscatter material are shown. The response obtained at small forward depth and acquired in the 72 keV down-scatter window shows a particularly large increase in FWHM (66%) and in FWTM (40%). Responses measured in energy windows centered at higher energies and larger depths show less or no influence of backscatter. In general, 5 cm of backscatter material accounts for more than 90% of the backscatter effect.

2.4.2 Thallium-201

The line source responses of Tl-201 for different thicknesses of backscatter material are shown in figure 2.8 for forward depths of 4 and 16 cm. For this isotope too, the backscatter material has very little influence on the shape of the line source response in the photopeak window. Only on a log scale (curves on the right in figure 2.8), is a small increase in the tails noticeable. However, the total counts in the Tl-201 projections (figure 9) are affected by the amount of backscatter material. The maximum increase in counts in the photopeak window is about 10% for the total image (region 1), and 5.3% for the counts at the maximum of the line source response (region 2). In the scatter window centered at 60 keV and at a forward depth of 4 cm, there is a significant difference (over 95%) in the total counts for the situation without backscatter and the situation with 1 cm or more backscatter material. The width of the responses is significantly (up to 20%) affected by

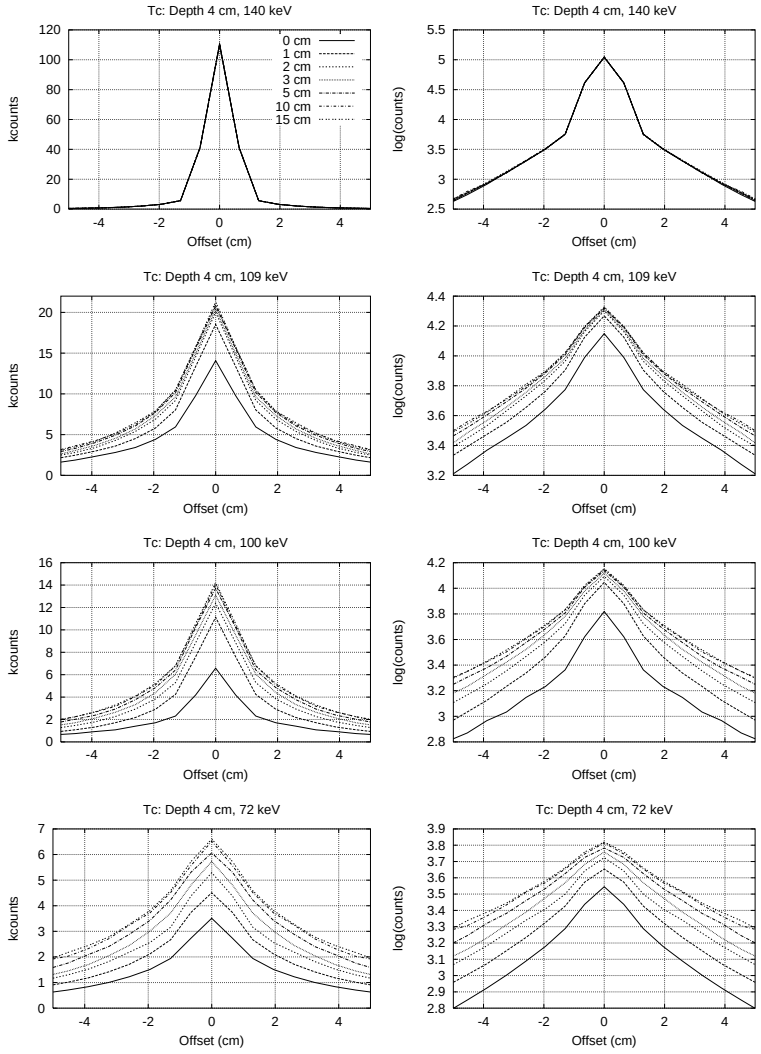

Figure 2.4: Comparison of Tc-99m line source responses at a forward depth of 4 cm for backscattering material thicknesses ranging from 0 to 15 cm and for different energy windows. The figures on the left are on a linear scale, the figures on the right are on a semi-logarithmic scale.

backscatter in the down-scatter window, but not in the photopeak window (figure 2.10).

As in the Tc-99m measurements, the steepest increase in counts is in the first few centimetres of backscatter material. Thereafter the number of counts quickly plateaus with increasing thickness. Table 3 shows the change in detected counts due to backscatter material.

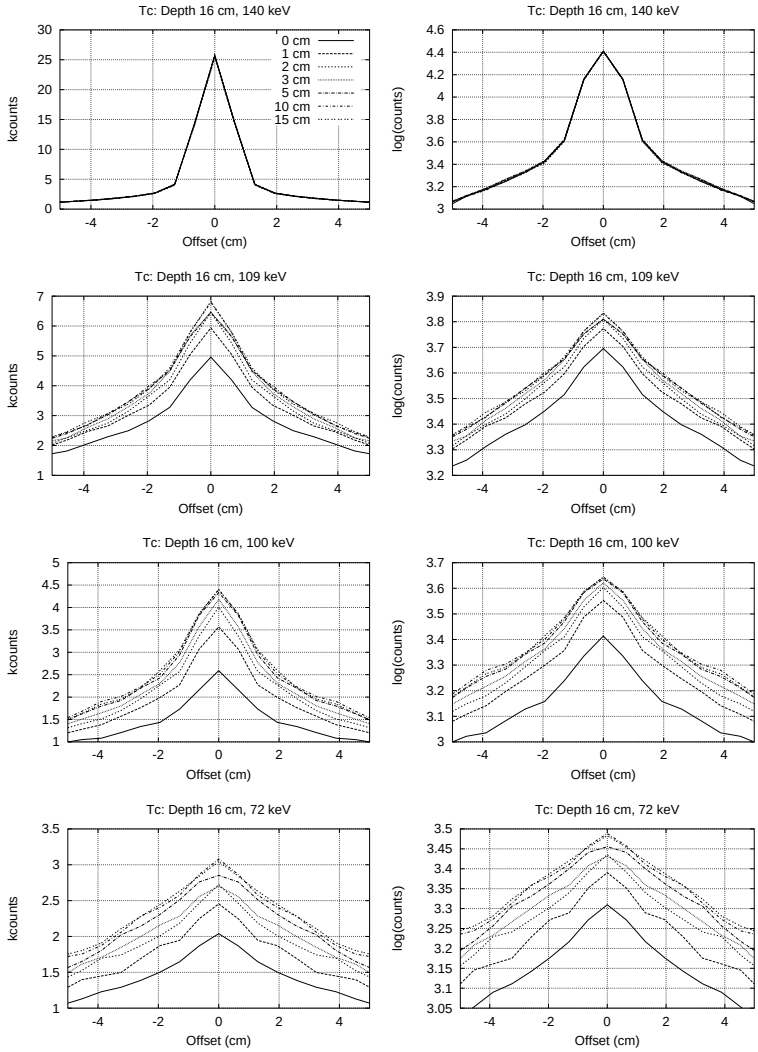

Figure 2.5: Comparison of Tc-99m line source responses at a forward depth of 16 cm for backscattering material thicknesses ranging from 0 to 15 cm and for different energy windows. The figures on the left are on a linear scale, the figures on the right are on a semi-logarithmic scale.

2.5 Discussion

The goal of this study was to investigate the influence of backscatter material on Tc-99m and Tl-201 line source responses in photopeak and down-scatter windows.

Down-scatter windows are important in Dual-Isotope SPECT and Emission-Transmission CT, because these are hampered by the spill-down of one radionuclide into a second ra-

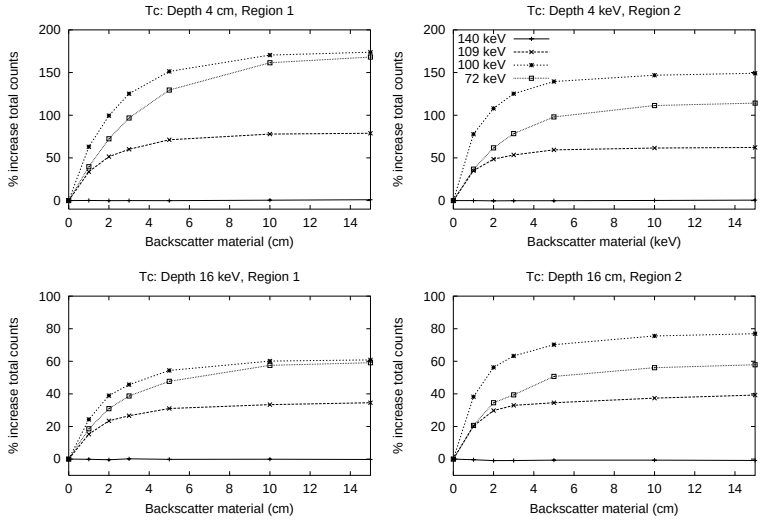

Figure 2.6: Increase in total counts in the Tc-99m line source projections at a forward depth of 4 cm (top frames) and 16 cm (bottom frames) as a function of backscattering material thicknesses, for the different energy windows. Left: counts in region 1. Right: counts in region 2

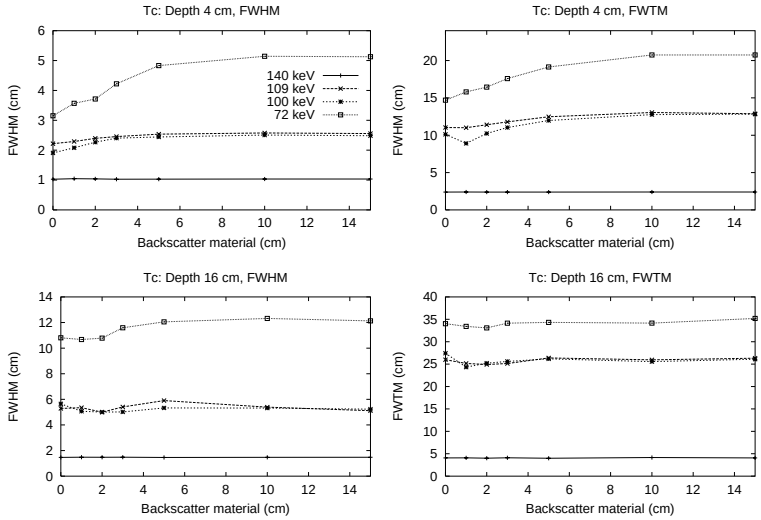

Figure 2.7: FWHM's (left) and FWTM's (right) of the Tc-99m line source projections at a forward depth of 4 cm (top frames) and 16 cm (bottom frames) as a function of backscatter material thicknesses, for the different energy windows.

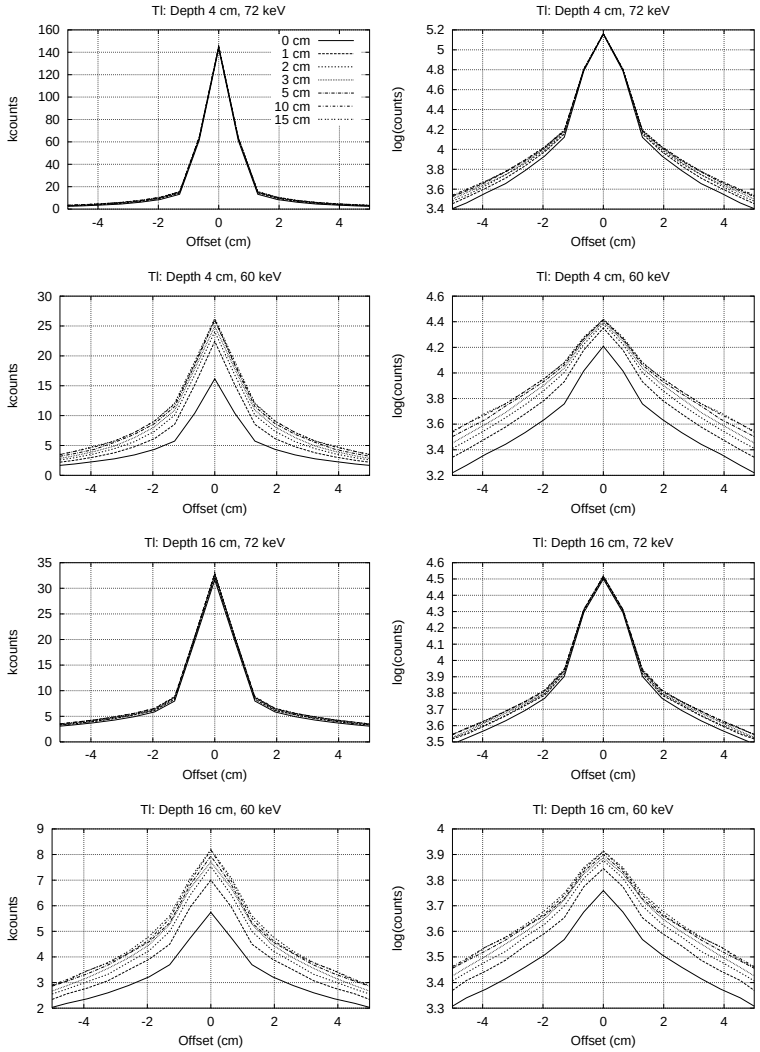

Figure 2.8: Comparison of Tl-201 line source responses at a forward depth of 4 cm (top) and 16 cm (bottom) for situations with backscattering material thicknesses ranging from 0 cm to 15 cm and energy windows centered around 72 keV and 60 keV. Left: linear scale. Right: semi-logarithmic scale.

dionuclide's photopeak energy window. Section 2 describes why the down-scatter windows are particularly affected by backscatter. In this section the simple representation of scatter using the Compton formula is appropriate since the underlying physics of photon transport through uniform media is well understood [42] and no new physical properties were sought. There are several parameters of SPECT acquisition which affect backscatter detection, such as energy resolution of the system, density of the interacting medium, and

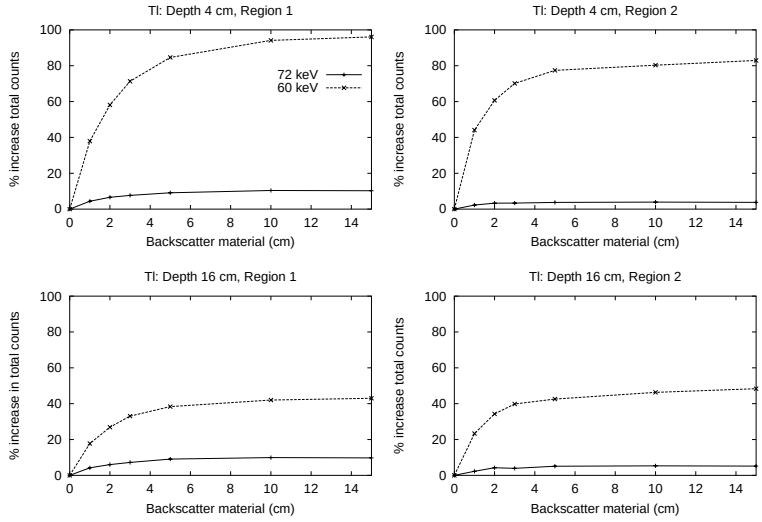

Figure 2.9: Increase in total counts in the Tl-201 line source projections at forward depths of 4 cm (top figures) and 16 cm (bottom figures) as a function of backscattering material thicknesses. Left: counts in region 1. Right: counts in region 2

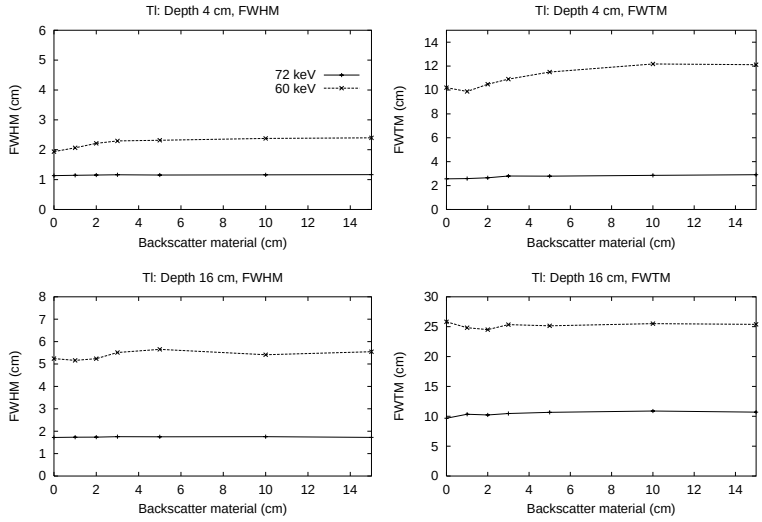

Figure 2.10: FWHM's (left) and FWTM's (right) of the Tl-201 line source projections at a forward depth of 4 cm (top frames) and 16 cm (bottom frames) as a function of backscatter material thicknesses.

Table 2.2: Tc-99m: Maximum increase in total counts due to 15 cm of backscatter material compared to no backscatter material for the two regions for different forward depths and energy windows. Region 1: total counts in projection, region 2: counts in maximum.

	Forward depth	Region 1	Region 2
140 keV	1 cm	0.0%	0.0%
	4 cm	0.1%	0.0%
	10 cm	1.4%	1.3%
	16 cm	0.0%	0.0%
109 keV	1 cm	143.8%	88.9%
	4 cm	78.6%	61.9%
	10 cm	46.7%	42.9%
	16 cm	34.3%	38.3%
100 keV	1 cm	344.7%	215.8%
	4 cm	174.5%	149.6%
	10 cm	88.7%	95.4%
	16 cm	60.6%	76.3%
72 keV	1 cm	300.6%	168.9%
	4 cm	167.6%	112.8%
	10 cm	87.8%	75.2%
	16 cm	57.5%	54.6%

width and location of the energy windows. Also, it is important to note that line sources and perspex slabs were used in this study, instead of point sources and water as scatter material.

Using the theory and considerations presented in section 2 one can explain the results obtained. These considerations may be useful for predicting trends in other experimental situations. One of the most important features of the results is the plateau effect. At small backscatter thicknesses the probability that a photon will backscatter is small because of the limited scatter angles. Increasing the backscatter thickness will allow more photons to backscatter. However photons scattered at large backscatter depths are less likely to be detected because they are more attenuated. At some point the addition of extra material, ceases to affect the yield anymore because the thick layer of backscatter material the photons have to pass, strongly attenuates the photon flux.

In all energy windows the increase in counts is largest in region 1. This means that the relative increase in counts due to the backscatter material is largest outside the maximum of the line source response. In region 2 the increase plateaus faster, at 3-5 cm of backscatter material. The total response (region 1) contains mainly multiple scattered photons and

Table 2.3: Tl-201: Increase in total counts for the two regions and for different forward depths. Region 1: total counts, region 2: counts in maximum.

	Forward depth	region 1	region 2
72 keV	1 cm	10.2%	4.0%
	4 cm	10.1%	3.7%
	10 cm	10.0%	4.0%
	16 cm	9.7%	5.3%
60 keV	1 cm	159.1%	113.0%
	4 cm	95.8%	81.9%
	10 cm	59.3%	59.7%
	16 cm	43.0%	47.9%

some first order scatter, as has been explained in section 2. Region 2 contains relatively more low order scatter, because these photons travel a shorter distance (mean path length between scatter events is approximately constant). The backscattered photons are typically higher order scattered photons, so region 1 will be influenced more by backscatter than region 2. Therefore the increase in counts in region 2 is smaller and it plateaus faster. The width of the response will also increase if relatively more counts are detected outside the centre of the response, as is shown in figures 2.7 and 2.10.

We have shown that 5 cm of backscatter material accounts for approximately 90% of the maximum extra counts. In larger objects like the thorax, the bulk of the detected photons originate from the part of the object where at least 5 cm of backscatter material is present; thus the projections will always have a backscatter contamination which is comparable ($\pm 10\%$) to that of the slabs. Therefore, a first order method for including backscatter in the slab-derived scatter model may be to add 5 cm of backscatter material to the slab measurements.

2.6 Conclusions

The influence of backscatter material on Tc-99m and Tl-201 line source responses was investigated for various energy window settings. The following conclusions are drawn from the measurements.

1. Backscatter material has no significant influence on the line source responses in the Tc-99m photopeak window. In the case of the Tl-201 photopeak, the number of total counts in the line source projections increase by up to 10% with increasing backscatter thickness.

2. Backscatter material has a strong effect on the line source response in scatter windows. In these windows total counts and width of the line source response increase strongly due to backscatter material.

3. More than 10 cm of scatter material behind the source has no important additional effect on the amount of scatter detected in all energy windows and forward depths considered. In most cases 1 cm and 5 cm of backscatter material account for approximately 30% and 90% of the total effect, respectively. When using slab-derived scatter correction the addition of 5 cm of backscatter material to the slabs can correct for the major backscatter effect in larger objects like the thorax, in which most photons originate from that part of the object where at least 5 cm of backscatter material is present.

On the basis of the results reported in this paper we conclude that backscatter has a strong influence on the Tc-99m and Tl-201 down-scatter responses, and can lead to a small increase in detected Tl-201 photons in the TL-201 photopeak window. This indicates that model-based down-scatter correction methods in Dual Isotope SPECT and combined Emission-Transmission SPECT should take backscatter into account.

Acknowledgements

We are grateful to ADAC Laboratories (Milpitas, CA) for financial support and to Chris Kamphuis and Eddy Slijpen (Image Sciences Institute, Utrecht University Hospital) for useful discussion, comments and technical support.

Chapter 3

Efficient SPECT Scatter Calculation in Non-Uniform Media using Correlated Monte Carlo Simulation

F.J. Beekman, H.W.A.M. de Jong and E.T.P. Slijpen
University Medical Center Utrecht
Physics in Medicine and Biology, Vol. 44, pp. N183-N192, 1999

Accurate simulation of scatter in projection data of Single Photon Emission Computed Tomography (SPECT) is computationally extremely demanding for activity distribution in non-uniform dense media. This paper suggests how the computation time and memory requirements can be significantly reduced. First the scatter projection of a uniform dense object (P^{sdse}) is calculated using a previously developed accurate and fast method which includes all orders of scatter (slab-derived scatter estimation), and then P^{sdse} is transformed towards the desired projection P which is based on the non-uniform object. The transform of P^{sdse} is based on two first-order Compton scatter Monte Carlo (MC) simulated projections. One is based on the uniform object (P^u) and the other on the object with non-uniformities (P^{nu}). P is estimated by $\tilde{P} = P^{sdse} \cdot P^{nu} / P^u$. A tremendous decrease in noise in $\tilde{P}$ is achieved by tracking photon paths for P^{nu} identical to those which were tracked for the calculation of P^u and by using analytical rather than stochastic modeling of the collimator. The method was validated by comparing the results with standard MC-simulated scatter projections (P) of Tc-99m and Tl-201 point sources in a digital thorax phantom. After correction, excellent agreement was obtained between $\tilde{P}$ and P. The total computation time required to calculate on a PC an accurate scatter projection of an extended distribution in a thorax phantom is a only few tens of seconds per projection, which makes the method attractive for application in accurate scatter correction in clinical SPECT. Furthermore, the method removes the need of excessive computer memory involved with previously proposed 3D model-based scatter correction methods.

3.1 Introduction

Detection of photons which have undergone scatter events is one of the main causes of image distortion in Single Photon Emission Computed Tomography (SPECT) and Positron Emission Tomography (PET). Over the last two decades, many methods have been developed for the purpose of reducing the resultant degradation of image contrast and loss of quantitative accuracy [24]. Some scatter compensation methods incorporate scatter in the transition matrix or point spread function (PSF) during iterative reconstruction. It has been shown that this can lead to highly quantitative accuracy (e.g. [46, 47, 120, 13, 99, 71]) and improved signal-to-noise ratios in the reconstructed images [13, 9, 67]. In addition, knowledge of the scatter response is valuable for fast simulation of tomographic data acquisition.

A complicating factor is that the scatter response is different for every point in the object to be imaged. Various methods for tackling this problem have been proposed for SPECT. These methods require information about the density distribution of the patient and can be divided roughly into two classes:

- One class of methods uses Monte Carlo (MC) simulations [46] to compute the entire transition matrix. The transmission matrix represents the mapping from the activity distribution onto the projections. MC simulation can readily handle media of non-uniform density. Due to photon cross-talk between slices, caused by collimator blurring and scattering, fully 3D SPECT reconstruction (instead of slice-by-slice (2D) reconstruction) is required for optimal image quality [13]. Unfortunately, hundreds of Giga-bytes up to several Terra-bytes of memory are required to store the complete non-sparse transition matrix when the fully 3D MC matrix approach is used, and it can take several months to generate the full matrix on a state-of-the-art workstation. In addition, the procedure has to be repeated for each patient. Analytical scatter models, based on integration of the Klein-Nishina (K-N) equation [105, 125], have practical disadvantages which are similar to those of MC based methods.

- A second class of methods, which includes anatomy-dependent scatter in the reconstruction, first calculates and stores in tables the scatter responses of point sources behind slabs for a range of thicknesses, and then tunes these responses to various object shapes with uniform density [8, 47]. This method is referred to as slab-derived scatter estimation (SDSE). A table occupying only a few megabytes of memory is sufficient to represent this scatter model for fully 3D reconstruction [13]. A fully 3D reconstruction of a Tc-99m cardiac study based on SDSE can be performed in only a few minutes on a state-of-the-art single processor workstation. A disadvantage of SDSE compared to matrices generated by MC simulation or K-N integration that it cannot accurately include the effects of the non-uniform mass density of the emitting object. So far only a few rough adaptations have been proposed to improve the accuracy of SDSE in non-uniform objects [49, 7].

The work reported here proposes an accurate and fast method for transforming the response of a distribution in a uniform object into the response of the same distribution in a

non-uniform object. This transformation is based on MC simulations that incorporate analytical instead of stochastic collimator blurring [31] and on a correlated photon tracking method. The theory of correlated Monte Carlo techniques for perturbation calculations is to be found in [111, 87, 106].

3.2 Methods

In this section, the SDSE method is first summarized briefly, since the method is used to calculate the scatter projection based on the object with uniform mass density, and includes all orders of scatter. In addition, the transformation of the SDSE-based projection into a projection based on a non-uniform object is discussed. Finally, the validation of the transformation method by means of MC-generated projection data of a digital thorax phantom is described.

3.2.1 Slab-derived scatter estimation (SDSE)

SDSE is based on the assumption that the scatter response of a point source in an arbitrary uniform dense object can be derived from a series of responses of point sources behind slabs of varying thicknesses. Consider an object containing a point source at position s_0 (Fig. 3.1). Because of the small acceptance angle of the collimator, photons detected at position j must have left the object near point P on the object surface. At point P, the point source has a "local depth" d_j. Therefore, the slab response at a slab thickness is chosen at d_j instead of d_{s_0} to evaluate the point source response at j. This method for accurately extending the scatter response model from slabs to arbitrary-shaped uniform objects has been evaluated extensively [8, 47, 17]. The SDSE method is very accurate for uniform objects, and includes all relevant orders and types of scatter in the model. The time to calculate a projection of an extended activity distribution using SDSE takes typically a few seconds on a PC.

3.2.2 Correction for non-uniformities

Two MC simulations are performed in order to correct SDSE-generated projections for effects arising from non-uniform mass-density. For computational efficiency, these simulations include only first-order Compton scatter. One simulation is based on a uniform object O^u with mass density equal to that of water, resulting in the projection P^u. The other simulation is based on a non-uniform mass-density distribution O^{nu} and generates the projection P^{nu}. Then a projection P^{sdse} based on SDSE and the uniform object O^u can be corrected for non-uniformities by multiplying each pixel j of P^{sdse} by a correction factor $C_j = P_j^{nu}/P_j^u$. C_j would converge to the exact correction factor if P^{nu} and P^u were exact; this is only possible if P^{nu} and P^u include all orders of scatter. However, in the results section it will be shown that modeling first-order scatter during the calculation of P^{nu} and P^u is sufficient to generate accurate correction factors. In the following subsection it will be explained how noise in C can be reduced if a correlated Monte Carlo

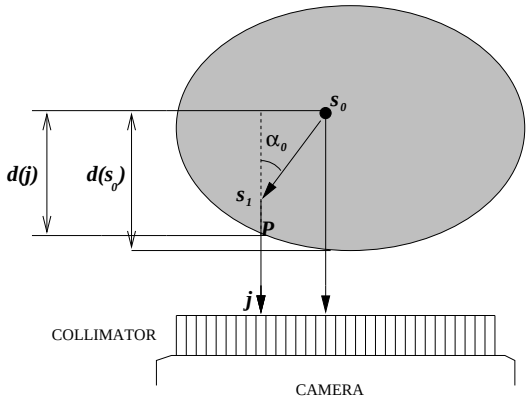

Figure 3.1: Cross-section of an object in front of a camera. A photon is emitted in voxel s_0, scattered at position s_1 and detected in pixel j.

technique is used to generate P^{nu} and P^{u}. Further noise reduction in P^{u} and P^{nu} is accomplished by analytical rather than stochastic modeling of the collimator. For this purpose, the weights of photons that scattered in voxel layers at different distances from the camera are stored in separate layers. These layers are then convoluted by a kernel representing the effects of intrinsic camera resolution and distance-dependent collimator response before they are added to P^{u} and P^{nu}. When analytical collimator modeling is used, standard MC simulation converges to noise free projections about 20 to 30 times faster than it does when stochastic collimator modeling is used [31].

Correlated Monte Carlo calculation

The Utrecht Monte Carlo System (UMCS, [109]), which is a dedicated MC simulator for fast calculation of SPECT projections of extended source distributions in non-uniform objects, was used to calculate P^{u} and P^{nu}. UMCS makes it possible to track identical photon paths in O^{u} and in O^{nu} by adapting the weights for differences in the density distribution in one of the simulations. This results in fast convergence of the correction map C, since noise correlations in corresponding pixels in P^{u} and P^{nu} are strongly increased. The tracking of equal particle paths [111, 87, 106] is a method that has been used successfully to accurately calculate perturbation in a wide range of situations; it is based on the idea that it is always possible to carry out a Monte Carlo calculation using probability distributions other than those which describe the physical stochastic scattering processes. However, the histories must be weighted by a cumulative product of the ratios between the different physical probability distributions.

In order to include one order of scatter in P^{u} and P^{nu}, photon histories and weights are calculated as follows: First, a photon path is selected in the uniform object O^{u} by (i) uniform random selection of an emission angle and (ii) selection of the amount of material the photon will pass through. This is done by sampling the probability distribution of the water-equivalent distance to collision. The scatter point s_1 (Fig. 3.1) is determined from

(i) and (ii). Then the photon is forced to be detected by directing it through a collimator hole. The initial weight w^u is multiplied by the probability of scattering under this angle α_1 (obtained from the K-N equations), and by the uniform attenuation that occurs over the trajectory from the scatter event to the detector. Generally, the weight w^{nu} of the photon that follows the same trajectory in O^{nu} is calculated by correcting for the ratios in attenuation due to non-uniformities and the ratios in density at scatter positions s_n:

$$w^{nu} = w^u \prod_{n=1}^{N} \left[\exp\left(\int_{s_{n-1}}^{s_n} \mu_{H_2O}^{n-1} - \mu^{n-1}(l)dl \right) \frac{\mu^{n-1}(s_n)}{\mu_{H_2O}^{n-1}} \right] \exp\left(\int_{s_N}^{j} \mu_{H_2O}^{N} - \mu^{N}(l)dl \right) \tag{3.1}$$

where $\mu^n(l)$ is the linear attenuation coefficient at position l in O^{nu} after photons have been scattered over angles $\alpha_1, ..., \alpha_n$, and where N is the scatter order. For first order scatter events, this equation takes the form:

$$w^{nu} = w^u . \exp\left(\int_{s_0}^{s_1} \mu_{H_2O}^{0} - \mu^0(l)dl \right) \frac{\mu_{(s_1)}^0}{\mu_{H_2O}^0} \exp\left(\int_{s_1}^{j} \mu_{H_2O}^{1} - \mu^1(l)dl \right) \tag{3.2}$$

where μ^1 is the linear attenuation coefficient after photons have been scattered over α_1, and μ^0 is the linear attenuation coefficient before any scattering has taken place.

3.2.3 Validation of the correction

In order to validate the method, we performed MC simulations of Tc-99m and Tl-201 point sources in the Mathematical Cardiac Torso (MCAT) phantom [117] (Fig. 3.2). These

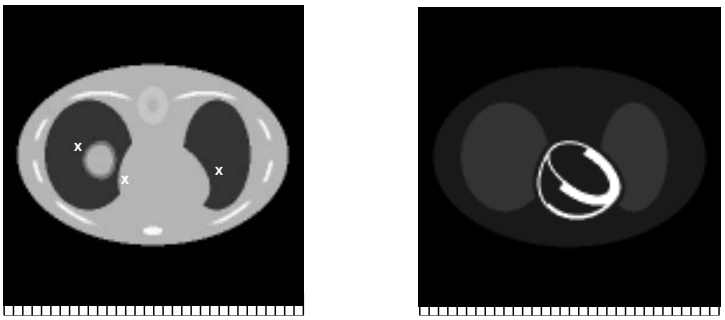

Figure 3.2: Cross-section of the MCAT phantom at mid-ventricular level and the collimator. Left: Mass density with position of point sources represented by crosses. Right: Extended activity distribution as used for generating the correction maps of Fig. 3.3.

simulations included no primary events, six orders of scatter, and were calculated using the SIMIND MC code [83]. The parameters used were typical for an ADAC Vertex Camera System equipped with VXHR collimators (hole length 54 mm and hexagonal hole diameter 2.03 mm, septum thickness 0.152 mm, collimator resolution $\approx$ 6.3 mm at 100 mm source distance). The energy resolution was 10%, the energy windows were 140

keV (20%) for Tc-99m and 72 keV (20%) plus 167 keV (15%) for Tl-201. The voxel size was 6mm x 6mm x 6mm and the grid size was 64 x 64 x 64. To illustrate what effect correlating the photon tracks during the MC simulation has on the convergence of C, anterior correction maps were calculated from the extended distribution shown in the right frame of Fig. 3.2. So that the extended distribution was representative for a cardiac study, we choose the relative activity concentrations of the background, the lungs and the myocardium in the ration 1:2:10.

Generation of slab-responses for SDSE

Slab-PSFs for SDSE were generated using SIMIND for depths ranging from 0.0 cm to 50 cm, and included scatter events up to the sixth order. The densities of the slabs and the uniform object O^u were chosen equal to the density of water. The effects of collimator blurring were not included in the slab-response generation but were later accounted for during SDSE simulation by convoluting with the distance-dependent detector response.

3.2.4 Assessment of convergence rate

In order to compare the convergence rates during calculation of the correction maps, we performed independent MC simulations and MC simulation based on correlated photon tracking with and without analytical modeling. The number of photon histories ranged from 6.10^6 to 2.10^9.

Almost noise-free Tl-201 correction maps of the extended distribution were calculated as a gold standard by generating 30.10^9 photon histories for P^{nu} and P^u. The Normalized Mean Square Error (NMSE) between the gold standard and the noisy correction maps in a region of interest (ROI) of 60x60 pixels in the center of the correction maps (64x64 pixels) was calculated as a function of the number of photon histories in P^u and P^{nu}.

3.3 Results

Tracking of identical photon paths clearly results in lower noise in the correction maps (Fig. 3.3, Right, Bottom) than when independent MC simulations are performed (Fig. 3.3, Left, Bottom).

The correction maps shown in Fig. 3.3 were based on a simulation time of 29.6 seconds per projection on a dual Pentium II 450 MHz. In this time 6 million photon histories were generated. The graph in Fig. 3.4 shows that independent MC simulations with stochastic collimator modeling take about 180 times longer per projection pair to make C converge than when C is based on correlated MC simulation with analytical collimator modeling. The graph shows that a speed-up factor of about six can be attributed to the fact that the spatial camera resolution was calculated analytically rather then stochastically, and a factor of about thirty can be attributed to correlated tracking. The sixfold speed-up due to analytical instead of stochastic modeling of the camera resolution effects

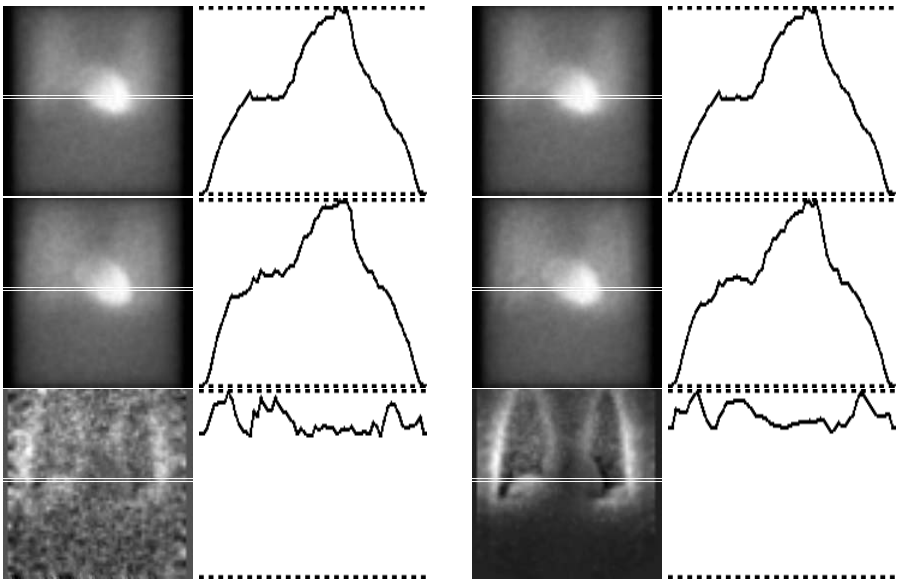

Figure 3.3: Anterior projections P^u (top row), P^{nu} (center row), and correction maps C (bottom row) with associated image profiles. Left) based on independent MC simulations. Right) based on MC simulations with correlated photon tracking. The projections and correction maps are based on equal calculation times per projection.

is lower than the factor of 20-30 found for uncorrelated MC in [31]. This could be caused by the fact that in the present work (i) a 64^3 image was used instead of a 128^3 grid and a high resolution collimator was used instead of a general purpose collimator, and (ii) the speed-up factor of the correlation map was evaluated instead of a projection generated by a more standard MC procedure.

The uncorrected point-source responses (P^{sdse}) and corrected point source responses $C.P^{sdse}$ are compared with Monte Carlo (SIMIND) generated projections in Figs. 3.5 and 3.6 where C is based on correlated photon tracking and analytical collimator blurring. The left frames depict the Tc-99m responses and right frames depict the Tl-201 responses. The image profiles show that the corrected SDSE are almost equal to the desired SIMIND MC responses. Only small discrepancies remain but are slightly more severe in the case of Tl-201. This may be caused by the fact that the Tl-201 responses contain relatively more multiple-order scatter events than do the Tc-99m responses.

3.4 Conclusions and Discussion

An efficient and accurate method has been presented for estimating photon scatter in projections from objects with non-uniform mass density. It has been shown that the scatter response of a uniform object can be transformed into the scatter response of a non-uniform

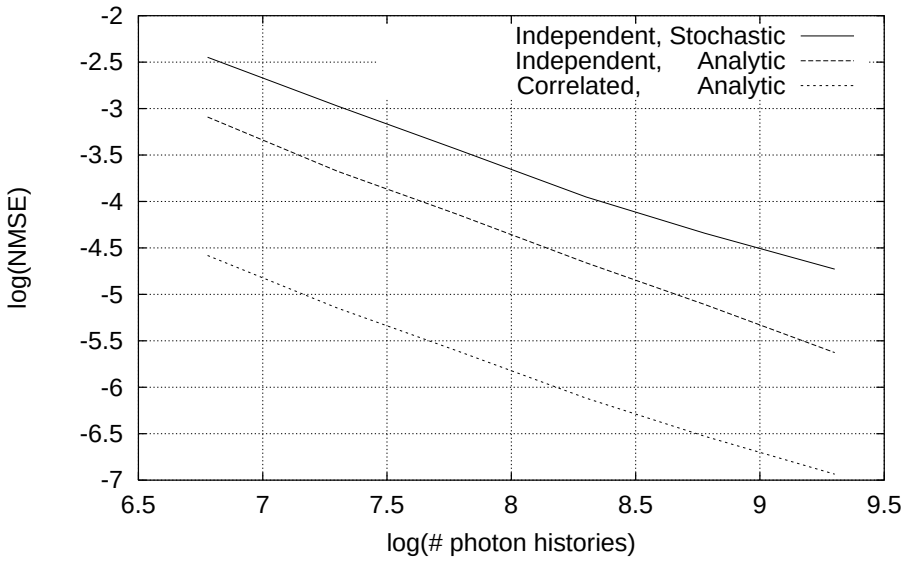

Figure 3.4: Normalized Mean Squared Error (NMSE) in the image profiles through the correction maps C (Fig. 3.3) as a function of the number of photon histories generated, for independent MC simulations with stochastic collimator blurring, for independent MC simulations with analytical collimator blurring and for correlated MC simulations with analytical collimator blurring.

object using two simulated projections which include only first-order scatter. These two MC simulated projections are generated in such a way that the noise level is low because the collimator is modeled analytically after probabilistic photon scatter modeling has been performed. Furthermore, the noise level of correction factors based on these simulations is decreased by using correlated photon tracks in the two MC simulated projections. The method is more than two orders of magnitude faster than a method that uses separate MC simulations and stochastic collimator blurring. Furthermore, no extra additional memory is required over the few tens of Mb required for SDSE reconstruction or simulation. For these reasons, the method has tremendous advantages over methods based on MC generation of complete matrices, especially when applied in fully 3D reconstruction.

Currently, the time needed to calculate correction maps for transforming a response from uniform to non-uniform objects may be somewhat too long for routine clinical implementation in iterative scatter correction, especially when the correction maps are calculated for all projection angles and each iteration anew. However, there are some simple ways in which the amount of computation time can be reduced. For example (i) it may be possible to calculate the correction maps in even less time, since the results of the calculation needed to select the scatter event positions and the attenuation over the trajec-

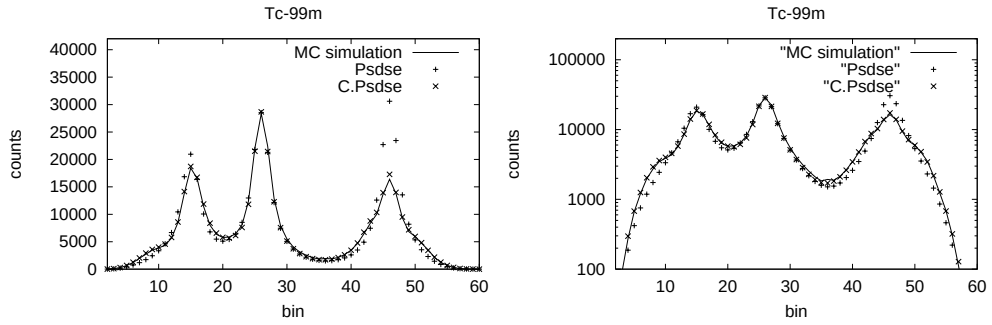

Figure 3.5: Scatter response of Tc-99m point sources. The solid line is the reference, the + signs represent the uncorrected SDSEs and the x signs represent the corrected SDSEs.

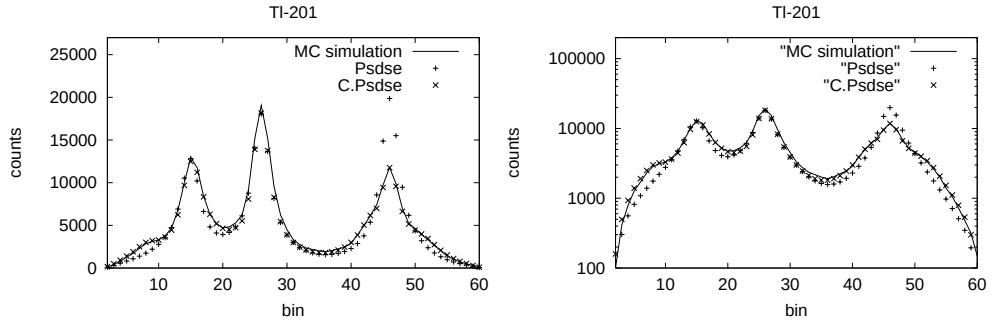

Figure 3.6: Like Fig. 3.5, but for Tl-201 point sources.

tory between emission and scattering can be re-used for more projection angles. (ii) the use of shorter MC simulation for the correction maps may be sufficient when combined with (edge-preserving) filtering of the correction maps (in the present method no filtering was performed), (iii) the correction factors may have to be calculated a few time only, since the calculated scatter estimate does not change much after only a few iterations of accelerated reconstruction algorithms like Ordered Subset Estimation Maximization (OS-EM [59]) or Dual Matrix OS-EM [71]. The scatter estimate can be kept as a constant term in later iterations instead of modifying the scatter estimate in each iteration [60, 66]. Alternatively, it may be worth investigating whether it is adequate to only approximate scatter modeling in the first couple of iterations, and calculate the correction factors only for latest iterations. (iv) Instead of completely recalculating the scatter estimates P^u and P^{nu} for each new iteration, only the differences in these estimates due to change in the iteration have to be calculated. This would involve the tracking of only a fraction of the photon histories required for a complete scatter estimates; finally (v) it might be possible to combine the currently used variance reduction with other variance reduction methods (see [56] for an overview of variance reduction techniques which have been applied to the

MC simulation of emission tomography). However, as processors become faster and the number of processors per computer increases, the method should soon become practical for routine scatter correction, even without adding any of these acceleration methods.

The use of only one order of scatter was sufficient for an accurate calculation of the correction factors needed to transform the scatter response based on a uniform medium to the scatter response of a non-uniform medium. One order of scatter sufficed, because the transformation conserves some intuitively desirable properties: (i) the scatter response is not changed by the transformation when the densities of the scatter objects (O^{u} and O^{nu}) are identical, (ii) the values in the scatter response approach zero for a source in an object with infinitely high density. (iii) inaccuracies in P^{u} and P^{nu} due to inclusion of a limited number of scatter orders partly cancel each other out. An even better transform could be accomplished by including more scatter orders in the MC calculation. Since the computation time typically increases linearly with the number of scatter orders, the calculation times would still be much shorter than with straightforward MC simulation. However, other investigators have observed that in situations where a high number of collisions per photon are likely, correlated sampling methods can become inaccurate [38]. Therefore, the method should be further validated in experiments where more orders of scatter are used for the calculation of correction factors.

We believe the basic principles of the method could also be applied to other collimator geometries and to other imaging modalities such as transmission CT and PET. However, the success of such applications will depend on the efficient calculation of scatter responses from objects with uniform density and on the availability of suitable MC simulators.

Acknowledgements

We thank an anonymous reviewer for outstanding comments, Sheila McNab for critically reading the document, Prof Dr Benjamin Tsui and Dr Karen LaCroix (University of North Carolina at Chapel Hill) for providing the MCAT phantom, Dr Michael Ljungberg (Lund University) for making available to us the SIMIND Monte Carlo software, Dr Tim Turkington (Duke Medical Center) for making available to us the image display software SPECTer, and Dr Styliyan Kalitzin (Utrecht University) for useful discussion.

Chapter 4

Acceleration of Monte Carlo SPECT simulation using Convolution-based Forced Detection

H.W.A.M. de Jong, E.T.P. Slijpen and F.J. Beekman
University Medical Center Utrecht
IEEE Transactions on Nuclear Science, Vol. 48, pp. 58-64, 2001

Monte Carlo (MC) simulation is an established tool to calculate photon transport through tissue in Emission Computed Tomography (ECT). Since the first appearance of MC a large variety of variance reduction techniques (VRT) have been introduced to speed up these notoriously slow simulations. One example of a very effective and established VRT is known as forced detection (FD). In standard FD the path from the photon's scatter position to the camera is chosen stochastically from the appropriate probability density function (PDF), modeling the distance-dependent detector response. In order to speed up MC we propose a convolution-based FD (CFD) which involves replacing the sampling of the PDF by a convolution with a kernel which depends on the position of the scatter event. We validated CFD for parallel-hole Single Photon Emission Computed Tomography (SPECT) using a digital thorax phantom. Comparison of projections estimated with CFD and standard FD shows that both estimates converge to practically identical projections (maximum bias 0.9% of peak projection value), despite the slightly different photon paths used in CFD and standard FD. Projections generated with CFD converge, however, to a noise-free projection up to one or two orders of magnitude faster, which is extremely useful in many applications such as model-based image reconstruction.

4.1 Introduction

Accurate simulation of Emission Computed Tomography (ECT) projection data is of paramount importance for several areas in ECT. Simulation of ECT projection data is often a good alternative to phantom experiments [4, 97, 128, 121, 48, 17, 79, 126]. This is true particularly in the case of experiments with complex activity distributions where it is not feasible to construct a representative physical phantom. Furthermore, in model-based iterative image reconstruction methods an accurate ECT simulator can be used as a forward projector to correct for image degrading effects like attenuation and scattering of photons and collimator and detector blurring [84, 46, 49, 13, 61, 65].

Monte Carlo simulation (MC) of photon histories is a well-established method for accurate modeling of ECT. In contrast to simulators based on point-spread function models, objects with non-uniform density can easily be handled by MC methods. In addition, a large variety of other details of the imaging process can be simulated in a realistic manner [126, 102, 2, 85]. Unfortunately, when photons are traced through the object in exact accordance with the underlying statistical physics, only one photon will be detected for every 10^5 emitted. All other photons will be absorbed in the collimator or miss the camera entirely, which means that the method is extremely time consuming. In order to increase the efficiency of MC simulation, variance reduction techniques (VRT) are very often applied [57]. One successful VRT is known as forced detection (FD) [4, 84]. In FD the photon, on leaving its scatter or emission position, is forced to pass through a collimator hole, which results in a tremendous increase of detected events. For the calculated particle flux to be an accurate estimate of the true (analog-calculated) flux, this detected event is weighted by the probability of the forced direction and by the probability that the photon will not be attenuated.

There are several reasons why it is desirable to generate, essentially, noise-free projections, even though this requires simulating a large number of photon histories. First of all, the application of VRTs alters the noise properties of the simulated projections. In order to obtain results with realistic noise properties, the correct noise is added to noise-free projection data. Furthermore, almost noise-free projections are desirable in model-based iterative reconstruction, in order to minimize the noise-level in the reconstructed images. Unfortunately, it still takes hours rather than minutes to obtain almost noise-free scatter estimates with MC, despite the use of known VRTs like FD. Therefore, it is very important to further reduce the time needed to generate almost noise-free projections.

The purpose of this work is to present a flexible and general method to speed up accurate MC simulation of ECT. To this end, the established technique of FD is combined with convolution-based modeling of collimator response and intrinsic camera resolution (convolution-based FD, CFD). The method of CFD can be combined with other VRTs, is easy to implement and maintains a high degree of accuracy in the MC simulation. The proposed method is similar to methods used in rotation-based projectors, which also use blurring kernels to include the camera response [47, 8]. However, the scatter modeling in these rotation-based projectors is always based on point-spread function models, which do not accurately include the effects of non-uniform mass densities during simulation. The calculation of down-scatter using point-spread function models is further complicated due to the significant effect of backscatter material [30, 68].

In the following section the implementation of standard FD and CFD are explained in detail and the methods of validation are described. The method of CFD is validated by comparing simulations generated by CFD with those generated using standard FD. In sections 3 and 4 the results of the validation in terms of accuracy and speed-up are presented and discussed.

4.2 Methods

In this section, we first describe the camera point-spread function which was used to model the collimator and detector resolution. Next, the Utrecht Monte Carlo System (UMCS) [33], which is used to generate the scatter projections, is described briefly. In addition, the CFD and standard FD methods are described in greater detail.

4.2.1 Camera Response Function

The resolution of a gamma camera is determined by the collimator parameters and the intrinsic detector resolution. Collimator blurring and intrinsic detector blurring can be modeled by a distance- dependent camera point spread function (PSF^{cam}). PSF^{cam} is defined by the collimator hole length l, the hole diameter d and the intrinsic detector resolution R_i [110]. The resolution in terms of Full Width at Half Maximum (FWHM) can be expressed as:

$$FWHM(z) = \sqrt{R_i^2 + (d + \frac{d}{l_e}z)^2}, \qquad l_e = l - \frac{2}{\mu} \tag{4.1}$$

Here z is the distance from the mean interaction depth in the detector, l_e is the effective hole length to correct for photons which penetrate through the edges of the collimator material and μ is the linear attenuation coefficient of the collimator material. It has been shown that a Gaussian is a good approximation for PSF^{cam} (e.g. [90]). Then, for a parallel-hole collimator the formula reads

$$PSF^{cam}(x,y)|_z = \frac{2\sqrt{\ln 2}}{\pi FWHM(z)} \exp\left(-\frac{4\ln 2\,(x^2+y^2)}{FWHM(z)^2}\right), \tag{4.2}$$

where (x, y) is the position on the detector plane. PSF^{cam} describes the probability density function (PDF) used for standard FD and the convolution kernel used for CFD.

4.2.2 Monte Carlo simulator

For generation of the scatter estimates we used a MC simulator developed by us: the Utrecht Monte Carlo System (UMCS) [33]. The UMCS is designed for fast photon transport simulation in SPECT. The code is written in C++. The UMCS uses a three-dimensional voxelized emission distribution map and electron density map. The simulations include Compton scatter and photo-electrical absorption. We validated UMCS using measurements of point-sources behind slabs, and projections and energy spectra of

extended source distribution generated with the SIMIND Monte Carlo code [83]. In this section we describe in detail how UMCS generates photon histories using standard FD and CFD.

Both in standard FD and in CFD, first the photon emission position is sampled from the emission distribution map. Thereafter an initial photon direction and path length is set, resulting in an interaction site (x, y, z). A copy of this original photon is created at this interaction site. In standard FD this copy is forced to escape from the object in a direction so that it can pass through the collimator and can be absorbed in the detector crystal. This is achieved by sampling a photon path from the PDF which is described by PSF^{cam}, which sets the detection position (x', y') and, hence the scatter angle θ' (Fig. 4.1, Top). The photon weight of the copy is corrected for the probability of not being absorbed photo-electrically, for the probability of scattering over the angle θ' using the Klein-Nishina function for Compton scattering, and for the probability that it will not be attenuated before it reaches the camera. Finally the photon weight of the copy is added to the projection bin corresponding to the detection position. Starting from the first interaction site, a new direction and path length of the original photon are set and again a copy of the photon is forced to be detected on leaving the new scatter site. This process is repeated until the original photon escapes the object (Fig. 4.1, Top). Standard FD has been described in several other papers and is implemented in most MC simulators. Note that there are slight differences between the various MC codes in the way in which the final photon path is sampled [4, 84, 57].

4.2.3 Implementation of Convolution-Based Forced Detection

The method of CFD differs only from standard FD in the way in which the detection of the copy of the original photon is simulated. As in standard FD a copy of the original photon is created at the interaction site (x, y, z). Instead of moving over a path that is randomly chosen by sampling the PDF, the copy is forced to move along the path that runs along the collimator hole axis (i.e. perpendicular to the camera face in the case of a parallel-hole collimator). The course followed by the original photon after scatter is equivalent to that using FD. The weight of the copy is corrected for the probability of not being absorbed photo-electrically, for the probability of scattering over the determined scatter angle θ (Fig. 4.1) using the KN-function and for the probability of not being attenuated before it reaches the camera. In order to facilitate convolution with the appropriate blurring kernel, the weight of the copy is stored in a three-dimensional sub-projection map. The storage bin in the sub-projection map (x, y, z) corresponds to the position of scatter site (x, y, z) in the electron density map (Fig. 4.1, Bottom). The size of the sup-projection bins is chosen equal to the voxel size in the electron density map.

After all photon histories have been calculated, the layers of bins in the sub-projection map parallel to the camera face $L(x, y)|_z$ are convolved layer-by-layer using the distance-dependent camera response function $PSF^{cam}(x, y)|_z$. Since $PSF^{cam}(x, y)|_z$ is modeled as a Gaussian, the two-dimensional convolution can be separated into two one-dimensional convolutions, without loss of accuracy. Separation of the kernel (15 x 15 pixels) speeds up the convolution by a factor of about 10. The projection is formed by adding all layers of the sub-projection map after convolution.

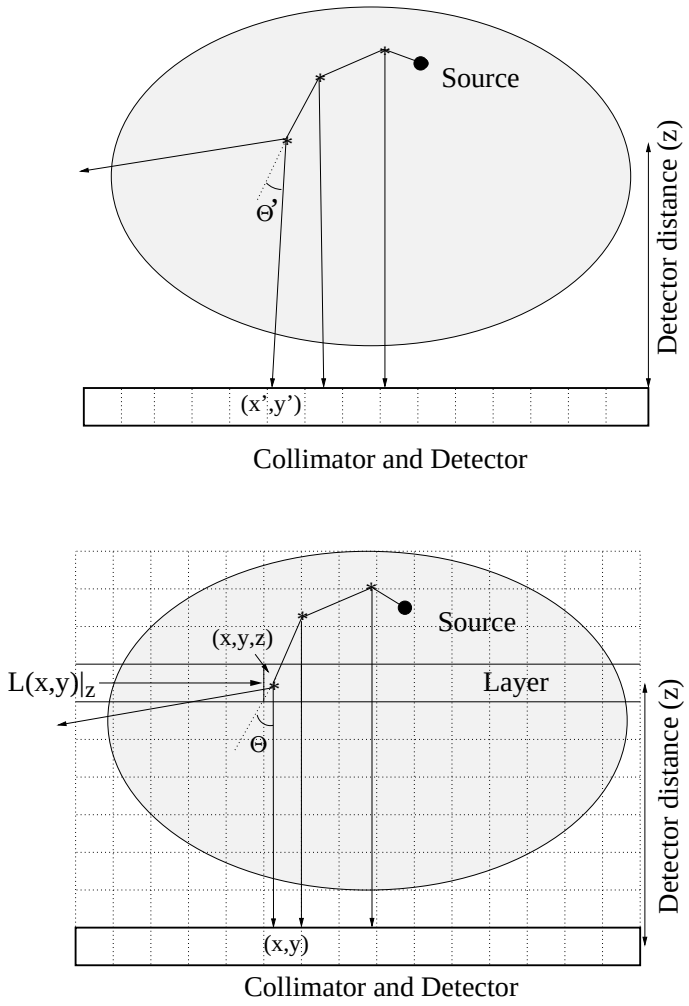

Figure 4.1: Monte Carlo SPECT scatter simulation using standard FD (upper figure) and using CFD (lower figure). Standard FD first samples a photon path from the PDF and adds the photon weight to the projection bin at (x', y') . In CFD the photon weight is stored in a map with layers $L(x, y)|_z$ corresponding to the photon's scatter position (x, y, z). Each layer in this map is convolved with the appropriate camera response given by $PSF^{cam}|_z$.

4.2.4 Simulations

In order to validate CFD, scatter projections of Tc-99m point sources and extended emission distributions in the Mathematical Cardiac Torso (MCAT) were generated [116] (Fig. 4.2).

The simulations included 5 orders of scatter. Projections were simulated with the camera position as drawn in Fig. 4.2. The collimator parameters used were typical for a general purpose parallel-hole (LEGP) collimator (d = 0.19 cm, l = 3.5 cm). A detector with an intrinsic resolution of R_i = 0.39 cm was simulated. The energy resolution was set to 10%, the energy window was centered at 140 keV and had a width of 20%. The voxel size was 0.25cm$\times$0.25cm$\times$0.25cm and the grid size was 128$\times$128$\times$128. So that the extended distribution would be representative for a cardiac study, we chose the relative activity concentrations of the background, the lungs and the myocardium in the ratio 1:2:10. All simulation were run on a MIPS4 R10000 200 MHz processor.

4.2.5 Validation Methods

First the accuracy of CFD was validated. To this end, high count noise-free projections estimated with CFD and standard FD were compared. These high count projections were based on 5×10^8 photon histories for the point source distribution and 2×10^9 photon histories for the extended source distribution. The high count standard FD projection is referred to as reference projection.

Furthermore, the noise and error properties of CFD and FD estimated projections were compared by taking the Normalized Mean Square Errors (NMSE) in the estimated projections using the reference projection:

$$NMSE = \sum_i (e_i - r_i)^2 \tag{4.3}$$

where e_i represents the normalized pixel values of the estimated projection and r_i represents the normalized pixel values of the reference projection, and i runs over all projection bins. Normalization of the projections was achieved by dividing the projections by the number of generated photon histories for that projection. The NMSEs were determined for a series of projections with increasing numbers of simulated photons and thus simulation running time. Hence, the NMSE includes both the noise in the projections and the error in the projections generated using CFD, due to the approximation used. The speed-up factor of CFD was determined by comparing the simulation times of CFD and FD estimated projections at equal NMSE.

4.3 Results

The accuracy of CFD was investigated by simulating almost noise-free (5×10^8 photon histories) point-source projection data. Fig. 4.3 shows profiles of a high-count CFD and standard FD generated projections of point sources both on a linear and semi-logarithmic scale. The CFD-generated projection is in excellent agreement with the FD-generated projection. Only in the maximum of the responses very small differences can be seen between CFD and standard FD-based projections. The maximum bias in the CFD generated projection is 0.91% of the peak projection value of the standard FD generated projection.

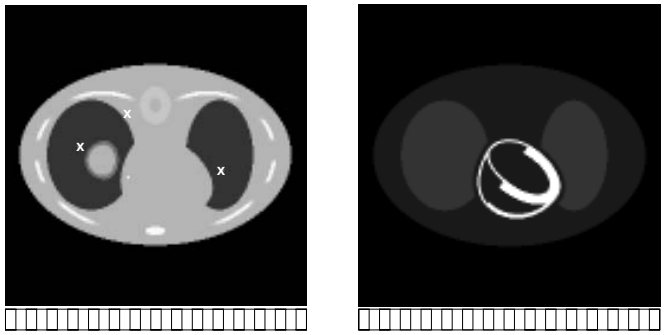

Figure 4.2: Digital phantom and camera position. Left: electron density of the MCAT phantom with the position of the point sources represented by cross-hairs. Right: extended emission distribution.

Simulated projections of the extended emission distribution in the MCAT phantom are shown in Fig. 4.4. The estimated projections are based on 10^6 or 10^7 photon histories generated using CFD and standard FD. As a reference, a projection based on standard FD and 2×10^9 photon histories is included.

It is clearly visible that for equivalent numbers of simulated photon histories, the estimated projections generated with CFD are less noisy than estimated projections generated with standard FD. This is confirmed by the image profiles of point source projections shown in Fig. 4.5 and the profiles of the extended source projections in Fig. 4.6. The profiles are composed by summing three adjacent projection rows. The white line in Fig. 4.4 indicates the location of the image profile in the estimated projections of the extended source. Estimated projections generated by CFD are much smoother, and are closer to the reference projection than those generated by standard FD for equal numbers of photon histories. In CFD every photon is projected as a blurring kernel, which initially will cause correlated lumpy noise-textures if an insufficient number of photon histories is simulated. This effect can be seen clearly in the CFD-generated projection of 10^6 photon histories in Fig. 4.4, but appears to be no longer visible when 10^7 photon histories are generated.

Fig. 4.7 shows the NMSE as a function of the number of photon histories for CFD and standard FD. For equal numbers of photon histories, CFD produces projections which have an NMSE that is more than ten times smaller than that for standard FD. Fig. 4.8 shows the speed up of CFD relative to standard FD as a function of NMSE and number of generated photon histories; depending on NMSE or number of simulated photon histories, CFD reaches the same error level from 20 to 90 times faster than standard FD. The more photon histories that are simulated the larger the speed-up factor is. This can be explained at least partly by the fact that in CFD a fixed amount of time is needed for convolution.

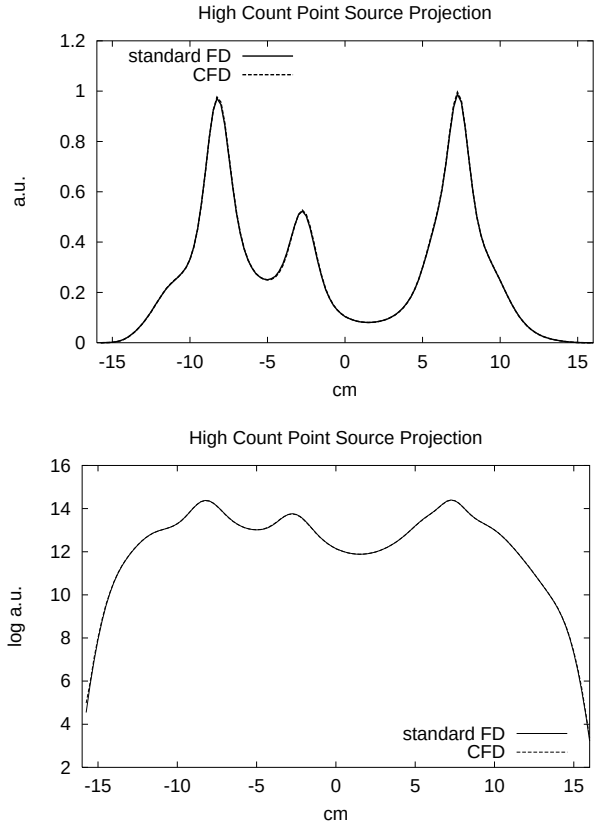

Figure 4.3: Comparison of image profiles of high-count (5×10^8 photons) projections of point sources in MCAT phantom, for CFD and standard FD.

4.4 Discussion

We have shown that a MC simulator using convolution-based forced detection (CFD) converges to noise-free projections up to one or two orders in magnitude faster than if standard forced detection (FD) is used. However, if CFD is used, approximations have to be made with regard to photon transport. First of all, all photons are forced to move to the camera along the collimator hole axis instead of being randomly projected within the finite collimator acceptance angle. Although this slightly alters the path from the scatter event to the detector, and hence the attenuation on that path and the detection position, the difference between the photon paths in CFD and standard FD is extremely small. Since low-energy general purpose (LEGP) collimators as used in this study have an acceptance angle of about 2°, the photon paths of detected photons do not deviate much from the paths along the collimator hole axis. As a consequence of the different photon paths

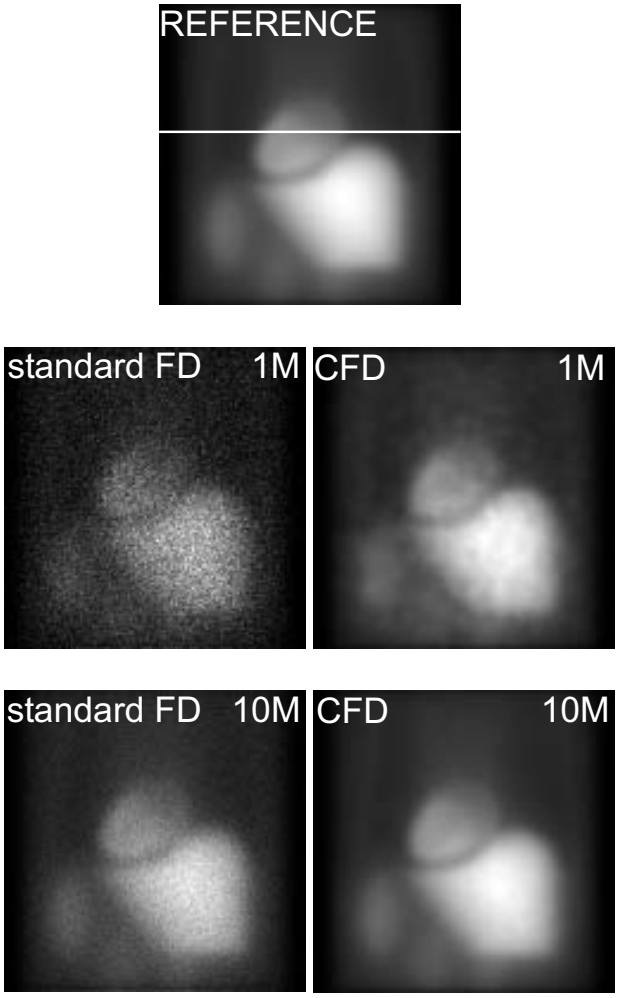

Figure 4.4: Simulated scatter projections of MCAT extended distribution for standard FD (left) and CFD (right). Top row: Reference projection based on 2×10^9 photon histories. The white horizontal line represents position of the image profiles shown in figure 4.6. Second row: based on 10^6 photon histories. Bottom row: based on 10^7 photon histories.

in CFD and FD, the computed scatter angles (Θ and Θ' in Fig. 4.1) of photons before detection slightly differ as well. The mean scatter angles of all photons scattering in (x, y, z) however, converge in CFD to the same mean scatter angles in standard FD, since in standard FD all photons are distributed symmetrically around the angle used in CFD.

To justify these approximations we have shown that CFD-generated projections converge to projections that are extremely close to those obtained with standard FD. Furthermore, when using high resolution collimators with a larger acceptance cone instead of

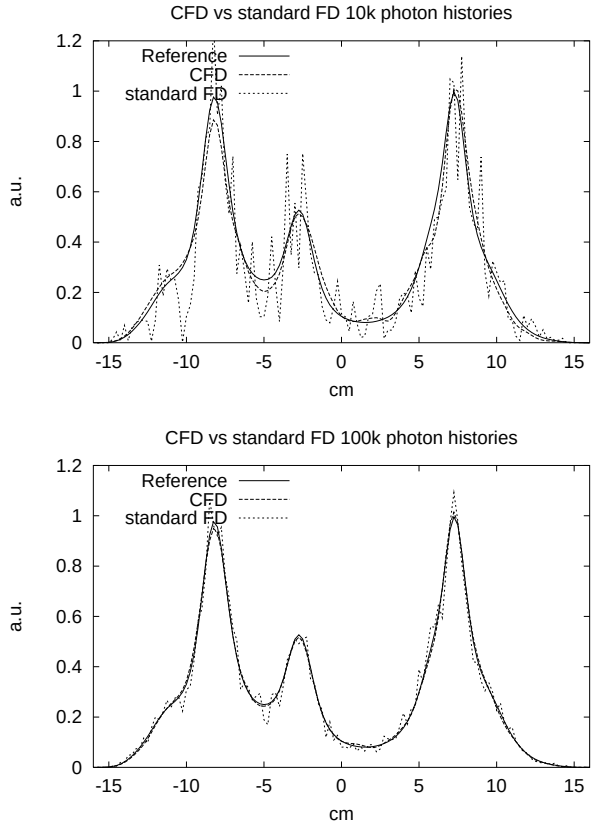

Figure 4.5: Image profiles of point source projections for equal numbers of photon histories generated by CFD and standard FD compared with the reference projection based 5×10^8 photon histories. Top: 10^4 photon histories. Bottom: 10^5 photon histories.

an LEGP collimator, we expect that the deviation of CFD from standard FD will further diminish.

In this study we used a distance-dependent camera response, which included collimator blurring and intrinsic camera resolution. It is possible that the blurring kernel might also be modified to include lead x-rays, as required to simulate Tc-99m/Tl-201 Dual Isotope SPECT, or collimator penetration, as occurs in imaging high energy isotope distribution. In these two cases photon paths often deviate more from the path parallel to the collimator hole axis as compared to the situation described in here. Therefore we expect a larger error in the attenuation on the photon path from scatter position to detection position as compared to the situation described in this paper.

Fast convergence of the simulated scatter projections is mandatory if MC is to be used for model-based iterative reconstruction. The projection that is generated using CFD and

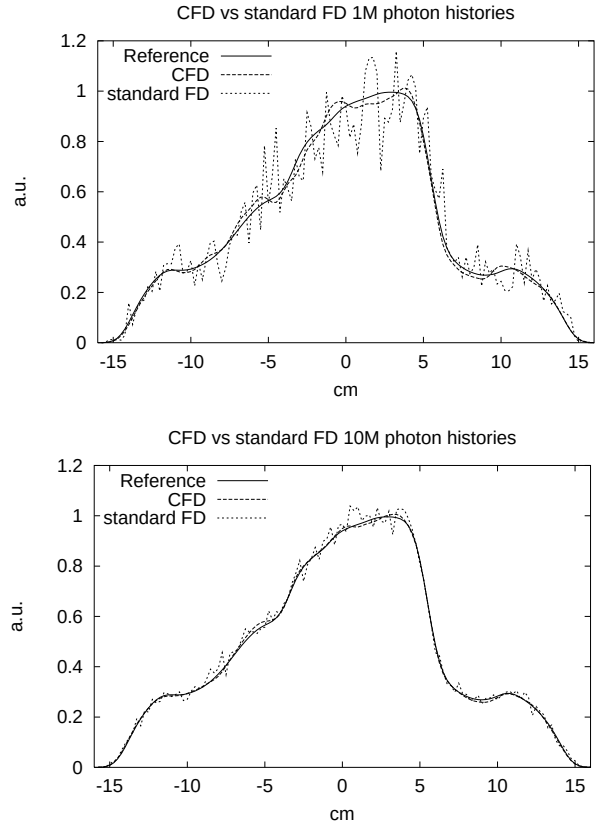

Figure 4.6: Image profiles of point-source projections for equal numbers of photon histories generated by CFD and standard MC compared with the reference projection based 5×10^8 photon histories. Top: 10^6 photon histories. Bottom: 10^7 photon histories.

is based on 10^7 photon histories is very close to the reference projection (Fig. 4.4). The speed up achieved by using CFD is then already more than 80 times (Fig. 4.8). For use in model-based iterative reconstruction the projections based on 10^7 photon histories satisfy the desired noise level which is very low as compared to the noise level in measured projections. Further research will be required to determine if a lower number of photons is sufficient for reconstruction. Using a MIPS4 R10000 200 MHz processor, UMCS with CFD requires approximately 2.3 minutes to generate a scatter projection based on 10^7 photon histories and 5 orders of scatter simulating a 64^3 grid. When simulating a 128^3 grid, this simulation time will be 30 minutes. Simulation times reduce roughly by a factor of 2.5 when only first and second order scatter is simulated, which accounts for about 99% of the total counts in the Tc99m photo-peak window.

Nevertheless, the time needed to calculate almost noise-free projections is still some-

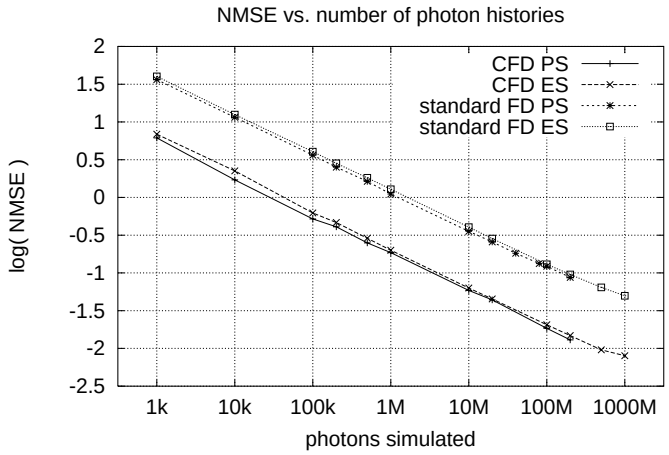

Figure 4.7: NMSE as a function of the number of generated photon histories for point source projections (PS) and extended source (ES) projections on a log-log scale.

what too long for routine clinical implementation in iterative scatter correction, especially when the projections are calculated for all angles and each iteration anew. However, there are some simple ways in which the amount of computation time can be reduced. For example (i) it is possible to calculate multiple projections in significantly less time, since the selection of scatter positions and the calculation of attenuation over the trajectory between emission and scattering can be re-used for more projection angles. (ii) For the case of model-based image reconstruction, only the differences in these estimates due to change in the iteration have to be calculated, instead of completely recalculating the projections for each new iteration. This would involve the tracking of only a fraction of the photon histories required for complete scatter estimates. (iii) As mentioned before, correlated photon tracking tremendously speeds up MC, as demonstrated in [5]. However, correlated tracking is only useful when a fast simulator, such as that used for photopeak scatter projection [17], is available.

A major advantage of CFD is that the technique can be added to other VRTs, such as stratification, forced scatter, Russian roulette and correlated MC which have been validated in the past [57], [5].

4.5 Conclusion

A practical method for speeding up MC simulations (CFD) has been developed and evaluated. In CFD forced detection is combined with a convolution operation to model collimator blurring and intrinsic resolution. Projections generated with CFD converge to a noise-free projection one up to two orders in magnitude faster than if standard FD is used.

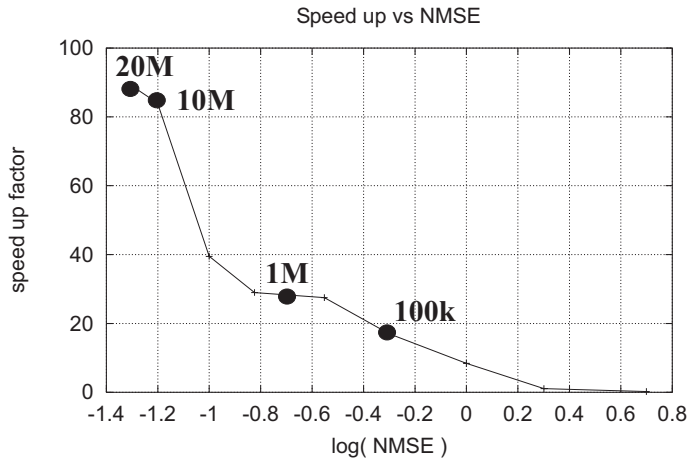

Figure 4.8: Speed up as a function of NMSE for extended source projections. At some points in the graph the required number of generated photon histories when using CFD is shown.

This is extremely useful for several applications of MC ECT simulation, such as the simulation of extended distributions and for model-based image reconstruction. In addition, CFD is straightforward to implement, and can easily be combined with other variance reduction techniques.

Chapter 5

Rapid SPECT simulation of down-scatter in non-uniform media

H.W.A.M. de Jong and F.J. Beekman
University Medical Center Utrecht
Physics in Medicine and Biology, Vol. 46, pp. 621 - 635, 2001

A rotation-based Monte Carlo (MC) simulation method (RMC) has been developed, designed for rapid calculation of down-scatter through non-uniform media in SPECT. A possible application is down-scatter correction in Dual Isotope SPECT. With RMC, only a fraction of all projections of a SPECT study has to be MC simulated in a standard manner. The other projections can be estimated rapidly using the results of these standard MC calculations. For efficiency, approximations have to be made in RMC with regard to the final scatter angle of the detected photons. Further speed-up is obtained by combining RMC with convolution-based forced detection (CFD), instead of forced detection (FD), which is a more common variance reduction technique for MC.
The RMC method was compared with standard MC for Tc-99m down-scatter in a Tl-201 window (72 keV $\pm$ 10%) using a digital thorax phantom. The resulting scatter projections are in good agreement (maximum bias a few percent of largest value in the projection), but RMC with CFD is about 3 orders in magnitude faster than standard MC with FD and up to 25 times faster than standard MC with CFD. Using RMC combined with CFD, the generation of 64 almost noise-free down-scatter projections (64×64) takes only a couple of minutes on a 500 Mhz Pentium processor. Therefore, rotation-based Monte Carlo could serve as a practical tool for down-scatter correction schemes in Dual Isotope SPECT.

5.1 Introduction

Dual-Isotope (DI) SPECT enables the simultaneous monitoring of different (patho)-physiological processes and which are represented by different radio-labeled compounds. In addition, DI SPECT avoids problems with the registration between the images of the different isotopes, and it reduces patient discomfort and scan times. A typical example is found in nuclear cardiology, where DI SPECT offers an opportunity for simultaneous 'rest' and 'stress' myocardial perfusion imaging. Tl-201-thallous chloride is preferable used to study the perfusion at rest, and a Tc-99m-labeled compound (e.g. Tc-99m-tetrofosmin or Tc-99m-sestamibi) for the stress study. However, complications due to photon cross-talk or down-scatter are inherent to DI SPECT; photons of the higher energy isotope can be detected in the photo-peak window of the lower energy isotope, due to energy loss in scatter interactions. For example, Tc-99m/Tl-201 DI SPECT for cardiac perfusion imaging is hampered by down-scatter of Tc-99m photons (emitted at 140 keV) in the lower Tl-201 photopeak window (centered at 72 keV), which causes an overestimation of the Tl-201 distribution (e.g. [53], [72], [124]). It is therefore often necessary to correct for down-scatter. To this end, model-based correction methods have been proposed which require the calculation of down-scatter projections (e.g. [12], [68]).

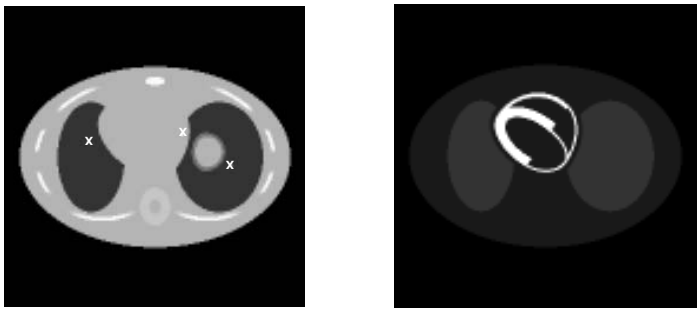

Figure 5.1: Cross section of the MCAT phantom at mid-ventricular level. Left: mass density with positions of point sources represented by cross hairs. Right: extended activity distribution in the heart, lungs and background.

Monte Carlo simulation (MC) of photon histories is a general and well-established method for calculating scatter in SPECT projections. In contrast to methods based on point-spread function models, effects due to non-uniform mass density of the emitting object can be handled more accurately using MC methods [126], [102], [2], [85]. Simulated down-scatter projections of the Mathematical Cardiac Thorax (MCAT) phantom (Fig. 5.1) with uniform and non-uniform mass density, illustrate the importance of including the effects due to non-uniform mass densities (Fig. 5.2). This figure shows an anterior view of a Tc-99m extended distribution acquired in a 72 keV $\pm$ 10% energy window. Clearly visible is the local reduction in down-scatter yield due to the low mass density of the lungs. The error in the simulation based on the uniform density distribution is up to 30% of the largest pixel value in the projection. Besides the effects due to non-uniform mass densities, an accurate down-scatter simulation must include all relevant scatter events. For

instance, back-scatter events are a significant part of the total down-scatter [30]. In addition a relatively high number of scatter orders have to be simulated, as shown in Fig. 5.3; the detected energy spectrum of an extended Tc-99m distribution in the MCAT phantom shows the contributions made by the different orders of scatter. The spectrum was simulated using a camera at a center-of rotation distance of 21 cm with a VXHR collimator and a camera energy resolution of 10%. It is remarkable that Tc-99m photons which have scattered up to 8 times make a significant contribution to the down-scatter contamination in the Tl-201 energy window.

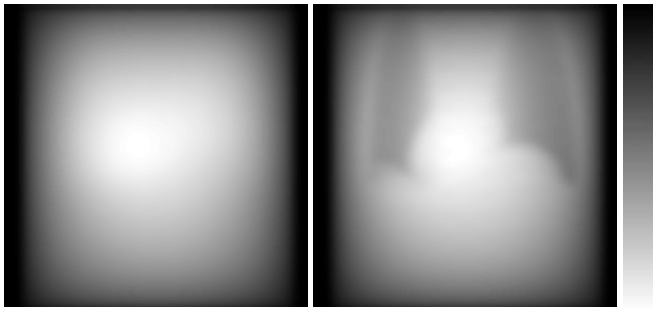

Figure 5.2: The influence of including the effect of non-uniform density distribution of the object. Left: down-scatter projection of the uniform MCAT phantom. Right: down-scatter projection of the non-uniform MCAT phantom.

To make the - notoriously slow - MC simulation feasible for scatter correction in SPECT, acceleration methods denoted by variance reduction techniques (VRTs) are often applied [57]. A very popular VRT is forced detection (FD) to increase photon yield on the detector [4], [84]. More recently proposed VRTs include convolution-based forced detection (CFD) for the efficient modeling of camera resolution [34], and correlated photon tracking combined with CFD [5] which allow an extra acceleration of about two orders of magnitude. These methods have been found to be accurate for scatter simulations in the photo-peak window. When a combination of these VRTs is used, MC becomes computational feasible for fully 3D scatter correction in routine clinical iterative image reconstruction.

MC simulation of down-scatter is computationally more demanding than MC simulation of scatter in the photo-peak window. This is mainly caused by the fact that high order scatter events significantly contribute to down-scatter. The purpose of this work is to present and validate an acceleration method for MC simulation of down-scatter in SPECT (rotation-based Monte Carlo simulation (RMC)).

In the following section, RMC and its implementation are explained in detail, and the validation procedure for RMC is described. In the results section comparisons of RMC with standard MC are presented in terms of accuracy and speed-up.

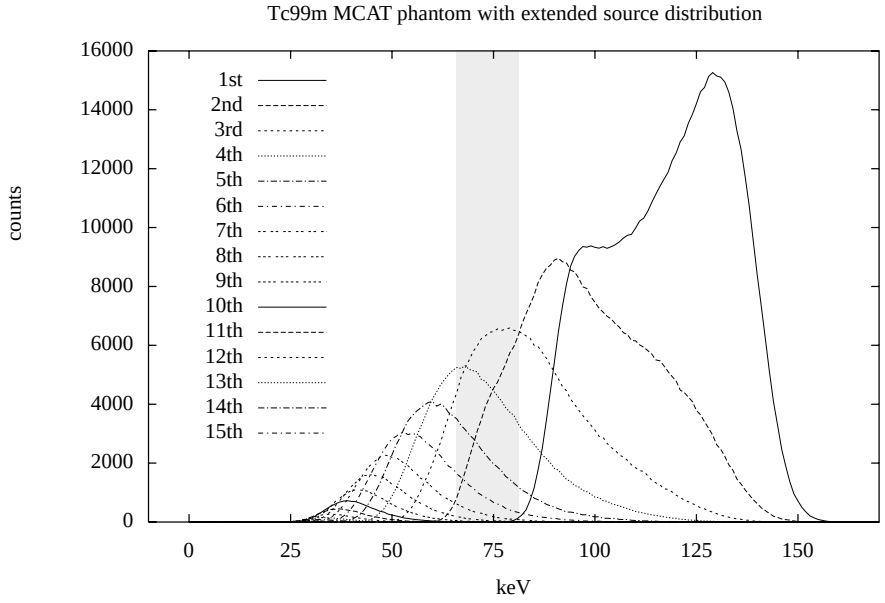

Figure 5.3: Simulated energy spectrum of a Tc-99m filled MCAT phantom, separated into components of scatter orders. Photons with scatter order up to 8 can contribute significantly to the down-scatter in the 72 keV window (shaded region).

5.2 Methods

A SPECT image is reconstructed from a series of projection images acquired at different angles. For clinical applications the number of projections typically ranges from 30 to 120. In the SPECT simulation method described in this section (RMC), only a few projections (two to four) are simulated using more or less standard MC calculation of photon histories. In the sequel, these projections will be referred to as base-projections. In this section it will be shown how the remaining projections ('off-base projections') can be generated efficiently by re-using the results of the MC calculations already performed for the base projections.

For the MC calculations we used a simulator developed by us: the Utrecht Monte Carlo System (UMCS) . The UMCS is designed for fast photon transport simulation in SPECT. The code is written in C++. The simulations include Compton scatter and photo-electrical absorption. We validated UMCS using measurements of point-sources behind slabs, and projections and energy spectra of extended source distribution generated with the SIMIND Monte Carlo code [83]. The results of these validations are reported in [33].

5.2.1 Monte Carlo Simulation of a Base Projection

The UMCS uses a three-dimensional emission-distribution (e-map), a mass density distribution (ρ-map), the geometry and characteristics of the SPECT system and the probability density functions (PDFs) describing the physics of photon transport, including emission, scatter and detection processes. This input is used to generate a large number of photon histories (typically tens of millions).

In this paper we will describe an implementation which incorporates CFD [34]. The CFD method results in considerable faster convergence to noise free projections than does the use of FD. Broadly outlined, the implementation of CFD is similar to that of FD [4, 83]. However, to speed up convergence, CFD projects photons as Gaussian basis functions in order to model the distance-dependent camera resolution, whereas FD projects photons as delta functions with detector positions sampled according to a PDF that models the camera resolution.

Simulation of photon histories

Generation of photon histories is implemented as follows and is similar to the implementation of many other codes [4], [84], [57]. First the emission position s_0 of a photon is chosen randomly from the e-map. Using uniformly distributed random numbers, the PDFs set an emission direction and a photon path length in water. These determine, together with the ρ-map, the first photon interaction position s_1. Attached to the photon is a Photon History Weight (PHW), which represents the probability of the photon existence, and which is set to one at emission. At the photon interaction position s_1, the PHW is multiplied by the energy (E) dependent probability (1-$P_{pe}(E)$) that the photon will not be absorbed in a photo-electric interaction. Since only Compton scatter and photo-electric interaction are simulated, the photon is forced to Compton scatter.

Next, the probability that this photon will be detected at detection position p_1 after Compton scattering at s_1, is determined (detection probability, DP_1). Starting from s_1, a new direction (using a PDF according to the Klein-Nishina (KN) function for Compton scatter), a new energy and path length for the original photon are set, which results in a new scatter position s_2. The PHW of the original photon is again multiplied by the probability that it will not be absorbed in a photo-electric interaction, and the DP_2 for detection on leaving s_2, is calculated. This process is repeated for higher order scatter until the photon escapes from the object or its energy drops below a specific minimum photon energy (e.g. 50 keV).

Generally, the DP_n of a photon having its n-th scattering event in s_n and being detected in p_n is formulated as follows:

$$DP_n = S_n \times A_n \quad \text{with} \tag{5.1}$$

$$S_n = PHW_n \times KN(\theta) \times P_{det}(E(\theta)) \quad \text{and} \tag{5.2}$$

$$A_n = e^{-\mu(E(\theta)) \int_{s_n}^{p_n} \rho(l) dl} \tag{5.3}$$

where θ is the required scatter angle for the photon be detected at p_n, $E(\theta)$ is the energy of the photon after scattering (computed using the Compton formula), $KN(\theta)$ is

the probability that the photon Compton scattered over θ (according to the KN-function), and $P_{det}(E)$ is the probability that the scattered photon with energy E will be recorded in the energy window. P_{det} is further determined by the energy window settings and the camera energy resolution. The attenuation on the path from s_n to the detector p_n is denoted by A_n, and depends on the integrated mass density $\int_{s_n}^{p_n} \rho(l)dl$ on that path, and on the energy dependent attenuation coefficient $\mu(E(\theta))$. PHW_n is the photon history weight just after scattering at s_n. As will be described below in detail, the terms S_n are stored in such a way that they can also be used for the calculation of off-base projections.

Generation of the S-map

The terms S_n, calculated at every photon scatter event, are voxel-wise summed to their scatter positions, in what will be referred to as the S-map (Fig. 5.4, Left). The S-map overlays the ρ-map and e-map and contains in every voxel the sums of S_n (from now on denoted by S_{tot}), summed over all photons which scattered from that voxel position towards the base projection. By rotating the S-map and multiplying it voxel-by-voxel by the projection-angle dependent attenuation A_n (5.3), one uses the S-map to estimate other projection angles, without recalculating complete photon paths through the object. As equations (5.2) and (5.3) show, S_n and A_n depend partially on the individual scatter angles θ of the photons. Because the information about these individual scatter angles of the photons θ is lost after summing the terms S_n, the attenuation coefficient $\mu(E(\theta))$ is approximated as will be explained in the next section. Furthermore, although a range of projection angles is estimated using the same scatter map, the individual scatter angles θ cannot be changed after the terms S_n have been summed in the scatter map. This second approximation does not have a strong effect on the simulation of down-scatter, as will be shown in the results section.

Central μ approximation for attenuation of photon ensembles

In order to construct the base projection from the S-map, the terms S_{tot} stored in the S-map are multiplied by A_n. However, since only S_{tot} is stored, it is no longer possible to correct photon weights exactly according to the individual photon energy. The assumption is made, that the attenuation can be approximated by the μ corresponding to the central energy of the window (central μ approximation). Hence, in the case of a Tl-201 energy window (centered at 72 keV), $\mu(E(\theta))$ in equation (5.3) is replaced by $\mu(E = 72keV)$.

The image profiles of projections in Fig. 5.2.1 show that both for the point-sources and for the extended activity distribution in the MCAT phantom, the projections generated with the central μ approximation are indistinguishable from the projections generated with standard MC using CFD. The MC simulation shown in this figure was made using a Tc-99m source distribution, recorded in an energy window centered at 72 keV and with a width of 20%. The maximum error in the entire projection is only 0.03% of peak projection value, which shows that the central μ approximation can be used with only a neglectable loss of accuracy.

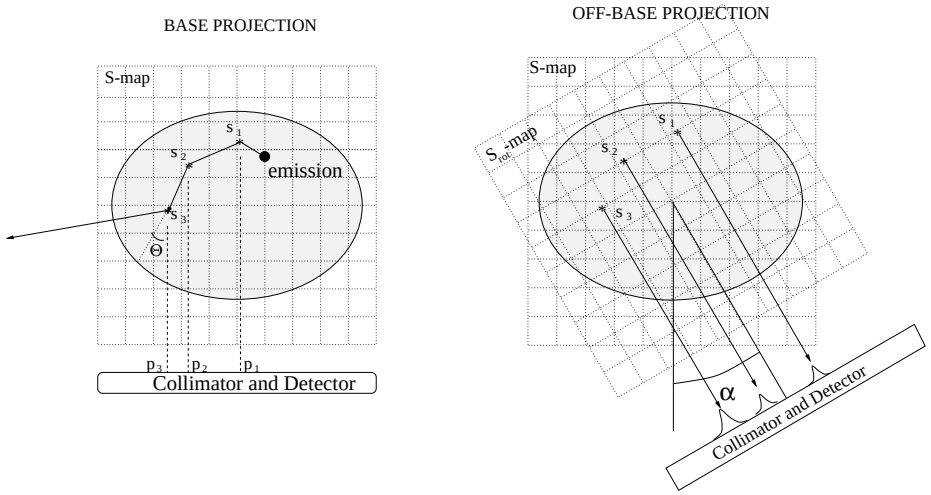

Figure 5.4: Illustration of rotation-based Monte Carlo simulation. Left: For generation of the base projection, the photons are traced through the object. At each scatter position s the scatter probability is calculated and summed to the S-map at position s. Right: A projection at a different angle than the base projection, is calculated by rotating the S-map and multiplying all terms in the rotated S-map by the attenuation. After this the layers in the rotated S-map are blurred with a distance dependent kernel, to include collimator and detector blurring.

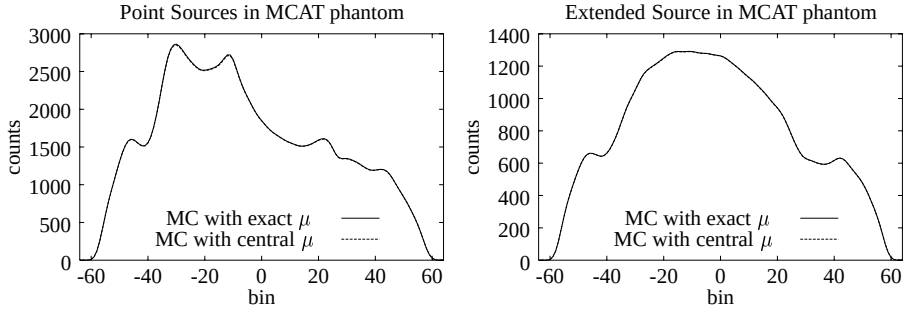

Figure 5.5: Comparison of exact μ and central μ approximation for generating down-scatter estimates of the point sources (left) and extended source (right).

Convolution-based Forced Detection

In order to include effects of collimator and detector response, after multiplication with the attenuation, the S-map is blurred layer-by-layer using a distance-dependent Gaussian kernel, and all layers are summed to form the base projection. This method is referred to as convolution-based forced detection (CFD). When using CFD, the photon detection

position p on the camera is always on the line through s, running along the collimator hole axis (i.e. perpendicular to the camera face when the collimator is a parallel-hole type, Fig. 5.4). Validations of CFD have demonstrated that this approximation in the photon transport leads to negligible differences as compared to FD.

5.2.2 Estimation of an Off-Base Projection

The off-base projections use the terms S_{tot}, which were stored in the S-map while the base projections were calculated. The off-base projections are generated using following steps (see also the right frame of Fig. 5.4):

1. The S-map is rotated over α degrees ($S_{tot,\alpha}$), α being the difference between the base projection angle and the off-base projection angle.
2. The terms $S_{tot,\alpha}$ in the rotated S-map are corrected for attenuation on the path towards the detector by multiplying them by the correct term $A_{n,\alpha}$. The central μ approximation is used, similar to the construction of the base projection.
3. Similar to the construction of the base projection, the rotated S-map is blurred layer-by-layer using a distance-dependent kernel and finally all blurred layers are summed to form the off-base projection (CFD).

The base projections are chosen equidistant over the total projection arc. For example, if two base projections are chosen to generate all projections with an acquisition angle of 360 degrees, the angle between the base projections is set to 180 degrees. Then the S-map of the base-projection that has an angle closest to the off-base projection angle is used to calculate the off-base projection. For projection angles more distant from the base projection angles, significant approximations are made in DP, justifying the validation of the effects on down-scatter projections.

5.2.3 Validation

The accuracy of RMC was validated by comparing down-scatter simulations based on RMC and based on standard MC using CFD. For this purpose Tc-99m point-sources as well as a Tc-99m extended activity distribution in the digital MCAT thorax phantom were used [116] (Fig. 5.1). Sixty-four projections were calculated. The energy window was centered around 72 keV and had a width of 20%. The simulations included 10 orders of scatter and 10^7 emitted photons, which resulted in about 2.10^7 detected photons per projection. When using CFD, this number of photon histories is sufficient to generate almost noise-free scatter projections. The acquisition arc was 360 degrees. The camera parameters were typical for an ADAC vertex camera system equipped with VXHR collimators, and the energy resolution was set to 10%. A voxel size of 6 mm $\times$ 6 mm $\times$ 6 mm and a grid size 64 $\times$ 64 $\times$ 64 was used in the simulations as well as a voxel size of 3 mm $\times$ 3 mm $\times$ 3 mm and a grid size 128 $\times$ 128 $\times$ 128. The grid and voxel size of the S-map were set equal to the grid and voxel size of the ρ-map. All simulations were performed with two, three or four base projections, in order to show the influence the number of base projections had on the accuracy of the resulting projections.

Table 5.1: Different error measures for the case two, three or four base projections are used or only the central μ approximation.

source distribution	MCAT		Points	
Simulation grid	64	128	64	128
	2 Base Projections			
max. error	4.9%	5.2%	6.1%	5.4%
abs. error	1.9%	2.2%	2.2%	2.6%
pos. error	1.7%	0.5%	1.6%	0.5%
neg. error	0.3%	1.7%	0.6%	2.1%
	3 Base Projections			
max. error	3.7%	3.7%	4.6%	3.7%
abs. error	1.6%	1.7%	1.8%	1.8%
pos. error	1.0%	0.9%	1.0%	0.9%
neg. error	0.6%	0.8%	0.8%	0.9%
	4 Base Projections			
max. error	2.8%	2.7%	3.8%	2.8%
abs. error	1.4%	1.4%	1.6%	1.5%
pos. error	1.0%	0.9%	1.1%	1.0%
neg. error	0.5%	0.5%	0.6%	0.5%
	Central μ			
abs. error	0.1%	0.3%	0.2%	0.3%
pos. error	0.1%	0.3%	0.2%	0.3%
neg. error	0.0%	0.0%	0.0%	0.0%

5.3 Results

5.3.1 Accuracy of RMC

A comparison between RMC and standard MC using CFD is shown in Figs. 5.6 and 5.7 . The figures show only off-base projections with the largest angle α from the base projection. Hence, this angle is 90°, 60° and 45° in the case of two, three and four base projections respectively. These projections are most probably the projections with the largest error ('worst case'), since the approximation that the scatter probability ($KN(\theta)$), energy ($E(\theta)$) and as a consequence $\mu(E(\theta))$ are scatter-angle dependent, is less valid at larger angle differences between base and off-base projections. Clearly, the calculation of only two base projections (Top frames Figs. 6, 7, 8 and 9) results in a larger error as compared to the calculation of four base projections (Bottom frames Figs. 6, 7, 8 and 9).

The maximum error in pixel value, expressed as a percentage of the peak projection value in the standard MC projections, is shown in table 5.1. This table also includes the mean positive error (including all positive differences), the mean negative error (including all negative differences) and the mean absolute error (sum of all absolute differences), all as as a percentage of the total pixel value in the entire projections. The error measures are presented as a function of the number of base projections, and in the case only the central μ approximation is used.

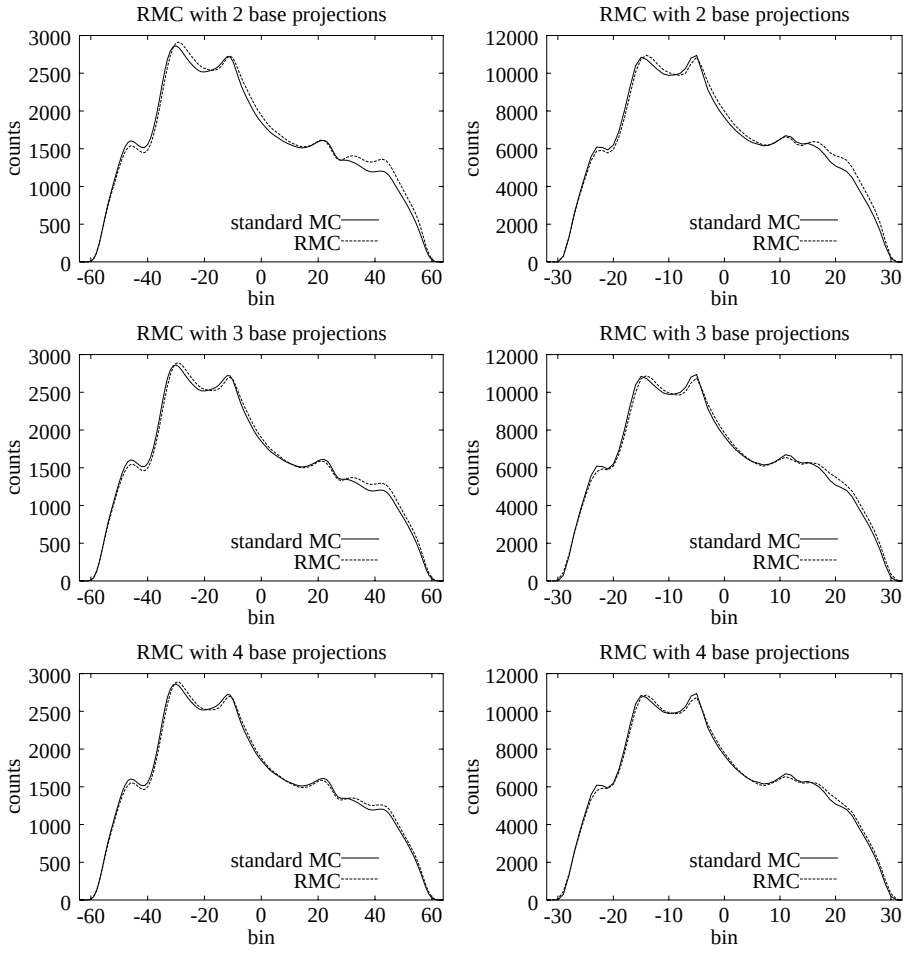

Figure 5.6: 'Worst case' RMC generated down-scatter estimates of point-sources in the MCAT phantom for two (top), three (center) and four (bottom) base projections simulated with standard MC with a 128^3 simulation matrix (Left) or a 64^3 simulation matrix (Right).

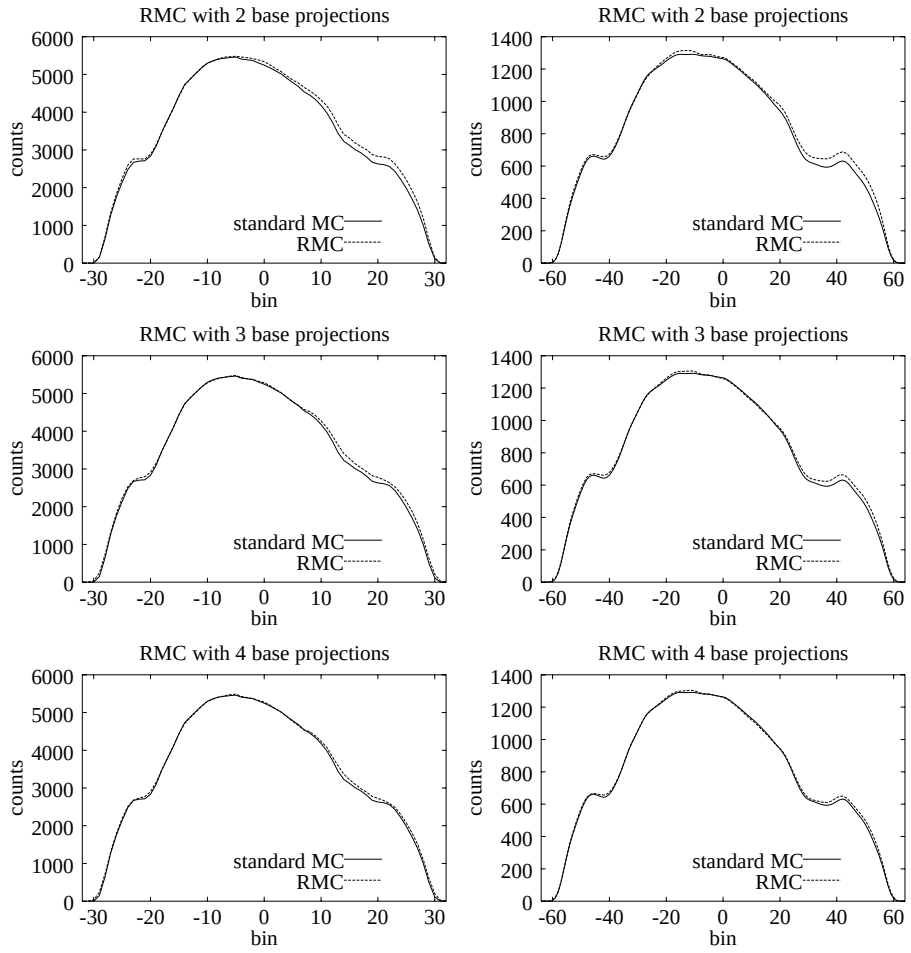

Figure 5.7: As in Fig. 6 but for the MCAT extended emission distribution.

5.3.2 Acceleration obtained by RMC

The simulation times for MC simulations using the different VRTs are shown in table 5.2 and are based on a matrix of 64^3, 64 projections, 10 orders of scatter. All simulations have an equivalent low noise-level (almost noise-free). The simulation takes more than 100 hours with standard MC using FD, whereas standard MC using CFD takes only 80 minutes, since this requires less photon histories [34]. Using the central $/mu$ approximation traces ensembles of photons from their last scatter position to the detector, which is faster than tracing all photons individually on that path as in CFD. Further reduction of simulation times is achieved with RMC, since only a few projections have to be generated using standard MC calculations. Depending on the number of base projections, the

Table 5.2: Simulation times and speed-up factors for down-scatter calculation of an extended Tc-99m distribution, using the different VRTs. All simulations have an equivalent noise-level. The simulation times of MC simulation using RMC are given for two, three and four base projections (bp).

applied VRT	time	speed up compared to FD	# photon histories per projection
FD	372320 s	1	1.10^9
CFD	4750 s	80	2.10^7
CFD, central μ	3964 s	98	2.10^7
CFD, central μ, RMC 4 bp	312 s	1220	2.10^7
CFD, central μ, RMC 3 bp	251 s	1516	2.10^7
CFD, central μ, RMC 2 bp	189 s	2016	2.10^7

computation time for RMC is as short as 3 minutes. Therefore RMC with CFD is more than 1000 times faster than standard MC with FD and up to 25 times faster than standard MC with CFD.

5.4 Discussion

An efficient acceleration method has been presented for MC simulation of down-scatter projections (rotation-based Monte Carlo, RMC). The method is based on simulating only a fraction of all projections by standard MC, and then taking a short-cut to calculate the other projections.

In order to make RMC efficient, some approximations were made regarding the physics of photon transport:

- Attaching approximate attenuation coefficients to all photons on their path to the detector ('central μ approximation') makes it possible to store sums of the detection probability (S) in an S-map instead of storing every detection probability individually. In this paper is shown that this approximation is accurate for down-scatter simulation.

- The next approximation in the detection probability is the KN-probability $KN(\theta)$ for Compton scattering towards the detector. This probability is calculated exactly for the base-projection. By rotating the S-map for off-base projections, one changes θ and hence, $KN(\theta)$ will also have to be changed for off-base projections. However, the approximation in the KN-probability takes advantage of the fact that every projection pixel is a sum of terms S of a large number of photons. A change in the scatter angles (θ), due to a change in projection angle (α), will lead to an increase in one part of the terms in S_n and a decrease in the other part, which partly neutralizes the total error induced in the S_{tot} values. Even with a large angle α between the

base projection and the off-base projection, the error in the off-base projection is not larger than 5%, which we expect to be acceptable for several applications where fast scatter calculation is required.

A more obvious way of re-using the photon histories for all projections would be to directly update the S-maps of all projections using exact photon detection probabilities (DP). Unfortunately, making such a method efficient would require a prohibitive amount of fast (cache) memory (up to 512 Mbyte) for the storage of all S-maps (64 in this study), since all S-maps have to be accessed anew for every scattered photon (more than 10^9 times). These drawbacks would make this alternative method very inefficient compared to the implementation of RMC described in this paper.

The approximations made in RMC are only validated for the use of simulating down-scatter. Therefore, the proposed method cannot be used with confidence for photopeak scatter. For instance, the used central μ approximation appoints an equal attenuation coefficient to all photons on the path from their last scatter position to the detector. In the case of simulating down-scatter it proved to be a good approximation to take the central μ. When simulating photopeak scatter such a choice of one attenuation coefficient for all photons would not be possible, because all scattered photons have an energy lower that the central energy in the energy window. Furthermore, RMC takes advantage of the fact that in every position of the scatter map photons are stored coming from very different directions before they reach their last scatter event. In the case of photopeak scatter the majority of detected photons will come from the same direction before their last scatter position, because they most probably only have scattered once. Therefore the approximations made in RMC regarding the photon's last scatter angle θ will fail in the case of photopeak scatter, especially when only a couple of base-projections are taken, to make the speed-up interesting. In recent publications we described appropriate Monte Carlo techniques for fast calculation of photopeak scatter in non-uniform media and which do not rely on non-general approximations made in RMC [5, 34].

MC simulation using RMC is not exact, but produces down-scatter projections with a maximum error in the projection varying between 0.03 % and about 3% - 5% for the source distribution, simulation grid and number of base projections investigated in here. The errors involved in fast point-spread function based calculation methods, like the Slab Derived Scatter Estimation (SDSE) methods [8, 47], can be estimated using a previous study [30], in which it was shown that the effects of back-scatter, which are not taken into account in SDSE, can double the amount of down-scatter on the detector when 5 cm of back-scatter material is present behind the source. In that study the influence of back-scatter on scatter projections was measured using Tc-99m line sources and an energy window centered at 72 keV. In the point source configuration used in the validation section of this paper, for all point sources positions at least 5 cm of back-scatter material is present. It is shown that in such a high back-scatter situation the proposed method still gives acceptable results (see table 5.1). Furthermore, in contrast to RMC, most other fast analytical calculation methods make coarse approximations regarding wide-angle scatter intensity in non-uniform objects [7]. Wide-angle scatter is relatively important in down-scatter calculation.

The use of variance reduction techniques is wide-spread in Monte Carlo simulators,

although this alters the statistical properties of the simulation data. In case effects concerning photon counting statistics have to be evaluated, a common strategy is to first simulate (almost) noise-free data and then generate the correct (Poisson) noise.

An important source of contamination in Tc-99m/Tl-201 DI SPECT which was not included in the present method is the detection of lead x-rays. Lead x-rays have an energy of about 75 keV and can be produced by Tc-99m photons with an energy larger than 88 keV, when they are absorbed in the collimator lead. The fraction of lead x-rays detected in the region of the Tl-201 x-ray peaks is normally in the range 10%-20% of the total Tc-99m contamination, depending on the choice of collimator [93, 123]. Efficient methods for modeling lead x-rays (possibly in combination with RMC) are mandatory if further improvements are to be made in down-scatter correction in Tc-99m/Tl-201 dual isotope imaging. When these models are evaluated and implemented experimental validation of the proposed methods is possible.

5.5 Conclusions

Rotation-based Monte Carlo simulation combined with convolution-based forced detection may serve as an efficient and accurate tool for down-scatter simulation and model-based down-scatter correction in dual-isotope SPECT, since it takes into account both he effects of back-scatter and the effects of non-uniform mass-density of the object. Next, we plan to incorporate a lead x-ray model in the present method.

Acknowledgements

We are grateful to ADAC Laboratories (Milpitas, CA) for partly financing this research and to Hans van Isselt (University Medical Center Utrecht) for usefull comments.

Chapter 6

Fast Monte Carlo simulation of SPECT down-scatter including interactions with crystal and lead

H.W.A.M. de Jong[1], W.T. Wang[2], E.C. Frey[2], M.A. Viergever[1] and F.J. Beekman[1]
[1]University Medical Center Utrecht, [2]University of North Carolina at Chapel Hill
submitted to Medical Physics

A major image degrading factor in simultaneous Dual Isotope (DI) SPECT or simultaneous Emission-Transmission (ECT-TCT) imaging, is the detection of photons emitted by the higher energy isotope in the energy window used for imaging the lower energy isotope. In Tc-99m/Tl-201 DI SPECT typically tens of percents of the total down-scatter is caused by lead x-rays. In Tc-99m/Gd-153 ECT-TCT, a comparable fraction of the down-scatter originates from Tc-99m photons which only partly deposit their energy in the detector crystal. Down-scatter projections can be estimated using photon transport calculations. which can be used for down-scatter correction.
In this paper we extend a previously proposed efficient down-scatter simulation method, by incorporating into the scatter model the interactions of photons with the detector crystal and collimator lead. To this end, point spread function tables including crystal and lead interactions are simulated. Subsequently, photons are traced through the patient body until their last scatter position, and the precalculated responses are used to project the photons onto the detector plane.The approach is evaluated by comparing calculated Tc-99m down-scatter projections with measured projections. The inclusion of the crystal and lead interactions tremendously increases accuracy of the simulations. Calculating 60 down-scatter projections of an extended distribution on a $64 \times 64 \times 64$ grid takes about 3 minutes on a PC with two 1.2 GHz processors. We conclude that accurate simulation of down-scatter is now possible including all relevant effects of non-uniform density and photon interactions with the crystal and collimator lead.

6.1 Introduction

Simultaneous Dual-Isotope (DI) SPECT allows for studying different biological properties of organs and tissues simultaneously, while only a single scan is performed to obtain SPECT projections. By collecting the photons in separate energy windows, SPECT images can be reconstructed of each of the two radio-nuclide distributions. An advantage of DI SPECT is that problems with the image registration are avoided, which can occur in sequential acquisition of SPECT images. In addition, DI SPECT reduces patient discomfort by reduction of the total of scan time and strong reduction of the time of the total procedure. An example of DI SPECT, is found in myocardial perfusion imaging, where Tc-99m (emission energy 140 keV) and Tl-201 (majority of the emission energies between 69 keV and 80 keV) can be used to simultaneously obtain rest and stress images. However, scattered Tc-99m photons contaminate the Tl-201 photopeak window centered around 72 keV. This contamination causes an overestimation and improper fill-in of defects in the reconstructed Tl-201 distribution (e.g. [53, 72, 124]). In Tc-99m/Gd-153 combined Transmission-Emission CT (TCT-ECT), down-scatter of Tc-99m photons in the Gd-153 transmission window at 100 keV hampers the reconstruction of the transmission map (e.g. [113, 58, 10, 1]). The number of detected down-scattered photons depends on several factors, i.e. the SPECT system used, the energy window settings and the activity ratio of the two isotopes. Furthermore, the amount of down-scatter is patient dependent due to differences in organ uptake, patient size and attenuation distribution. Because of the strong influence of the down-scatter on the quantitative accuracy of the Tl-201 image and the transmission maps, neither DI SPECT nor TCT-ECT are suitable without correction for this down-scatter (e.g. [72, 1, 26]).

Down-scattered photons can be divided in two classes. First, photons originating from the Tc-99m source can be detected in the Gd-153 and Tl-201 photo-peak windows due to energy loss in scatter interactions in the patient which we refer to as *object down-scatter*. Secondly, both unscattered photons and photons which scattered in the patient can interact with collimator lead (e.g. causing lead x-rays) or only partially deposit their energy in the crystal, which will be referred to as *camera down-scatter*.

Several methods have been proposed to correct for the down-scatter contamination in Tc-99m/Tl-201 DI SPECT. Most methods use an intermediate scatter window from which the down-scatter estimation is calculated by scaling and/or applying a filter. This down-scatter estimate is then subtracted from the Tl-201 data in the object or projection image domain. These approaches are relatively easy to implement and require little computation time. A disadvantage is that the subtracted down-scatter estimate is noisy, which further increases the noise level in the corrected image. Furthermore, the spatial distribution of the down-scattered photons is difficult to describe with spatial information acquired in other energy windows [53]. As an example, markedly different spatial distributions of scattered Tc-99m counts in the scatter window (e.g. 100 keV $\pm$ 10%) have been found, as compared with the lower-energy window (e.g. 72 keV $\pm$ 10%). This causes inaccuracies and artifacts in the corrected images [26]. This problem could partially be accounted for by spatially convolution of the scatter window, or deconvolution of the lower-energy isotope image [74]. Moore et al. used the convolution strategy and also included the 140 keV photopeak window in the down-scatter correction to take lead x-rays into account [92].

The main drawback of these methods is that they use a spatial invariant (de-)convolution kernel, or a single factor to appropriately scale scatter windows, which partly ignores the source-depth dependency of the down-scatter.

An approach that does not require patient dependent parameters, scaling factors and additional scatter windows and which has the conceptual advantage of minimizing noise amplification is to calculate the down-scatter projections during image reconstruction. This model-based correction requires a reconstructed activity distribution of the higher energy isotope, an attenuation map and a method based on photon transport models to calculate the down-scatter projections (e.g. [68, 12]). Monte Carlo (MC) simulation is often regarded as the most accurate method to calculate SPECT projections; however the construction of a low-noise estimate is computationally demanding. Therefore several techniques have been introduced to speed up MC simulation.

We recently proposed to calculate object down-scatter projections using a combination of two acceleration techniques: Rotation-based Monte Carlo (RMC) [29] and Convolution-based Forced Detection (CFD) [5, 34]. These methods enable to simulate object down-scatter several orders of magnitude faster than standard MC. However, to date, photon interactions in crystal and lead were not included. In the mean while, the UNC group introduced a method to simulate lead x-ray projections for DI SPECT [123] by combining a layer-by-layer blurring model with an existing down-scatter model (Effective Scatter Source Estimation, ESSE [49]). In this approach only the lead x-ray kernels were pre-calculated using Monte Carlo simulations. The purpose of the present paper is to provide a more general and accurate framework for efficient calculation of down-scatter projections which can be used to improve both DI SPECT and ECT-TCT. To this end, we combine RMC for calculating object down-scatter with pre-calculated lead x-ray kernels. An advantage of RMC over ESSE and other approximate models is that RMC is based on first physical principles which is more general and accurate for including effects caused by non-uniformities and backscattered photons on down-scatter calculations. Furthermore, in contrast with previous down-scatter calculation methods, not only object and lead x-ray interactions are accounted for, but also interactions with the crystal.

6.2 Gamma interaction with lead and NaI crystal

In this section, lead x-rays, collimator scatter and partial energy deposition in the detector crystal, which are the effects that contribute to the Tc-99m camera down-scatter in the $100\pm10\%$ keV or $72\pm10\%$, are looked at more closely.

Lead x-rays. The majority of the Tc-99m photons which enter the camera are photo-electrically absorbed in the collimator lead. When photons are absorbed with an energy higher than 88 keV, lead x-rays are emitted. Because these lead x-rays have an energy of around 80 keV, they can be detected in the 72 keV energy window.

Compton scatter. A small part of Tc-99m photons which interact with the collimator have Compton scatter events in the lead [18]. These photons loose energy in the scatter process, so that they can be detected in the 100 keV or 72 keV window.

Table 6.1: Relative contribution of object down-scatter, and the different parts of the camera down-scatter in 100±10%keV and 72±10% keV energy windows, expressed as a percentage of total counts in the 140 keV window. The numbers are calculated using MCNP for a Tc-99m point source in air, and a point source positioned in the center of a 22.2 cm diameter water-filled cylinder.

	Point-source in Air		Point-source in Cylinder	
	100 keV	72 keV	100 keV	72 keV
object down-scatter scatter	0%	0%	51%	44%
partial energy deposition	2.4%	0.4%	6%	0.3%
collimator scatter	0.05%	0.01%	0.9%	1.5%
lead x-rays	0.4%	3.7%	0.2%	7.4%

Partial energy deposition. Tc-99m photons also can contribute to the camera down-scatter when only a part of the photon energy is absorbed in the detector crystal. For example, Tc-99m photons which have Compton scatter in the NaI crystal can escape the crystal after scattering ([18]). In such cases, only a part of the photon energy is deposited during scatter. Partial energy deposition also occurs when x-rays, which are emitted after photon absorption, escape the crystal.

Both primary (unscattered) and scattered Tc-99m photons can contribute to the camera down-scatter in the above described manners. Therefore, also Tc-99m photons that scattered in the object or patient (i.e. object down-scatter) have to be included in calculation of the camera down-scatter.

Table 6.1 shows the relative contributions of the camera down-scatter contributions in the 100 keV and 72 keV energy window. These numbers were calculated for a Tc-99m point-source in air and in a water-filled cylinder using a modified version [123] of the Monte Carlo N-Particle code MCNP4B [23], which is capable of keeping track of all gamma interactions with crystal and lead. These results show that the camera down-scatter in the 100 keV energy window is largely due to partial energy deposition in the crystal. In the 72 keV energy window the major part of the camera down-scatter is due to lead x-rays. Therefore, in calculating the camera down-scatter in this window, only photons entering the camera with an energy larger than 88 keV will be included. In the next section the implementation of the camera down-scatter is described more in detail.

6.3 Methods

The camera down-scatter projections are calculated in two steps, which are described in this section. First the photon scatter in the object is simulated using the rotation-based Monte Carlo (RMC) method. With this intermediate result, the primary and scattered photons are projected on the detector plane using tabulated point spread functions including the gamma interactions described in section 2. At the end of this section phantom

measurements are described, which are used to validate the proposed down-scatter model.

6.3.1 Camera Down-Scatter calculation

Rotation-based Monte Carlo

The RMC method has previously been proposed to efficiently generate object down-scatter projections including effects due to non-uniform mass densities and backscattered photons [29]. RMC works as follows: For every projection angle, a 3D voxelized map (scatter map) is generated which contains at every (voxel) position the sum of probabilities of photons scattering from that position to the detector. Next the scatter map is blurred layer-by-layer with a distance dependent geometric response function modeling collimator and detector blurring. The blurred layers are summed to form the object down-scatter projection.

For the required photon transport calculations we used a simulator developed by us: the Utrecht Monte Carlo System (UMCS) [33]. The UMCS is designed for fast photon transport simulation in SPECT. The code is written in C++. The simulations include Compton scatter and photo-electric absorption. We have previously validated UMCS using measurements of point-sources behind slabs, and projections and energy spectra of extended source distribution generated with the SIMIND Monte Carlo code [83]. These validations showed excellent agreement between the UMCS and SIMIND generated projections and experimentally acquired projections in the Tc-99m photopeak window [33, 32].

Point Spread Functions

Incorporation of camera down-scatter in RMC is based on point spread functions (PSF) of point-sources in air which include the effects of partial energy deposition, collimator scatter, and lead x-rays. Measured in energy window W (i.e. 100±10% keV or 72±10% keV), the $PSF_W(\vec{x}, z)$ depends on the collimator and detector characteristics, the distance z between the point source and detector and the position $\vec{x}$ on the camera measured from the center of the PSF (Fig. 6.1). Furthermore, the shape and magnitude of the $PSF_W(\vec{x}, z)$ changes slightly with emission energy E, so that it would be necessary to know the $PSF_W(\vec{x}, z)$ for every possible energy. In order to make the method efficient, for the 100 keV window a distinction was only made between camera down-scatter due primary Tc-99m photons ($PSF^{pr}_{100}(\vec{x}, z)$) and photons scattered in the object ($PSF^{sc}_{100}(\vec{x}, z)$). For the 72 keV window a comparable approach is used, however, the scattered photons were split up in two energy groups (88-107 keV and 107-140 keV) because of the broader energy range of photons which can generate lead x-rays. These latter point spread functions represent the projection of a point-source emitting photons with an energy uniformly distributed over the given energy range. For calculation of camera down-scatter in the 72 keV window $PSF^{pr}_{72}(\vec{x}, z)$, $PSF^{107-140}_{72}(\vec{x}, z)$ and $PSF^{88-107}_{72}(\vec{x}, z)$ are needed. The use of these PSF is similar as described by Wang et al. [123].

All $PSF_W(\vec{x}, z)$ were measured at distances of 1, 5, 10, 15, 20, 25, 30 and 40 cm. $PSF_W(\vec{x}, z)$ at other distances z are estimated from these. Wang et al. used analytic

expressions to fit the $PSF_W(\vec{x}, z)$ for the different distances simultaneously, which involves simultaneous fitting of 8 parameters using a complex fitting procedure [123]. Furthermore, only PSF measured in the Tl-201 photopeak window were fitted in that study, so that the used expressions could not directly be used for PSF measured in the 100 keV window. In order to increase generality and robustness, second-order Lagrange interpolation is used for estimating the intermediate PSF's in the present study, similar to [14].

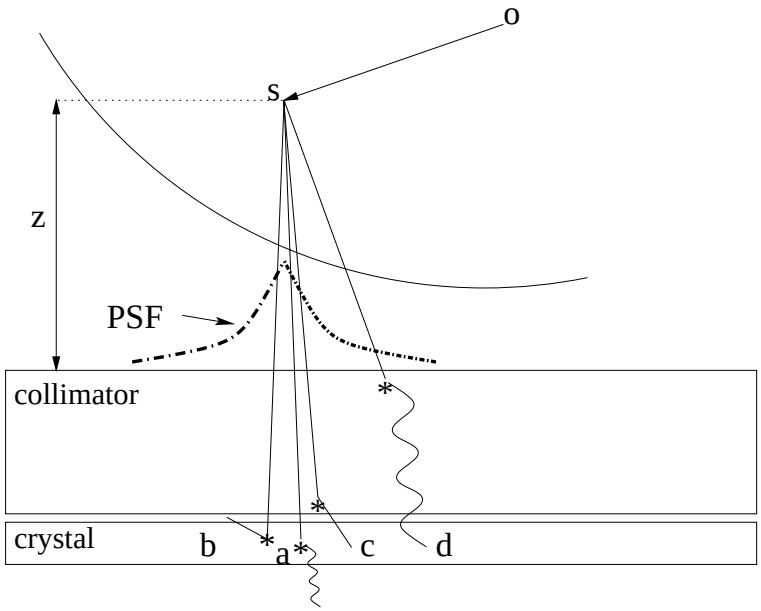

Figure 6.1: A photon scattering at position S can be detected after direct absorption in the crystal or (a) with possible escape of the resulting x-ray (partial energy deposition), (b) after scattering in the crystal with possible escape after scatter (partial energy deposition), (c)after scatter in the collimator, or (d) via emission of a lead x-ray. Instead of forcing a photon coming from S to be detected in one of these manners, a PSF is projected which includes all these photon events in the camera. This PSF depends on the scatter position distance z and the energy E of the photon directly after scattering in S.

Together with $PSF_W(\vec{x}, z)$ the camera down-scatter can be calculated when at each position in the object the distribution of primary and scattered photons is known which leave that position in the direction of the camera (Fig. 6.1). This distribution is calculated using RMC.

Generating the down-scatter projections

For calculation of a camera down-scatter projection due to photons which scattered in the object, RMC is used to generate scatter maps as explained in 6.3.1. For the 100 keV

window a scatter map was generated including all scattered photons with an energy too high to be directly detected in that window. This scatter map is blurred layer-by-layer with the $PSF^{sc}_{100}(\vec{x}, z)$. The Tc-99m source map, which contains the original emission distribution, is blurred layer-by-layer with the $PSF^{pr}_{100}(\vec{x}, z)$. After blurring all layers are added to form the camera down-scatter in the 100 keV window. For the 72 keV window two scatter maps were generated; One includes all scattered photons leaving the object in the energy-range 107 - 140 keV while the other includes all scattered photons leaving the object in the energy-range 88 - 107 keV. The first scatter map is blurred layer-by-layer with the $PSF^{107-140}_{100}(\vec{x}, z)$, the second with $PSF^{sc}_{72}(\vec{x}, z)$. Furthermore, the source map is blurred layer-by-layer with the $PSF^{pr}_{72}(\vec{x}, z)$. Again, the blurred layers of the two scatter maps and the emission map are added to form the camera down-scatter in the 72 keV window.

6.3.2 Physical Experiments

All experiments were carried out on an ADAC Vertex^{TM} camera (ADAC Laboratories, Alder Drive 540, Milpitas CA) equipped with Vantage Extra High Resolution (VXHR) collimators (hole length 54 mm and an inner hexagonal hole diameter 2.03 mm, septum thickness 0.152 mm). The thickness of the NaI crystal in the detector was 9.5 mm.

Measurement of the camera energy resolution

In order to accurately model the energy resolution of the camera in the simulations, energy spectra were measured of point-sources in air containing Tc-99m (140keV), Co-59 (122 keV), and Am-243 (60 keV) (Fig. 6.2). The energy resolution (expressed in Full Width at Half Maximum) was modeled linearly proportional to the energy E, $FWHM = 0.068E + 3.95$ [keV], similar to [123].

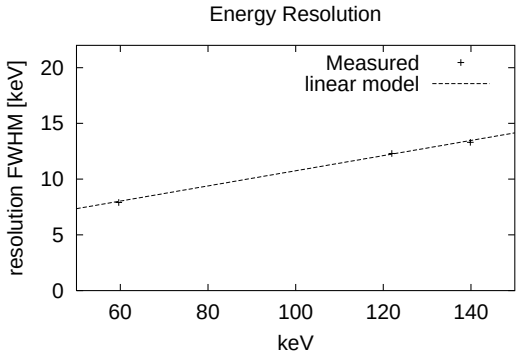

Figure 6.2: Energy resolution in FWHM [keV] as a function of energy, used to calibrate the Monte Carlo simulations. The crosses in the plot indicate resolutions measured at 140 keV (Tc-99m), 122 keV (Co-59), 60 keV (Am-241).

Validation of MCNP

Validation of the modified version of MCNP was achieved by acquiring projections of Tc-99m in a small cylindrical perspex source holder (diameter 3 mm, height 7 mm) measured in the 140 keV ± 10%, 100 keV ± 10% and the 72 keV ± 10% energy windows. To reduce down-scatter from the gantry and the walls 1.5 cm of copper was placed behind the source. The influence of the copper and the source holder were also included in the MCNP simulations. In this set-up, about 23% of all photons detected in the 100 keV are due to gamma interactions with lead or crystal while this percentage is 87% in the 72 keV energy window. Excellent agreement between the profiles of the experimental and simulated projections demonstrates the accuracy of the MCNP code (Fig. 6.4).

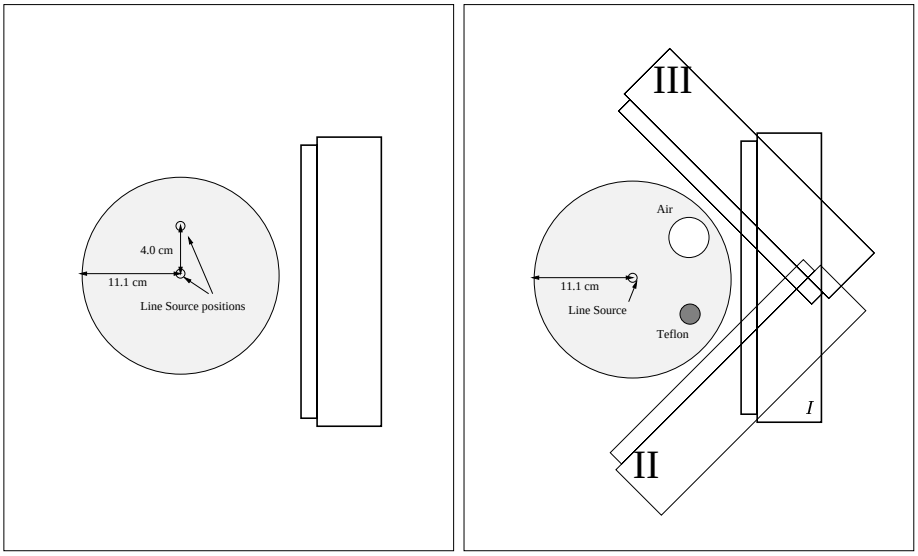

Figure 6.3: Experimental set-up and camera positions used to validate the proposed model. The cylinder was entirely filled with water (left frame) or contained a Teflon rod and an air filled rod as shown in the right frame.

Down-scatter projection measurements

The proposed down-scatter method was validated by measurements with a short cylindrical Tc-99m source (length 10 mm, diameter 3 mm, 50 MBq) in a water filled cylinder with a diameter of 22.2 cm and a length of 21 cm. The energy windows were 140 keV ± 10%, 100 keV ± 10% and 72 keV ± 10%. The source was located at the center and an off-center position. A non-uniform cylindrical phantom was produced using two cylindrical rods (a Teflon cylinder with a diameter of 26 mm and an air-filled perspex cylinder with a diameter of 56 mm) placed in the water cylinder. For this phantom we used 3 camera positions and a source at the center of the cylinder as shown in Fig. 6.2.

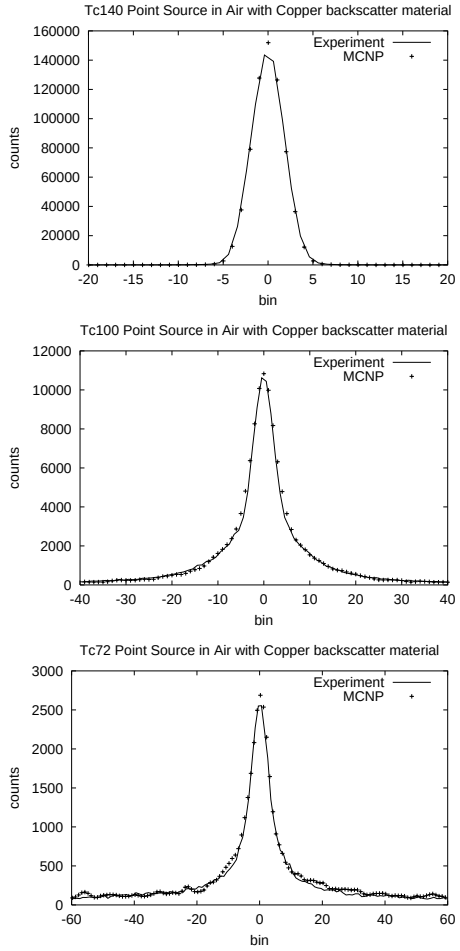

Figure 6.4: Profiles of MCNP simulated and experimental projections for a point source in air for the 140 keV window (top), 100 keV window (center) and the 72 keV window (bottom).

6.4 Results

RMC was used the generate object and camera down-scatter projections of a small line source in a cylindrical phantom. Figures 6.5 and 6.6 show profiles (profile width 0.972 cm) of the simulated and measured projections of the uniform cylinder phantom in three different energy windows: 140 keV photopeak window, and the 100 keV and 72 keV down-scatter windows.

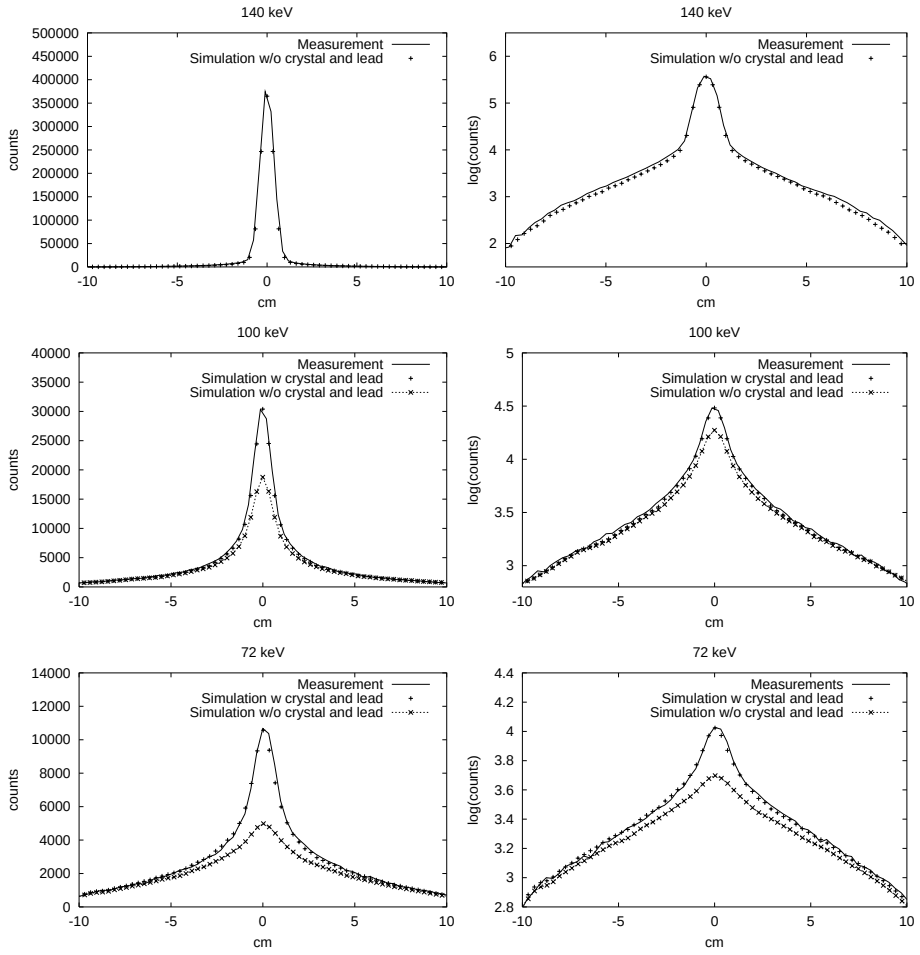

Figure 6.5: The profiles of the projection image in the 140 keV, 100 keV and 72 keV windows acquired from the Tc-99m line source located at the center position of the uniform cylinder phantom. Profiles of the simulated projections are shown with and without inclusion of the camera down-scatter model to show the influence of collimator scatter, lead x-rays and partial absorption. Profiles are shown on a linear (left) and a semi-logarithmic scale (right).

6.4.1 Accuracy

The pixel size in the projections is 0.324 cm. The simulated down-scatter projections are shown with and without inclusion of gamma interactions in the crystal and the collimator. Simulated and measured projections were scaled to the count level in the 140 keV photopeak projection and the same scale factor was used for all projections. There is a

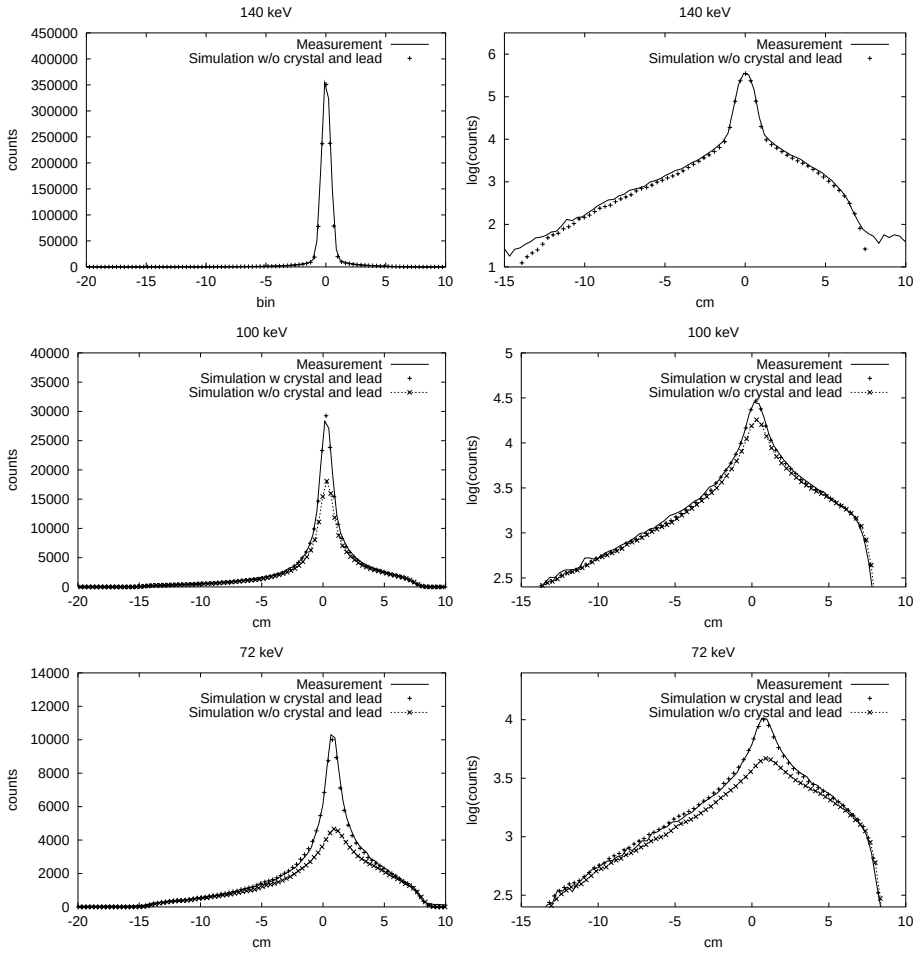

Figure 6.6: Same as Fig 6.5, but now with the line source in the off center position.

tremendous increase in accuracy due to the inclusion of the camera down-scatter. Good agreement between simulated and experimentally acquired projections is also achieved for the case when the line source was positioned in an off-center position. This is promising because modeling the asymmetric scatter response of a source close to the edge of the attenuator is often regarded as difficult to achieve (mainly due to the large influence of back-scattered photons on the down-scatter projection [30]). Figures 6.7, 6.8 and 6.9 show profiles of the simulated and measured projections of the non-uniform cylinder phantom for three different views. Good agreement is also achieved in these cases. The small deviations between simulated and experimentally acquired projections could be explained by small deviations between experiments and simulations in the positioning of the air tube and Teflon tube.

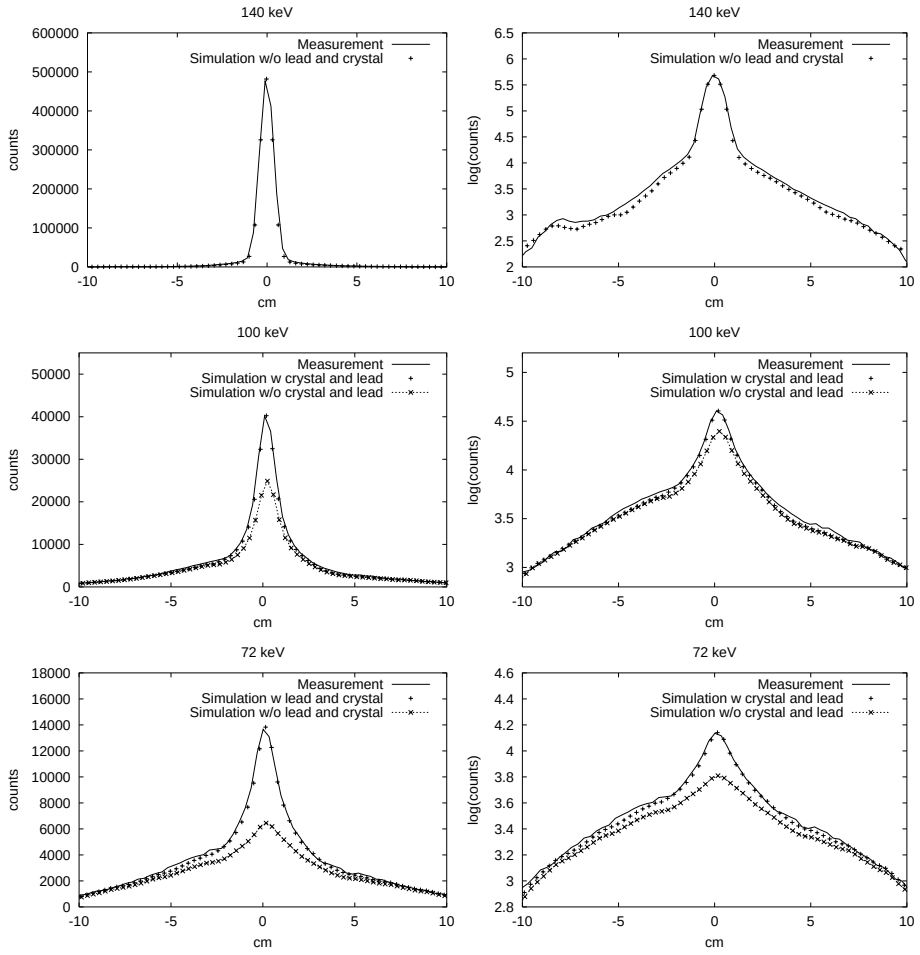

Figure 6.7: Same as Fig 6.5, but now with the non-uniform cylinder phantom, and camera position I.

6.4.2 Efficiency

Computational efficiency of the method was determined using the Mathematical Cardiac Thorax (MCAT) phantom [116]. The size of the cubic voxels and the dimensions of the phantom were 0.5 cm and $64 \times 64 \times 64$, while the size of the square pixels and projection dimensions were 0.5 cm and 64×64. In Fig. 6.10 a slice of the Tc-99m activity distribution and mass density distribution is shown. In Fig. 6.11 profiles (profile width 0.5 cm) of simulated Tc-99m projections in the 100 keV and 72 keV window with and without inclusion of camera down-scatter are compared. These simulations are based on 10^7 photons. For comparison profiles of a high count simulation (10^9 photons) are

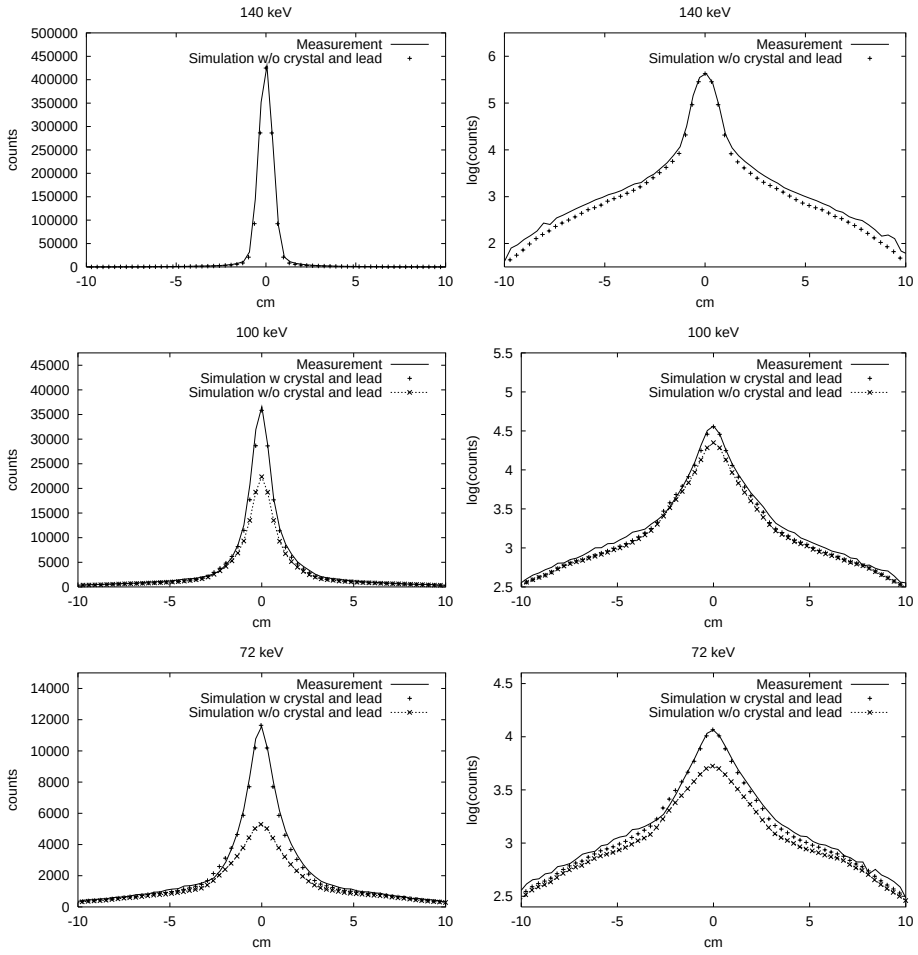

Figure 6.8: Same as Fig 6.5, but now with the non-uniform cylinder phantom, and camera position II.

also shown. Calculating the 60 down-scatter projections (10^7 photons) on a Pentium III computer with two 1.2 GHz processors takes 243 seconds without inclusion of camera down-scatter and 339 seconds with inclusion of camera down-scatter. The simulation described in here requires 40 Mbyte of computer memory.

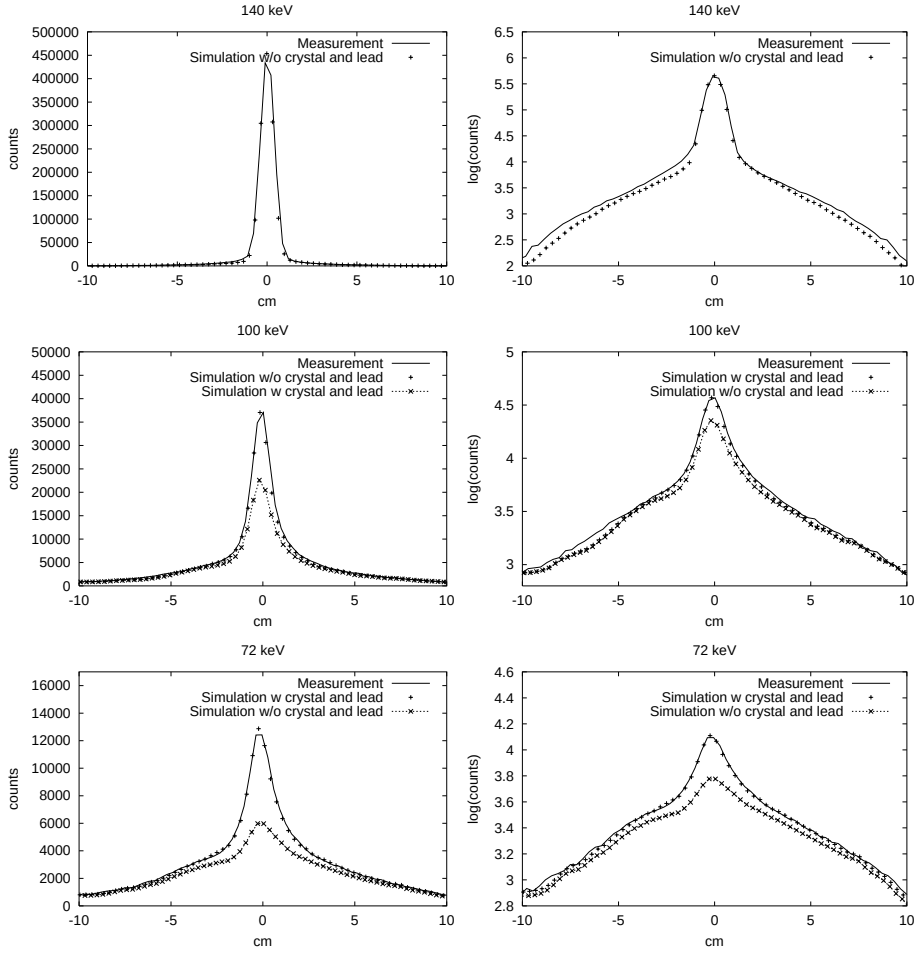

Figure 6.9: Same as Fig 6.5, but now with the non-uniform cylinder phantom, and camera position III.

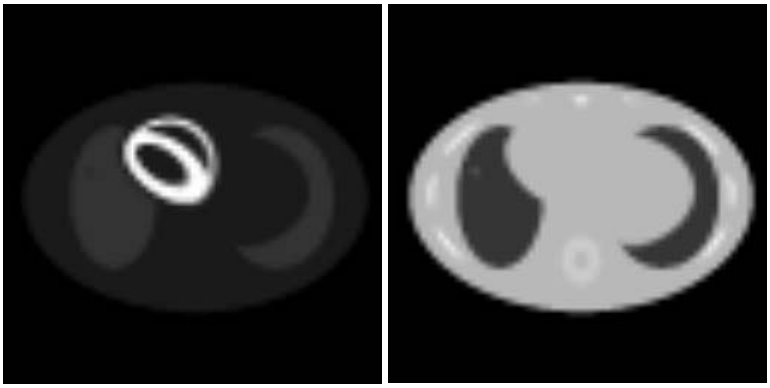

Figure 6.10: Cross section of the MCAT phantom at mid-ventricular level. Left: extended activity distribution in the heart, lungs and background. Right: mass density distribution.

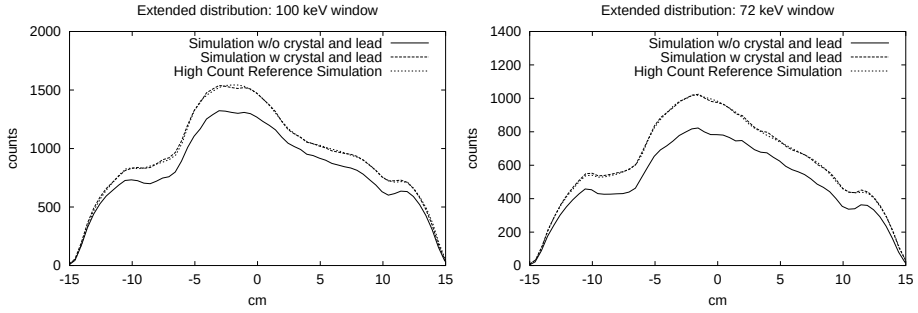

Figure 6.11: Simulated Tc-99m anterior down-scatter projections of the MCAT phantom with and without inclusion of camera down-scatter compared to a high count reference simulation. Top: Simulated anterior projection in the 100 $\pm$ 10 %keV energy window. Bottom: Simulated projection in the 72 $\pm$ 10 %keV energy window.

6.5 Discussion and conclusion

In order to accurately simulate the down-scatter of Tc-99m photons in the Gd-153 transmission window and in the Tl-201 photopeak projection, the effect of partial energy deposition in the crystal, of collimator scatter and of lead x-rays were included within an accelerated Monte Carlo (MC) frame-work. This study shows that for accurate modeling of down-scatter all these effects are important; a tremendous increase in accuracy of simulated projections was accomplished when these effects were included.

In order to make the simulation method efficient, some approximation were made. First of all, photons are forced to move to the camera in the direction of the collimator hole axis after leaving their last scatter position. However, especially photons which generate detected lead x-rays may have traveled a path in a direction that is non-perpendicular the collimator face. Furthermore, an approximation was made regarding the energy de-

pendency of the point spread functions. For example in the case of camera down-scatter in 100±10% keV, a distinction was only made between primary (140 keV) and scattered photons (<140 keV). The validation of the method shows that despite the assumptions made, the simulated projections are in good agreement with the experimental measured projections, even in more complex situations, like non-uniform mass densities in the phantom or with sources near the boundary of the object.

The use of MC techniques might be computationally more demanding than that of most other proposed down-scatter correction methods. However, it is expected that the acceleration techniques used in this paper will make MC simulation feasible very soon to apply for down-scatter correction within clinically acceptable times.

In conclusion, the proposed combination of Monte Carlo simulation with efficient modeling of gamma interactions with lead and crystal may serve as an efficient and accurate tool for down-scatter simulation. Incorporation of this simulation-method into an iterative reconstruction algorithm may allow for accurate down-scatter correction in simultaneous Emission-Transmission CT, and in Dual-Isotope SPECT.

Chapter 7

Simultaneous Tc-99m/Tl-201 dual-isotope SPECT with Monte Carlo-based down-scatter correction

H.W.A.M. de Jong, F.J. Beekman, M.A. Viergever and P.P. van Rijk
University Medical Center Utrecht
submitted

In simultaneous Tc-99m/Tl-201 dual-isotope (DI) SPECT, down-scatter of Tc-99m photons contaminates the Tl-201 image, which leads to decrease of lesion contrast and loss of quantitative accuracy. Correction for down-scatter can be achieved by first reconstructing the Tc-99m activity distribution. Subsequently, the Tc-99m down-scatter in the Tl-201 photopeak window is simulated and used for correction during iterative reconstruction of the Tl-201 image. In this work, the down-scatter projections are calculated using a dedicated Monte Carlo simulator which is able to efficiently model the detection of lead x-rays from the collimator. An antropomorphic torso phantom with cardiac insert with and without cold lesions, was used for evaluation of the proposed method. Excellent agreement in lesion contrast and quantitative accuracy was found between the down-scatter corrected DI-SPECT Tl-201 image and the virgin (i.e. separately acquired) Tl-201 image, in particularly when the effects of lead x-rays were included. Compensation for the noise added by down-scatter to the Tl-201 image is possible by using a 15% lower dose of Tc-99m, a 15% increase in scan time and a 12% increase in Tl-201 dose.
In conclusion, the Monte Carlo-based down-scatter correction recovers lesion contrast and quantitative accuracy in DI-SPECT Tl-201 images, while degradations due to the added noise of down-scatter in simultaneous DI-SPECT can be compensated for by slight adaptations to the data acquisition protocol.

7.1 Introduction

The aim of cardiac SPECT imaging is to acquired information about regional or global myocardial perfusion, tissue viability and functional characteristics as left ventricle ejection fraction and wall movement. Diagnostic viability information is obtained by studying myocardial perfusion under stress and rest conditions. Most protocols involve the use of Tl-201 and/or Tc-99m labeled compounds of which different imaging qualities have been reported [119]. For instance, separate stress Tc-99m/rest Tl-201 imaging is well-established in routine clinical cardiac imaging. A relatively new and promising cardiac SPECT protocol is simultaneous stress Tc-99m/rest Tl-201 dual-isotope SPECT (DI-SPECT), which allows for simultaneous evaluation of the processes targeted by the two radio-isotopes [19, 108]. DI-SPECT has some interesting potential benefits over separate dual-isotope protocols. It decreases overall study time and scan time, which allows for increased patient throughput, cost reduction and reduced patient discomfort. Furthermore, perfect registration between rest and stress images is guaranteed.

Simultaneous dual-isotope SPECT images are degraded by down-scattered photons of one radio-isotope that contaminate the image of the other radio-isotope. In DI-SPECT, Tc-99m photons emitted at 140 keV can be detected in the Tl-201 photopeak, centered around 72 keV, owing to energy loss in Compton scatter interactions or via the emission of lead x-rays from the collimator [93]. This down-scatter can lead to gross overestimation in activity and loss of contrast in small lesions [72, 124, 53, 26]. For example, a irreversible defect (indicating non-viable tissue) in separate Tc-99m/Tl-201 SPECT can be interpreted as a reversible defect (indicating viable tissue) in DI-SPECT, which may lead to needless angioplasty or bypass surgery, if down-scatter is not corrected for. In addition, down-scatter adds noise to the Tl-201 image. In general, Tc-99m/Tl-201 DI-SPECT is often regarded as unsuitable for clinical use without adequate correction for the effects of down-scatter [40, 19, 72, 26]. Several methods have been proposed to correct for down-scatter [73, 92, 74, 54]. The majority of these correction methods is based on estimating the down-scatter by blurring and scaling projection data acquired from intermediate scatter windows. Although these methods are computationally efficient, they can not accurately take into account the patient dependency of the down-scatter. Furthermore, a down-scatter estimate directly based on measured projections is often noisy, which will add noise to the down-scatter corrected Tl-201 image.

An approach that does not require patient-dependent parameters, scaling factors and additional scatter windows is to calculate the down-scatter projections using point-spread functions during image reconstruction. These model-based corrections employ the reconstructed Tc-99m activity distribution and a transmission CT ('attenuation map') registered to the SPECT image to calculate the down-scatter projections (e.g. [12, 68]). Monte Carlo (MC) simulation is often regarded as the most accurate method to calculate SPECT projections; however the estimation of noise-free projections is computationally demanding. Several techniques have been introduced to speed up SPECT MC simulation [57, 101, 5, 34, 29].

We recently proposed to calculate down-scatter projections using a combination of two acceleration techniques: Rotation-based Monte Carlo (RMC) [29] and Convolution-based Forced Detection (CFD) [5, 34, 36]. RMC is capable of giving very accurate es-

timates of the measured down-scatter, in objects with uniform and non-uniform density distributions, and can model the effects of lead x-rays.

The goal of this study is to develop accurate correction for down-scatter in order to recover the quality of the Tl-201 image in simultaneous Tc-99m / Tl-201 dual-isotope SPECT protocols. To achieve this, a Monte Carlo-based approach is evaluated. Furthermore, the influence of modeling lead x-rays in the Monte Carlo simulator is investigated, and an adaption to the acquisition protocol is proposed to reach the lower noise level of a separately acquired Tl-201 image ('virgin' Tl-201 image).

7.2 Materials and Methods

In DI-SPECT, the Tc-99m image is hardly hampered by the Tl-201 activity in the myocardium; Using a typical acquisition protocol, only 2 - 4 % of the Tl-201 photons will be detected in the 140 keV window [68]. Therefore, the Tc-99m image can be reconstructed using the same approach as used in separately acquired Tc-99m SPECT. Based on the acquired transmission CT map and the reconstructed Tc-99m distribution, the Tc-99m down-scatter projections in the Tl-201 energy window are simulated using accelerated Monte Carlo simulations (section 7.2.3). Finally, the Tl-201 image is reconstructed while accounting for down-scatter during statistical reconstruction (section 7.2.3). The proposed method was validated by means of thorax phantom experiments.

7.2.1 Antropomorphic Thorax Phantom Experiments

A physical antropomorphic thorax phantom (Model ECT/Lung/P, Data Spectrum Corp., Hillsborough, NC, Fig. 7.1) was used for validation of MC-based down-scatter correction . It consists of a cardiac insert representing the myocardium, two lung inserts, a liver insert and a spine insert. A small solid defect (2 ml) was placed in the anterior wall and a large solid defect (5 ml) in the inferior wall of the heart insert. Furthermore, to assess the uniformity of the reconstructed myocardial wall, a phantom set-up was used without lesions in the heart insert.

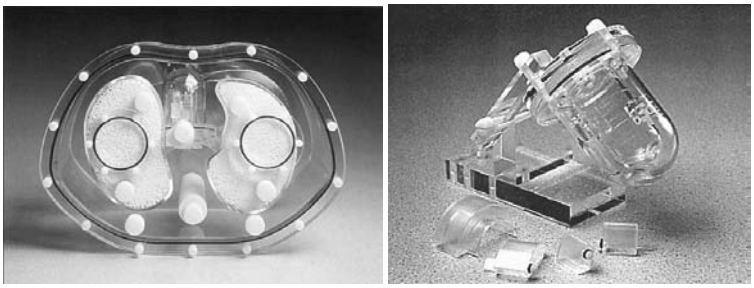

Figure 7.1: Left: Antropomorphic thorax phantom. Right: Cardiac insert with lesions. Images by courtesy of Data Spectrum Corp.

Two high count SPECT data sets were acquired: one with only Tc-99m in the phantom and one with only Tl-201 in the phantom. Peak count levels in the projections were over 10,000 counts/pixel for the Tc-99m projections and over 15,000 counts/pixel for the Tl-201 projections. This is more than a hundred times higher as found in typical clinical studies, so these projections can be regarded as containing a negligible amount of noise. The almost noise-free projection data can be scaled after which Poisson noise can be added to produce any required count level. This enables studying different acquisition times, activity levels and Tc-99m/Tl-201 ratio's. In both measurements the phantom was placed at exactly the same position (deviation smaller than 1 mm) on the scanner table.

The relative activity concentration ratio myocard:liver:lungs:background was 30:15:3:1 for Tc-99m and 100:5:4:5 for Tl-201. These ratio's reflect the distributions of separately acquired stress Tc-99m and rest Tl-201 studies [119]. The Tc-99m data were measured in the Tc-99m photopeak window (140 keV $\pm$ 10%) and in the lower Tl-201 photopeak window (72 keV $\pm$ 10%). The Tl-201 data were acquired in the lower and higher Tl-201 photopeak windows (72 keV $\pm$ 10% and 167 keV $\pm$ 7.5%) and in the Tc-99m photopeak window.

DI-SPECT studies were obtained by summing the separately acquired Tc-99m and Tl-201 projections in concordant energy windows. Projections were scaled and Poisson noise was added to emulate projections from a typical DI SPECT study with an acquisition time of 35 seconds per projection, 4 mCi Tl-201 and 25 mCi Tc-99m administered to the patient [19]. Absolute activities in the myocardium were based on 1.1% myocardial uptake for Tc-99m and 3% for Tl-201 [86].

All experiments were carried out on a dual-head ADAC Vertex camera equipped with Vantage Extra High Resolution (VXHR) collimators. The SPECT studies were acquired over a non-circular, 180° orbit using 64 projections and 128 $\times$ 128 matrices, with a pixel size of 4.72 mm. A transmission map was acquired using two scanning Gd-153 line sources (150 mCi each), with a electronic moving window and 34 seconds per projection (ADAC Vantage^{TM}).

7.2.2 Reconstruction algorithms

Both the emission and transmission images were reconstructed on a dual-processor 1.2 GHz Pentium PC, using iterative statistical algorithms. The reconstruction voxel size was $4.72 \times 4.72 \times 4.72$ mm and the matrix size was $128 \times 128 \times 128$.

Transmission map

The transmission image was reconstructed with the ordered subsets convex algorithm [69]. The number of iterations performed was six with subsets containing eight projections each. An elliptical uniform start image was used. Images were post-processed with a cubic shaped median filter ($3 \times 3 \times 3$ voxels). A sample slice of the filtered transmission image is shown in Fig. 7.2.

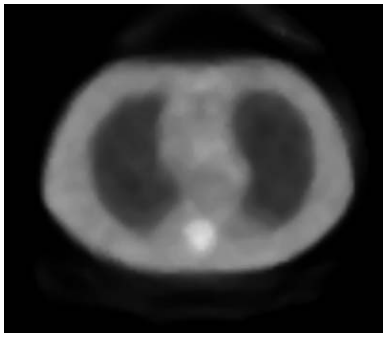

Figure 7.2: Slice of the reconstructed CT map of the antropomorphic phantom.

Tc-99m reconstruction

The Tc-99m emission distribution was reconstructed using a fully 3D Dual Matrix Ordered Subsets Expectation Maximization algorithm (DM-OS) with eight subsets [70]. The effects of attenuation, fully 3D object shape dependent photopeak scatter and distance-dependent detector response were included the projector [13]. Effects of non-uniform mass-densities were incorporated using water equivalent depths according to the implementation in [7]. In order to assure a high and almost constant resolution over the whole image, a relatively high number of iterations (30) was performed, instead of stopping the iteration process early [91, 16].

7.2.3 Monte Carlo-based down-scatter correction

The rotation-based Monte Carlo (RMC) method combined with the modeling of lead x-ray detection was recently proposed to efficiently generate down-scatter projections including effects due to non-uniform mass densities and multiple order scattered photons [29, 35]. With RMC, down-scatter projections were calculated based on the reconstructed Tc-99m distribution and the transmission map. In order to maintain accurate contrast in the down-scatter estimates, unfiltered Tc-99m reconstructions were used for the calculations. This did not lead to significantly increased noise in the down-scatter simulations, since the simulated projection pixel values can be regarded as weighted sums of voxel activity estimates. Down-scatter projections were based on on $5 \cdot 10^7$ photon paths calculated including 10 orders of Compton scatter and the effects due to the detection of lead x-rays ('DI Fully Corrected'). This takes about 12 minutes on a PC with Dual 1.2 GHz processors. To investigate the importance of lead x-ray simulation, projections were also calculated neglecting the effects of lead x-rays ('DI Corrected w/o Pb x-rays').

Tl-201 reconstruction

For reconstruction of the Tl-201 images, the projections acquired in the 72 keV window and in the 167 keV window were added. Although the 167 keV window contains less than

10% of the total number of detected Tl-201 photons, these higher energy photons are less hampered by attenuation or scatter and therefore add relatively much information content per emitted photon to the Tl-201 image. Similarly to the Tc-99m images, Tl-201 images were reconstructed with correction for attenuation, Tl-201 photopeak scatter, and detector blurring. For reconstruction of the down-scatter corrected DI-SPECT Tl-201 images, the Monte Carlo simulated down-scatter projections were added to the denominator of the DM-OS algorithm [22, 9] Thirty iterations OS-EM 8 were used to reconstruct Tl-201 images. For visualization, Tl-201 images were post-filtered using a 3D Gaussian blurring filter with a Full Width at Half Maximum of 1.65 cm.

7.2.4 Assessment of Image Quality

Image quality of the down-scatter corrected and uncorrected DI-SPECT Tl-201 images was compared to virgin Tl-201 images, in terms of lesion contrast, noise in the myocardium, and quantitative accuracy. The lesion contrast is defined as $|m - l|/(m + l)$, where m is the average activity in the myocardial wall and l is the average activity in a region covering the lesion.

In order to assess image noise in the myocardial wall, reconstructions of projections with two different noise realizations were performed for every specific SPECT study. The reconstructions with the two different noise realizations were subtracted. The Normalized Standard Deviation (NSD) was determined in a region drawn over the myocardial wall in the subtracted image, by averaging the variance over all voxels and dividing it by the mean count level in the noise realizations. This approach prevents influence of bias on the NSD.

Bulls-eye plots were constructed from short-axis images by sampling the maximum counts in the myocardial wall. In order to ensure that the sampling was largely perpendicular to the myocardial wall, the basal part of the myocardium was sampled cylindrically, while the apical part was sampled spherically [51, 41]. In the short-axis images of the Tl-201 reconstructions, five regions were drawn in which the average count level was calculated: apex, anterior wall, lateral wall, inferior wall and septal wall. These regional count levels are compared to the average count level in the whole myocardium in the same study.

7.3 Results

In Figs. 7.3 and 7.4, reconstructed short-axis images are shown of the DI-SPECT and virgin Tl-201 images. Fig. 7.3 shows the short-axis image at the level of the large lesion, Fig. 7.4 at the level of the small lesion. The DI-SPECT Tl-201 images presented, are uncorrected for down-scatter, fully corrected for down-scatter, or down-scatter corrected w/o the effects of lead x-rays. For quantitative comparison, vertical and horizontal profiles through the images are given. As shown in these figures, uncorrected images grossly overestimate activity concentrations, while contrast is low as compared to virgin images. DI-SPECT Tl-201 images with full correction for down-scatter are almost equal

to the virgin images; accordingly, almost perfect correction for image bias is possible with MC simulation. DI-SPECT Tl-201 images corrected for down-scatter without taking the effects of lead x-rays into account are less accurate as compared to the fully corrected DI-SPECT Tl-201 images.

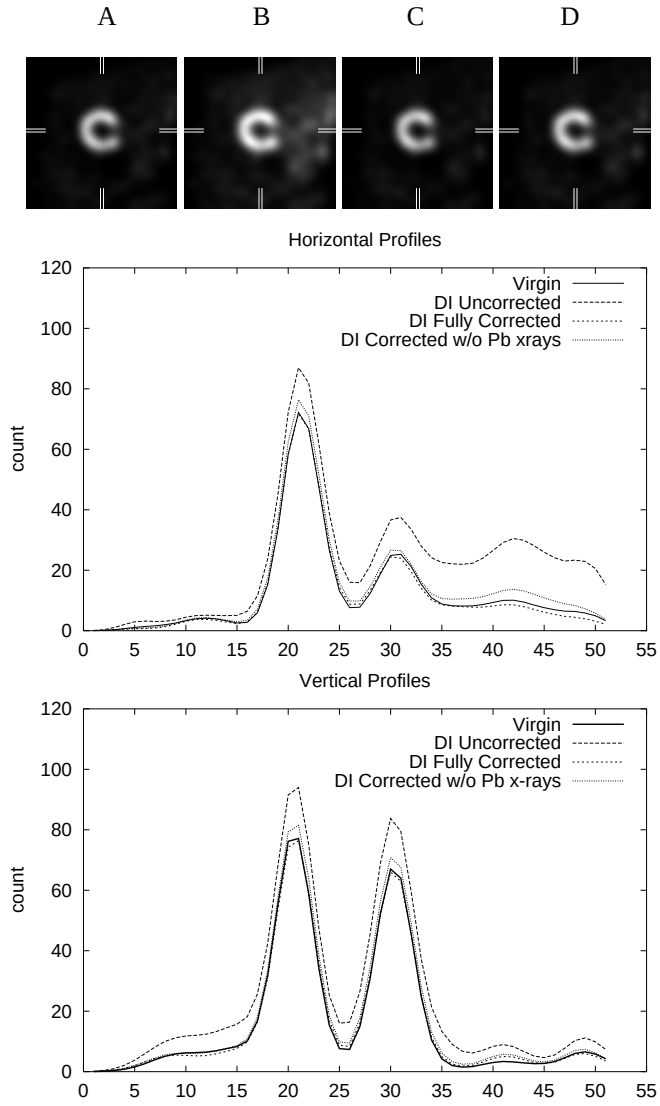

Figure 7.3: Slices of the Tl-201 short-axis images at the level of the large lesion. A: virgin Tl-201 image, B: uncorrected DI-SPECT Tl-201 image, C: fully corrected DI-SPECT Tl-201 image, D: DI-SPECT Tl-201 image corrected w/o Pb x-rays. Bottom: horizontal and vertical profiles through the short-axis images.

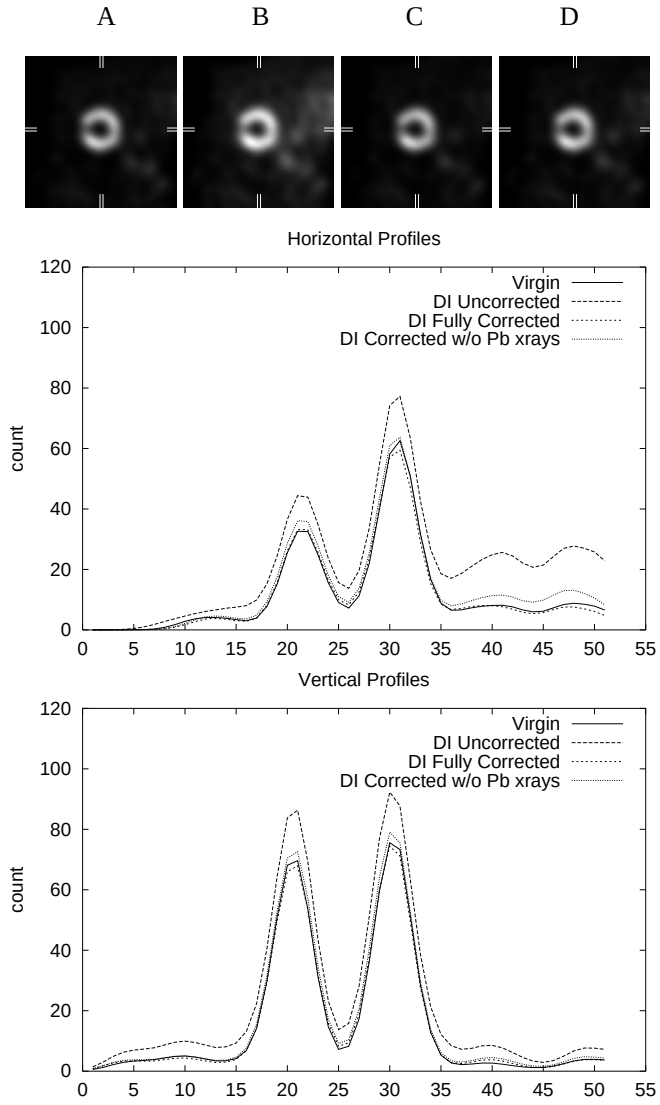

Figure 7.4: As Fig. 7.3 but now at the level of the small lesion.

In Figs. 7.5 and 7.6, short- and long-axis images are shown of the virgin Tl-201 image and the uncorrected and corrected DI-SPECT Tl-201 images. There is excellent agreement between virgin Tl-201 images and fully corrected DI-SPECT Tl-201 images.

Bulls-eye plots of the myocardium with lesions are shown in Fig. 7.3. The small and large lesions are clearly visible in all cases, however in the case of the uncorrected DI-SPECT Tl-201 image, the lesions appear to be smaller as compared to the virgin image. Circumferential profiles over the myocardial wall taken from the bulls-eye plot, confirm

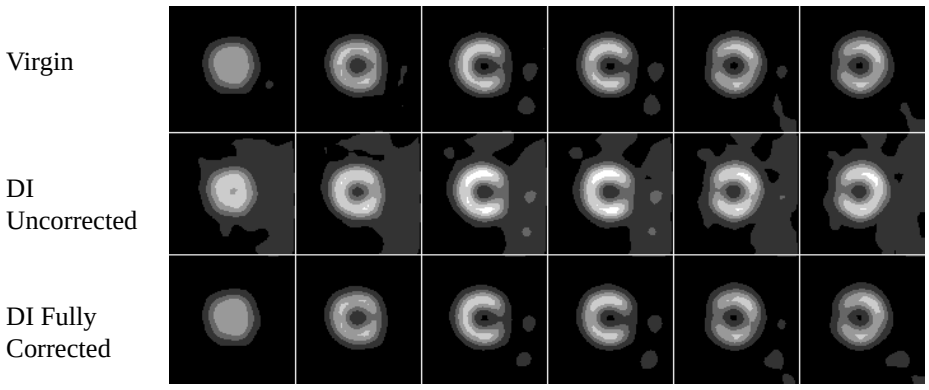

Figure 7.5: Short-axis images of Tl-201 reconstructions.

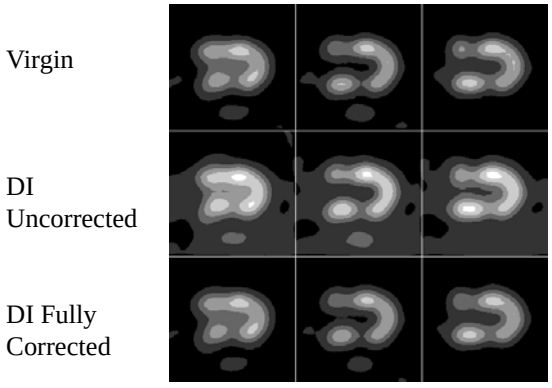

Figure 7.6: Long-axis images of Tl-201 reconstructions.

the excellent agreement between the virgin and the fully corrected images.

In order to assess uniformity of the corrected image, bulls-eye plots and circumferential profiles of the myocardium without lesions were made (Fig. 7.8). This experiment confirms the excellent agreement between virgin images and down-scatter corrected images. Furthermore, from the short-axis of the heart with and without lesions, average count levels were calculated in 5 regions, and compared with the average count level in the total myocardium (Tables 7.1 and 7.3). The count level in the fully corrected DI-SPECT Tl-201 image is almost equal to the count level in the virgin image, with errors as small as a few percent. Uniformity in the corrected DI-SPECT Tl-201 image is comparable with the virgin image.

During reconstruction of the Tl-201 images, lesion contrast but also noise tend to increase. In order to make a sensible assessment of the contrast-to-noise ratio of the images,

	virgin	DI Uncorrected	DI Fully Corrected
Total	80.9	99.4 (+23%)	79.6 (-2%)
Apex	84.4	102.3 (+21%)	83.3 (-1%)
Lateral Wall	84.8	103.8 (+18%)	84.9 (-0%)
Anterior Wall	78.9	96.3 (+22%)	76.8 (-3%)
Inferior Wall	71.1	90.7 (+28%)	68.2 (-4%)
Septal Wall	81.7	100.2 (+18%)	80.4 (-2%)

Table 7.1: Regional average count levels in the myocardium containing lesions. Values in brackets denote percentage deviation as compared to the average count level in the total myocardium.

	Virgin	DI Uncorrected	DI Fully Corrected
Total	83.9	101.1 (+20%)	81.4 (-3%)
Apex	82.9	99.6 (+20%)	80.9 (-2%)
Lateral Wall	85.4	103.1 (+17%)	84.0 (-2%)
Anterior Wall	86.1	101.8 (+18%)	82.2 (-4%)
Inferior Wall	81.0	102.0 (+26%)	78.8 (-3%)
Septal Wall	85.3	100.6 (+18%)	81.1 (-5%)

Table 7.2: Regional average count levels in the uniform myocardium. Values in brackets denote percentage deviation as compared to the average count level in the total myocardium.

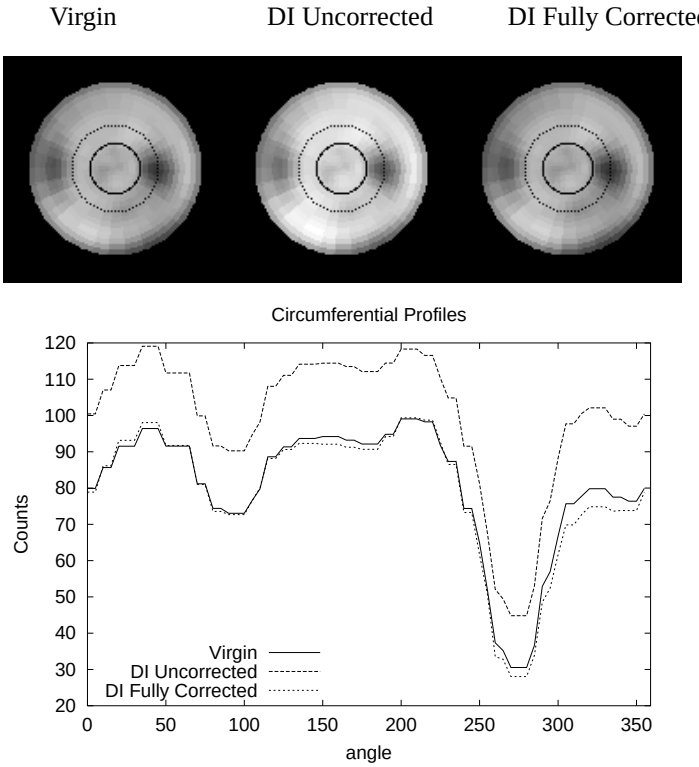

Figure 7.7: Top: Bulls-eye images and circumferential profiles (Center) of the Tl-201 images of the myocardium containing lesions. In the bulls-eye plots, the apex is denoted by the solid black line, while the position of the circumferential profiles shown is given by the dotted black line.

lesion contrast is shown as a function of noise in the myocardium (Fig. 7.9). These curves make it convenient to compare contrast at equal noise-levels and vice versa. The uncorrected DI-SPECT Tl-201 image has the lowest overall contrast-to-noise ratio, the virgin image the highest. Down-scatter correction of the DI-SPECT Tl-201 image increases contrast to noise, but not nearly to approach the ratio found in the virgin image. To illustrate that this lower contrast-to-noise is not due to inaccuracies of the Monte Carlo- based down-scatter correction, the contrast-noise curve of a DI-SPECT Tl-201 image corrected using a perfect down-scatter estimate is also included. This was done by using the scaled noise-free Tc-99m down-scatter projections which were measured apart from the Tl-201 projections in the phantom study, instead of simulated down-scatter projections.

Noise in the DI-SPECT Tl-201 image can be improved to the level as found in virgin Tl-201 images when more Tl-201 counts are acquired. This can be achieved by increasing the Tl-201 dose by about 12% (from 4 to 4.5 mCi), decreasing the Tc-99m dose by about 15% (from 25 to 21.7 mCi) and increasing the scan time by 15% (from 35 to 40

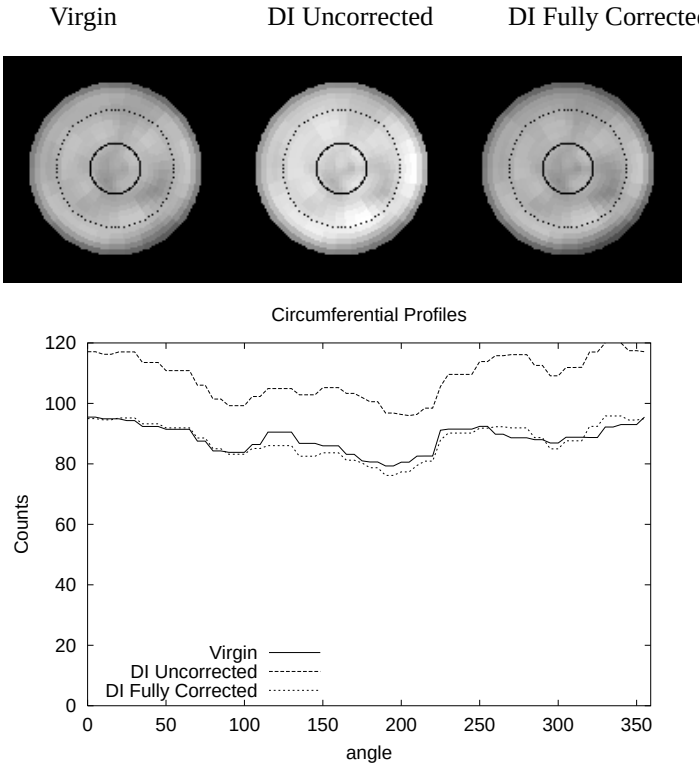

Figure 7.8: As in Fig. 7.3 but now for the myocardium without lesions.

sec./view). These adaptations result in about 30% extra Tl-201 counts, while Tc-99m counts remain unchanged. The contrast-to-noise results obtained with this adapted DI-SPECT acquisition protocol is also included in Fig. 7.9.

7.4 Discussion and Conclusions

The present study shows that, Monte Carlo-based down-scatter correction for Tc-99m/Tl-201 dual-isotope SPECT (DI-SPECT) is able to almost perfectly recover the quantitative accuracy of the Tl-201 images. Profiles through the lesions, circumferential profiles through the myocardial wall, bulls-eye plots and long and short-axis images show excellent agreement between the down-scatter corrected DI-SPECT Tl-201 images and the virgin Tl-201 image (seperately acquired, and hence not hampered by down-scatter). If the effects of lead x-rays are not included in the down-scatter correction, the accuracy of the results decreases slightly.

The noise level in the down-scatter corrected Tl-201 images is worse than that of the

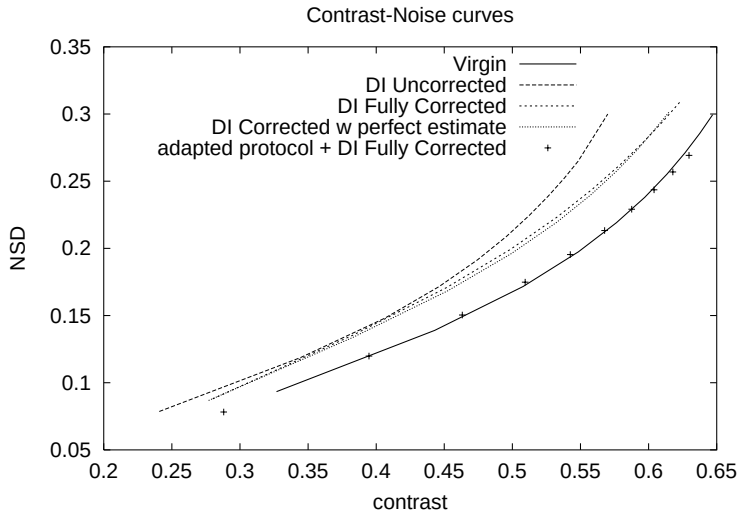

Figure 7.9: Lesion contrast as function of noise in myocardium. Virgin Tl-201 image compared to uncorrected and corrected DI-SPECT Tl-201 images acquired with the typical protocol or the adapted protocol. As a reference, correction with a perfect down-scatter estimate is also shown.

virgin Tl-201 image. This is caused by the fact that the down-scatter increases the mean intensity in the uncorrected DI-SPECT Tl-201 image and thus the variance. Correcting the DI-SPECT Tl-201 image with a noise-free down-scatter projection brings back the original mean, but still has the increased variance associated with the higher count level.

Fig. 7.10 illustrates this effect on sample projection data of a virgin Tl-201 study with a mean (i.e. average number of photons per pixel) of 50, an uncorrected DI-SPECT Tl-201 study (mean 100) and a corrected DI-SPECT Tl-201 study (mean 50). The uncorrected and corrected DI-SPECT Tl-201 images have a different mean but equal variance. In order to improve noise in down-scatter corrected DI-SPECT Tl-201 images, a slight adaption to the typical acquisition protocol is proposed, involving 15% longer scan time combined with 12% higher Tl-201 dose, and 15% lower Tc-99m dose. This conserves the amount of detected Tc-99m photons, while Tl-201 counts are increased by about 30%, resulting in a noise level in the DI-SPECT Tl-201 image that is comparable to that of a virgin Tl-201 image.

Increasing the scan time with a few minutes is acceptable, since the DI-SPECT protocol saves the time it takes to aquire one scan (20-30 minutes), as compared to the current clinical standard of seperate acquisition. However, adding a couple of minutes to the scan itself can lead to increased discomfort of the patient which increases the likelihood of motion artifacts. If not corrected for, patient motion can have significant impact on image quality.

Care should be also be taken when adapting injected doses. Although the Tc-99m

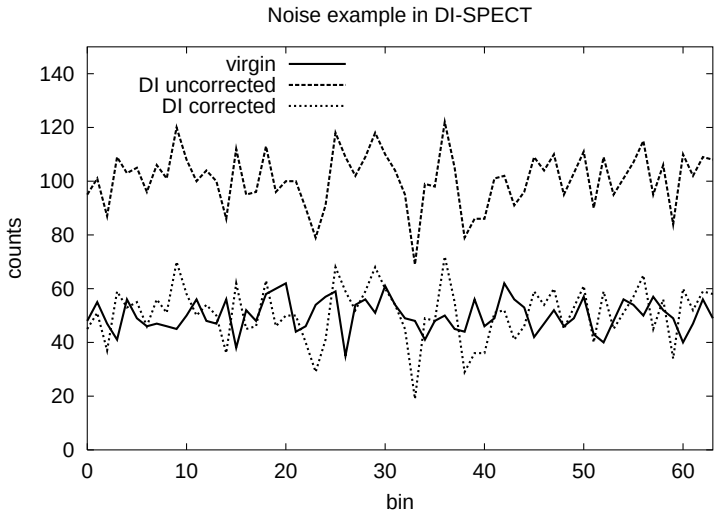

Figure 7.10: Effect of increased noise due to down-scatter, illustrated on sample projection profiles.

dose in the adapted protocol is decreased by 15%, this cannot compensate for the extra radiation load by the 12% increase in Tl-201 dose, since the decrease in effective dose of Tc-99m (-1 mSv) is much lower than the increased effective Tl-201 dose (+5 mSv). However, a small increase of the Tl-201 dose may be justified to achieve a more reliable simultaneous dual-isotope protocol [62]. Another consequence of the increased Tl-201 dose is the raised down-scatter from the 135 and 167 Tl-201 peaks in the Tc-99m image. Both Tc-99m down-scatter in the Tl-201 image and Tl-201 down-scatter in the Tc-99m image can be corrected for by simultaneously reconstruction of both Tl-201 and Tc-99m images [68]. The optimal trade-off between Tc-99m and Tl-201 image quality in combination with accurate down-scatter correction is subject of further study.

Recently, the feasibility of simultaneous Tc-99m/Tl-201 dual-isotope SPECT myocardial perfusion SPECT using a lower dose of Tc-99m was also proposed by Kwok et al. [78]. However, this was not combined with an increased scan time and no down-scatter correction was applied, so that both Tl-201 and Tc-99m image quality were compromised.

An alternative way to decrease noise in the corrected DI-SPECT Tl-201 image is to improve the efficiency of the SPECT system used, for instance by using fan-beam, or cone-beam collimator geometries [63, 118, 88, 10]. These systems have a 15%-40% higher efficiency as compared to parallel collimators. Another straightforward way to increase count rates, is to use more camera heads, e.g. triple-head instead of dual-head systems. However, triple-head systems are more expensive and often less versatile as compared to dual-head systems.

We have shown that Monte Carlo-based down-scatter correction has the potential to make dual-isotope SPECT reliable and robust, so that advantage can be taken of the many

favorable features of this protocol. Accurate simultaneous stress Tc-99m/rest Tl-201 cardiac SPECT is a significant step towards realizing a highly effective 'one-stop-shop' modality for management of patients with known or suspected coronary artery disease. The reconstruction methods proposed can straightforwardly be extended with ECG-gated acquisition of the Tc-99m image, so that comprehensive information about rest and stress perfusion with perfect registration between both images, viability and function can be obtained in a single scan, in a relative short time and with as little discomfort as possible.

Chapter 8

Summary and General Discussion

In Single Photon Emission Tomography (SPECT), three-dimensional images are reconstructed from a set of two-dimensional projections of radio-isotope distributions in the patient. As an example, these three-dimensional images can be used to non-invasively assess the myocardial perfusion, viability and functional characteristics as myocardial wall motion and ejection fractions. Frequently used radio-isotopes for perfusion imaging are Tc-99m and Tl-201. Various cardiac SPECT protocols are routinely used, of which most involve a separate study of the heart under stress and rest conditions. In simultaneous stress Tc-99m/rest Tl-201 dual-isotope SPECT, the images representing the rest and stress perfusion are acquired in a single scan. This has the advantage of reduced overall study time and perfect spatial registration of the cardiac images, while the unique characteristics of Tl-201 and Tc-99m labeled myocardial perfusion agents are combined.

The quality of the reconstructed SPECT image is degraded by physical factors such as photon attenuation, camera blurring and the detection of scattered photons. Quantitative accuracy of SPECT images improves when these factors are corrected for. Furthermore, in simultaneous Tc-99m/Tl-201 dual-isotope SPECT *down-scatter* of Tc-99m photons (emission energy 140 keV) contaminate the Tl-201 image (photopeak window around 70 keV), which can lead to gross overestimation of the accumulated activity, decreased lesion contrast or unwanted non-uniformities in the image.

An accurate and general way correct for attenuation, camera blurring and scatter is to employ a physical model of the formation of the projections during iterative SPECT reconstruction. To date, analytical models are used for this purpose, mainly because they are efficient in terms of computational burden. Most of these models work well for scatter correction in relatively uniform parts of the body (e.g. the head) and with radio-isotopes emitting high and medium energy photons (e.g., Tc-99m and I-123), but potentially fall short for scatter calculation in media with strong non-uniform mass densities (e.g., the thorax), with lower energy photons (e.g., Tl-201), or when used for model-based down-scatter correction in simultaneous dual-isotope SPECT.

This thesis starts with an investigation of the influence of *backscatter*. The complex nature of backscatter photon transport motivated us to study the Monte Carlo simulation method for calculation of SPECT projections. Monte Carlo simulation is a stochastic way (i.e. involving random numbers) for accurate calculation of general photon transport problems. A drawback is that Monte Carlo simulation can be very time-consuming, and therefore has been unattractive for clinical use. Several methods to accelerate Monte Carlo are introduced in this thesis, some to serve as a general scatter calculation tool in quantitative SPECT, some for specific calculation of down-scatter which is applied to a simultaneous Tc-99m/Tl-201 dual-isotope SPECT study.

8.1 Summary

In **chapter 2** the influence of backscatter, that is the contribution from behind the source, on scatter projections is investigated. It is shown that photons which scatter via material behind a Tc-99m source contribute significantly to the Tc-99m down-scatter in the Tl-201 photopeak projection, and therefore should be incorporated in the down-scatter model. Furthermore, backscatter is significant in general scatter calculation for Tl-201 SPECT. It is concluded that analytical models, which can be efficient for scatter correction in iterative SPECT reconstruction, are not appropriate for calculating down-scatter or Tl-201 scatter. For this reason, and because a more generic tool to efficiently calculate scatter could be very useful for image correction purposes, Monte Carlo simulation is revisited. In order to apply Monte Carlo simulation to iterative SPECT reconstruction, acceleration was required. In this thesis, this is achieved by combining Monte Carlo methods with analytical simulation methods.

In **chapter 3**, rapid and almost exact scatter projection calculation is achieved by transforming an analytically calculated scatter projection of an uniform dense object to the scatter projection of a non-uniform object (e.g. a thorax), using two condensed Monte Carlo simulations. Noise amplification is strongly suppressed by using correlated photon tracks, and by modeling the collimator and detector resolution analytically using blurring operations(Convolution-based Forced Detection (CFD)), rather than by employing the standard stochastic methods. By using these two acceleration methods the transformation can be performed about two orders of magnitude faster. Monte Carlo simulation with CFD alone converges to noise-free projections about 50 times faster than it does when traditional stochastic forced detection methods are used. CFD is validated as a stand-alone acceleration method for Monte Carlo simulation in **chapter 4**. Recently, iterative SPECT reconstruction schemes were demonstrated which make efficiently use of Monte Carlo simulation with CFD to achieve quantitative SPECT [6].

The improvement of simultaneous Tc-99m/Tl-201 dual-isotope SPECT reconstruction is the main theme of the second part of this thesis. Accurate reconstruction of simultaneous dual-isotope SPECT requires correction of Tc-99m down-scatter contaminating the Tl-201 image. This can be achieved by calculation of the down-scatter during reconstruction.

In **chapter 5** Rotation-based Monte Carlo (RMC) is proposed to accelerate Monte Carlo simulation of down-scatter. RMC is based on the Monte Carlo simulation of only a few projections of the total SPECT study and then takes a short-cut to rapidly estimate the other projections. RMC was combined with CFD, resulting in a speed-up of more than 1000 as compared to standard Monte Carlo simulation, without significant loss of accuracy.

Besides detection of Tc-99m photons which have scattered in the patient, in Tc-99m/Tl-201 dual-isotope SPECT a significant percentage of the total down-scatter is caused by lead x-rays. Lead x-rays are emitted from the collimator lead after absorption of Tc-99m photons, and have an energy which falls in the Tl-201 photopeak window. In **chapter 6** a method is described to incorporate detection of lead x-rays into the RMC method. Excellent agreement between experimentally measured down-scatter projections and simulated projections was demonstrated in this study.

In **chapter 7**, the results of Monte Carlo-based down-scatter correction in simultaneous Tc-99m/Tl-201 dual-isotope SPECT are described. Monte Carlo-based down-scatter using RMC and CFD almost perfectly recovers bias errors in the Tl-201 images. The noise level of the Tl-201 images in simultaneous dual-isotope SPECT can be improved to that of a sequentially acquired Tl-201 image, when the injected Tc-99m and Tl-201 dose and scan time are slightly adapted.

8.2 General Discussion

This discussion focuses on several aspects of cardiac SPECT and the application of simultaneous dual-isotope SPECT. Although the potential benefits of the simultaneous dual-isotope SPECT protocol are tremendous, there are also some pitfalls which have to be considered. Furthermore, cardiac SPECT is compared to other cardiac imaging modalities which are used in clinical practice nowadays or may become clinically available in the near future.

8.2.1 Cardiac SPECT

In the Netherlands (16 million inhabitants) about 65.000 people per year with known or suspected coronary artery disease are evaluated with SPECT myocardial perfusion imaging. Information about perfusion and viability is based on studying the myocardial perfusion under stress and rest conditions. Because of the favorable imaging characteristics (see chapter 1), tracers based on Tc-99m are often used for both studies, which has the disadvantage that the second study can not be initiated before the activity of the first study has cleared. Other protocols involve Tl-201 for stress and redistribution imaging, or separate stress Tc-99m / rest Tl-201 dual-isotope (Fig. 8.1, top bar) [19]. In these protocols, every rest or stress SPECT scan takes about 20 - 30 minutes each. In simultaneous stress Tc-99m / rest Tl-201 dual-isotope SPECT the rest and the stress images are acquired in one scan (Fig. 8.1, bottom bar); First Tl-201 is injected in rest. The Tl-201 accumulates in viable myocardial cells proportional to the regional blood-flow. Next, the patient's heart is stressed by a pharmacon or by exercise. At peak stress Tc-99m is injected. A simultaneous Tc-99m/Tl-201 scan can be acquired about 20 minutes later. The total study time of a protocol involving a sequential Tl-201/Tc-99m acquisition takes at least 90 minutes, whereas the simultaneous protocol takes about 50 minutes [19]. Implementation of this simultaneous SPECT protocol could significantly shorten patient waiting lists. The protocol not only substantially abbreviates the overall study duration for the patient, but more important, the inherent perfect registration of stress and rest image sets can reduce the frequency of unrecognized artifacts associated with separate stress and rest image acquisitions.

The simultaneous dual-isotope SPECT protocol, however, rests on the assumption that the effects of Tc-99m down-scatter in the Tl-201 image can be accounted for. In many proposed correction methods intermediate energy-windows and fixed parameters are used to estimate the down-scatter, although these parameters ideally should be patient

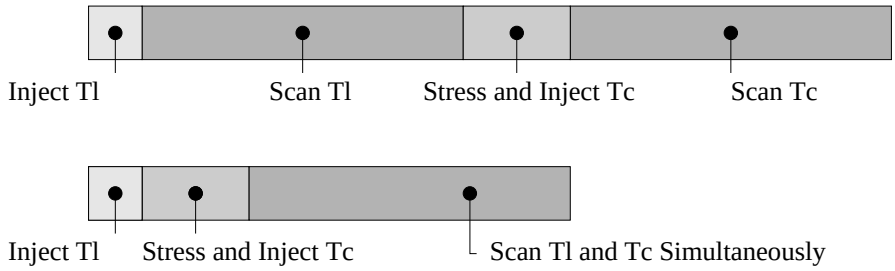

Figure 8.1: Schematic representation of a sequential (Top bar) and a simultaneous stress Tc-99m/ rest Tl-201 cardiac SPECT protocol (Bottom bar). The white areas indicate time reserved for getting the necessary metabolism of the radio-nuclide.

specific. Furthermore, the significant noise in the down-scatter estimate will prolongate in the corrected Tl-201 image. An advantage of energy window-based methods is that they are easy to implement, and quite independent to the imaging geometry used.

Compared to this, correcting for down-scatter using Monte Carlo simulation is more complex, but has some important advantages. Noise in the down-scatter estimate is reduced since this estimate is based on a summation of Tc-99m image-voxels which often have relative low noise. Furthermore, it is based on sound physical assumptions, hence does not require *a priori* patient specific knowledge. These features make Monte Carlo based (down-)scatter correction applicable to a broad range of imaging procedures.

It would be highly desirable if a cardiac image procedure would give accurate information about perfusion, viability and function such as ejection fractions in a single scan ('one-stop shop' principle [75]), in a relative short time and with little discomfort. Both tissue viability and perfusion can be acquired using the simultaneous dual-isotope protocol. If the acquisition is ECG-gated, SPECT yields valuable information about the function of the heart, while blurring of the image due to contraction and relaxation of the heart wall, is also prevented. Furthermore, SPECT accuracy can be significantly improved, when correction for major image degrading factors, such patient and respiration motion, photon attenuation, blurring and scatter is possible. While the effects of respiration motion can be reduced by gated acquisition, the other factors can be included during reconstruction. by using photon transport models such as presented in this work [11, 61, 98]. Hence, gated acquisition of simultaneous dual-isotope SPECT combined with accurate reconstruction to compensate for degrading factors, would yield an accurate cardiac imaging method which has the advantage of measuring perfusion, viability and function in one acquisition without additional negative side-effects for the patient.

8.2.2 Cardiac SPECT versus other cardiac imaging modalities

Clinically mature cardiac imaging methods include, apart from SPECT, contrast angiography and echocardiography. Among the emerging technologies in cardiac imaging are 3D echocardiography, electron beam CT, magnetic resonance imaging/angiography and

Positron Emission Tomography (PET). Each modality has unique advantages and disadvantages and often provide complementary information. In general, comprehensive cardiac imaging assessment should include information about morphology (anatomy), function and viability, perfusion or metabolism, but no single modality nowadays realizes all of these goals simultaneously.

Echocardiography is often used for initial functional investigations, but perfusion imaging using echo is not yet feasible for routine daily practice. The modality is convenient, portable and wide-spread but gives results which are operator-dependent (e.g. [21]). Contrast angiography is often used for accurate localization of coronary artery stenosis, but is not 3D, quantifies and visualizes the lumen and patency of the coronary arteries instead of direct myocardial perfusion, involves certain patient risks because of its invasive nature and is expensive (e.g. [112, 103]). CT images have a high resolution which can be used to localize coronary atherosclerosis, but cannot image perfusion or the physiological significance of coronary stenosis (e.g. [20]), MRI can excellently image function, although perfusion imaging using contrast media is still in an experimental stadium (e.g. [37]). PET FDG (fluorine-18 fluorodeoxyglucose) is considered the reference standard for assessing myocardial viability, but suffers from limited availability and high costs, and is therefore often used as an optional completion to SPECT perfusion imaging [127].

SPECT has a lower resolution as compared to most other 3D imaging modalities, but can image perfusion and function at low costs. SPECT is wide-spread so that a lot of experience in the last decades has been acquired concerning diagnosis and prognosis [95, 77, 25]. Other unique features include the possibility to acquire a stress image minutes after exercise (retrospective imaging), by the use of radio-labeled molecules which accumulate in the cells. Finally, if (gated) simultaneous dual-isotope Tc-99m/Tl-201 SPECT is available, rest and stress perfusion, viability and functional information can be obtained from one scan, which makes the modality highly competitive [52].

8.3 Conclusions and Recommendations

Monte Carlo simulation of SPECT was accelerated and applied to down-scatter correction in simultaneous dual-isotope SPECT reconstruction. Acceleration of the Monte Carlo-based correction method is necessary since the method is generally time consuming, which makes it unattractive for clinical use. The following conclusions can be drawn from this thesis.

- Simulation of projections for application to SPECT reconstruction is often too complex to achieve with contemporary analytical models (chapter 2).
- Monte Carlo simulation of scatter and down-scatter in SPECT can be tremendously accelerated when stochastic Monte Carlo simulation methods are combined with analytical simulation methods. This makes application of Monte Carlo simulation for (down-)scatter correction in SPECT feasible within clinical acceptable computation times (chapters 2, 3, 4, 5 and 6).

- Accelerated Monte Carlo simulation of down-scatter is almost perfectly able to recover quantitative accuracy of the Tl-201 images, when applied to Tc-99m/Tl-201 dual-isotope SPECT reconstruction, but the down-scatter induced noise is still to be addressed (chapter 7).
- Accurate simultaneous Tc-99m/Tl-201 dual-isotope SPECT is an important step forward towards comprehensive cardiac evaluation in a single scan ('one-stop shop'), which can be achieved by straightforward combination with ECG gated acquisition.

The applicability and the accuracy of Monte Carlo-based scatter correction depends on several extrinsic factors, some of which the impact has still to be investigated. Further study has to point out, for instance, how sensitive the down-scatter estimate depends on the quality of the attenuation map, the stability of energy window settings etc. . The resolution, noise and quantitative accuracy of the attenuation map depends on the transmission systems used and the amount of down-scatter into the transmission window. In addition, the acquisition protocol could be further refined regarding administered activity doses, window setting and scan times. Also, new hardware developments (e.g. converging beam collimators, semiconductor detectors) will have their impact on these protocols.

The accuracy of the Monte Carlo-based down-scatter calculation was demonstrated using phantom experiments (chapter 7 and 8). Patient studies will have to prove the usefulness of Monte Carlo simulation in clinical image reconstruction.

Bibliography

[1] H. Almquist, H. Arheden, A. Arvidsson, O. Pahlm and J. Palmer, "Clinical implication of down-scatter in attenuation-corrected myocardial SPECT", *J. Nucl. Cardiology*, vol. 6, no. 4, pp. 406–411, 1999.

[2] P. Andreo, "Monte Carlo techniques in medical radiation physics", *Phys. Med. Biol.*, vol. 36, no. 7, pp. 861–920, 1991.

[3] H. Asano, S. Takahito, T. Hideyuki, H. Sassa, K. Takeshima, Y. Miyazaki, K. Okumura, H. Hashimoto and T. Ito, "Diagnosis of right ventricular infarction by overlap images of simultaneous dual emission computed tomography using Technetium-99m Pyrophosphate and Thallium-201", *Am. J. Cardiology*, vol. 71, pp. 902–908, 1993.

[4] J. W. Beck, R. J. Jaszczak, R. E. Coleman, C. F. Sterner and P. Nolte, "Analysis of SPECT including scatter and attenuation using sophisticated Monte Carlo modeling methods", *IEEE Trans.Nucl.Sci.*, vol. 29, pp. 506–511, 1982.

[5] F. J. Beekman, H. W. A. M. de Jong and E. T. P. Slijpen, "Efficient SPECT Scatter Response Estimation in Non-Uniform Media using Correlated Monte Carlo Simulations", *Phys.Med.Biol.*, vol. 44, pp. N183–N192, 1999.

[6] F. J. Beekman, H. W. A. M. de Jong and S. van Geloven, "Efficient Monte Carlo based fully 3D SPECT reconstruction", *submitted*.

[7] F. J. Beekman, J. M. den Harder, M. A. Viergever and P. P. van Rijk, "SPECT Scatter Modeling in Non-Uniform Attenuating Objects", *Phys.Med.Biol.*, vol. 42, pp. 1133–1142, 1997.

[8] F. J. Beekman, E. G. J. Eijkman, M. A. Viergever, G. F. Borm and E. T. P. Slijpen, "Object Shape Dependent PSF Model for SPECT imaging", *IEEE Trans.Nucl.Sci.*, vol. 40, pp. 31–39, 1993.

[9] F. J. Beekman, C. Kamphuis and E. C. Frey, "Scatter Correction Methods in 3D Iterative SPECT Reconstruction: A Simulation Study.", *Phys.Med.Biol.*, vol. 42, pp. 1619–1631, 1997.

[10] F. J. Beekman, C. Kamphuis, B. F. Hutton and P. P. van Rijk, "Half-Fan-Beam Collimators Combined With Scanning Point Sources For Simultaneous Emission Transmission Imaging", *J. Nucl. Med.*, vol. 39, pp. 1996–2003, 1998.

[11] F. J. Beekman, C. Kamphuis, M. A. King, P. P. van Rijk and M. A. Viergever, "Improvement of image resolution and quantitative accuracy in clinical Single Photon Emission Computed Tomography.", *Comput. Med. Imaging Graph.*, vol. 25(2), pp. 135–146, 2001.

[12] F. J. Beekman, C. Kamphuis, E. T. P. Slijpen and P. P. van Rijk, "Model-Based Down-Scatter Correction of Attenuation Maps in Simultaneous Emission Transmission Imaging", *J.Nucl.Med.*, vol. 39, p. 178P, 1998.

[13] F. J. Beekman, C. Kamphuis and M. A. Viergever, "Improved Quantitation in SPECT Imaging Using Fully 3D Iterative Spatially Variant Scatter Compensation", *IEEE Trans.Med.Im.*, vol. 15, pp. 491–499, 1996.

[14] F. J. Beekman, E. T. P. Slijpen, H. W. A. M. de Jong and M. A. Viergever, "Estimation of the Depth Dependent component of Point Spread Function of SPECT", *Med. Phys.*, vol. 26, pp. 2311–2322, 1999.

[15] F. J. Beekman, E. T. P. Slijpen, H. W. A. M. de Jong and M. A. Viergever, "Point Spread Function Determination of SPECT", *Proceedings of the 1999 International Meeting on Fully Three-Dimensional Image Reconstruction in Radiology and Nuclear Medicine*, pp. 297–300, 1999.

[16] F. J. Beekman, E. T. P. Slijpen and W. J. Niessen, "Selection of Task-Dependent Diffusion Filters for the Post-Processing of SPECT Images", *Phys.Med.Biol.*, vol. 43, pp. 713–730, 1998.

[17] F. J. Beekman and M. A. Viergever, "Fast SPECT Simulation Including Object Shape Dependent Scatter", *IEEE Trans.Med.Im.*, vol. 14, pp. 271–282, 1995.

[18] M. J. Berger, J. H. Hubbell, S. M. Seltzer, J. S. Coursey and D. S. Zucker, "XCOM: Photon Cross Section Database (version 1.2), [Online].", 1999.

[19] D. S. Berman, H. Kiat, K. Van Train, J. D. Friedman, F. P. Wang and G. Germano, "Dual-isotope myocardial perfusion SPECT with rest thallium-201 and stress Tc-99msestamibi", *Nuclear Cardiology*, vol. 12, no. 2, pp. 261–270, 1994.

[20] D. S. Berman, E. F. Schisterman, R. Miranda, J. D. Friedman, S. W. Hayes, H. C. Lewin and G. Germano, "Nuclear cardiology and electron-beam computed tomography: competitive or complementary?", *Am. J. Cardiol.*, vol. 19, pp. 51E–55E, 2001.

[21] R. Bigi, "Complications of pharmacologic stress echocardiography in coronary artery disease.", *Clin. Cardiol.*, vol. 19, pp. 776–80, 1996.

[22] J. E. Bowsher and C. E. Floyd, "Treatment of Compton Scattering in Maximum Likelihood, Expectation Maximization Reconstructions of SPECT images", *J.Nucl.Med.*, vol. 32, pp. 1285–1291, 1991.

[23] J. F. Briesmeister, *MCNP-A General Monte Carlo N-Particle Transport Code, Version 4B*, Report LA-12625-M, Los Alamos National Laboratory, 1993.

[24] I. Buvat, H. Benali, A. Todd-Pokropek and R. DiPaola, "Scatter correction in scintigraphy: State of the art", *Eur. J. Nucl. Med.*, vol. 21, pp. 675–694, 1994.

[25] J. M. Cacciabaudo and M. Szulc, "Gated cardiac SPECT: has the addition of function to perfusion strengthened the value of myocardial perfusion imaging?", *J Nucl Med.*, vol. 42, pp. 1043–9, 2001.

[26] Z. Cao, C. C. Chen, C. Manoury, L. E. Holder, T. C. Abraham and A. Tehan, "Phantom Evaluation of Simultaneous Thallium-201/Technetium-99m Acquisition in Single Photon Emission Tomography", *Eur. J. Nucl. Med.*, vol. 23, pp. 1514–1520, 1996.

[27] Z. J. Cao, E. C. Frey and B. M. W. Tsui, "A scatter model for parallel and converging beam SPECT based on the Klein-Nishina formula", *IEEE Trans.Nucl.Sci.*, vol. 41, pp. 1594–1600, 1994.

[28] A. H. Compton, "A quantum theory of scattering of X-rays by light elements", *Phys. Rev.*, vol. 21, pp. 483–502, 1923.

[29] H. W. A. M. de Jong and F. J. Beekman, "Rapid SPECT simulation of down-scatter in non-uniform media", *Phys.Med.Biol.*, vol. 46, no. 3, pp. 621 – 635, 2001.

[30] H. W. A. M. de Jong, F. J. Beekman, M. Ljungberg and P. P. van Rijk, "The influence of backscatter on Tc99m and Tl201 line source responses.", *Phys. Med. Biol.*, vol. 44, pp. 665–679, 1999.

[31] H. W. A. M. de Jong, F. J. Beekman and E. T. P. Slijpen, "Acceleration of Monte Carlo SPECT simulation using convolution-based forced detection", *Conference Record of 1999 IEEE Nuclear Science Symposium and Medical Imaging Conference, Seattle*, 1999.

[32] H. W. A. M. de Jong, M. Gieles, M. Ljungberg and F. J. Beekman, "Validation of a fast simulator for clinical SPECT simulation", *J.Nucl.Med.*, vol. 42, p. 14P, 2001.

[33] H. W. A. M. de Jong, E. T. P. Slijpen and F. J. Beekman, "Utrecht Monte Carlo System for SPECT, Tech. Report 99-2", *Nuclear Medicine Physics Group, Utrecht University Hospital*, 1999.

[34] H. W. A. M. de Jong, E. T. P. Slijpen and F. J. Beekman, "Acceleration of Monte Carlo SPECT simulation using convolution-based forced detection", *IEEE Trans.Nucl.Sci.*, vol. 48, no. 1, pp. 58–64, 2001.

[35] H. W. A. M. de Jong, W. T. Wang, E. C. Frey and F. J. Beekman, "Fast Monte Carlo simulation of down-scatter for dual-isotope SPECT including gamma interaction with crystal and lead.", *J.Nucl.Med.*, vol. 42, pp. 193P–194P, 2001.

[36] H. W. A. M. de Jong, W. T. Wang, E. C. Frey, M. A. Viergever and F. J. Beekman, "Fast Monte Carlo simulation of SPECT down-scatter including gamma interactions with crystal and lead", *submitted to Med. Phys.*, 2001.

[37] A. de Roos, P. Kunz, H. LAmb, L. Kroft, S. Langerak, J. Doornbos and E. van der Wall, "Magnetics Resonance Imaging of ischemic heart disease: why cardiac magnetic resonance imaging will play a signicant role in the management of patients with coronary artery disease", *J. Comput. Assist. Tomogr.*, vol. 23, pp. S135–41, 1999.

[38] G. Dejonghe, J. Gonnord and J. C. Nimal, "Studies of Perturbations using Correlated Monte Carlo Method", *Oak Ridge National Lab*, vol. ORNL/RISDC-44, pp. 63–95, 1980.

[39] A. P. Dempster, N. M. Liard and D. B. Rubin, "Maximum Likelihood from incomplete data via the EM-algorithm", *J.Roy.Stat.Soc.*, vol. 39, pp. 1–38, 1977.

[40] E. Gordon DePuey, "Simultaneous Thallium-201/Technetium-99m dual-isotope cardiac SPECT: Ready for prime-time?", *J. Nucl. Med.*, vol. 34, no. 11, pp. 2006–2008, 1993.

[41] E. Gordon dePuey, E. V. Garcia and D. S. Berman, *Cardiac SPECT Imaging, second edition*, Lippincott Williams and Wilkins, Philadelphia, 2001.

[42] R. D. Evans, *The Atomic Nucleus*, Krieger, Malabar, Florida, 1982.

[43] G. El Fakhri, S. C. Moore, P. Maksud, A. Aurengo and M. F. Kijewski, "Absolute activity quantitation in simultaneous 123I/99mTc brain SPECT.", *J. Nucl. Med.*, vol. 42, pp. 300–308, 2001.

[44] E. P. Ficaro, J. A. Fessler, P. D. Shreve, J. N. Kritzman, P. A. Rose and J. R. Corbett, "Simultaneous Transmission/Emission Myocardial Perfusion Tomography. Diagnostic Accuracy of Attenuation-Corrected 99mTc-Sestamibi Single-Photon Emission Computed Tomography", *Circulation*, vol. 93, pp. 463–473, 1996.

[45] C. E. Floyd, R. J. Jaszczak and R. E. Coleman, "Scatter detection in SPECT-imaging: dependence on source depth, energy, and energy window", *Phys.Med.Biol.*, vol. 33, pp. 1075–1081, 1988.

[46] C. E. Floyd, R. J. Jaszczak, K. L. Greer and R. E. Coleman, "Inverse Monte Carlo as an unified reconstruction algorithm for ECT", *J.Nucl.Med.*, vol. 27, pp. 1577–1585, 1986.

[47] E. C. Frey and B. M. W. Tsui, "A Practical Method for Incorporating Scatter in a Projector-Backprojector for Accurate Scatter Compensation in SPECT", *IEEE Trans.Nucl.Sci.*, vol. 40, pp. 1107–1116, 1993.

[48] E. C. Frey and B. M. W. Tsui, "Modeling the Scatter Response Function in Inhomogeneous Scattering Media for SPECT", *IEEE Trans.Nucl.Sci.*, vol. 41, pp. 1585–1593, 1994.

[49] E. C. Frey and B. M. W. Tsui, "A New Method for Modelling the Spatially Variant Object Dependent Scatter Response Function in SPECT", *1996 IEEE Nuclear Science Symposium Conference Record, Anaheim, CA, November 1996*, pp. 1082–1086, 1996.

[50] E. C. Frey, B. M. W. Tsui and J. R. Perry, "Simultaneous Acquisition of Emission and Transmission Data for Improved Thallium-201 Cardiac SPECT imaging Using a Technetium-99m Transmission Source", *J.Nucl.Med.*, vol. 33, pp. 2238–2245, 1992.

[51] G. Germano, P. B. Kavanagh, P. Waechter, J. Areeda, S. Van Kriekinge and D. S. Berman T. Sharir T, Lewin HC, "A new algorithm for the quantitation of myocardial perfusion SPECT. I: technical principles and reproducibility.", *J. Nucl. Med.*, vol. 41, pp. 712–9, 2000.

[52] R. Hachamovitch, "Clinical application of rest Thallium-201/stress Technetium-99m sestamibi dual-isotope myocardial perfusion single-photon emission computed tomography", *Card. Rev.*, vol. 7, no. 2, pp. 83–91, 1999.

[53] G. J. Hademenos, M. Dahlbom and E. J. Hoffman, "Simultaneous dual-isotope Technetium-99m/Thallium-201 cardiac SPET imaging using a projection-dependent spilldown correction factor", *Eur.J.Nucl.Med.*, vol. 22, no. 5, pp. 465–472, May 1995.

[54] P. Hannequin, J. Mas and G. Germano, "Photon energy recovery for cross-talk correction in simultaneous Tc-99m/Tl-201 imaging", *J. Nucl. Med.*, vol. 41, no. 4, pp. 728–736, 2000.

[55] R. L. Harrison, S. B. Gillespie, S. D. Vannoy, M. S. Kaplan and T. K. Lewellen, "A public domain simulation system for emission tomography: photon tracking through heterogeneous attenuation using importance sampling", *J. Nucl. Med.*, vol. 34, p. 60P, 1993.

[56] D. R. Haynor, *Variance Reduction Techniques*, In: Monte Carlo Calculations in Nuclear Medicine, M. Ljungberg and S. E. Strand and M. A. King eds, IOP Publishing, pp. 145–163, Bristol, UK, 1998.

[57] D. R. Haynor, R. L. Harrison and T. K. Lewellen, "The use of importance sampling techniques to improve the efficiency of photon tracking in emission tomography simulations", *Med. Phys*, vol. 18, no. 5, pp. 990–1001, 1991.

[58] E. N. Heller, P. DeMan, Y. H. Liu, D. P. Dione, I. G. Zubal, F. T. Wackers and A. J. Sinusas, "Extracardiac Activity Complicates Quantitative Cardiac SPECT Imaging Using a Simultaneous Transmission-Emission Approach", *J.Nucl.Med.*, vol. 38, pp. 1882–1890, 1997.

[59] H. M. Hudson and R. S. Larkin, "Accelerated image reconstruction using ordered subsets of projection data", *IEEE Trans.Med.Im.*, vol. 13, pp. 601–609, 1994.

[60] B. F. Hutton and V. Baccarne, "Efficient Scatter Modelling for Incorporation in Maximum Likelihood Reconstruction", *Eur. J. Nucl. Med.*, vol. 25, pp. 1658–1665, 1998.

[61] B. F. Hutton, H. M. Hudson and F. J. Beekman, "A Clinical Perspective of Accelerated Statistical Reconstruction", *Eur. J. Nucl. Med.*, vol. 24, pp. 797–808, 1997.

[62] ICRP-52, "Protection of the patient in nuclear medicine. ICRP publication 52", *Annals of the ICRP*, vol. 17, 1987.

[63] R. J. Jaszczak, D.R. Gilland, M.W. Hanson, S. Jang, K. L. Greer and R.E. Coleman, "Fast Transmission CT for Determining Attenuation Maps Using a Collimated Line Source, Rotatable Air-Copper-Lead Attenuators and Fan Beam Collimation", *J. Nucl. Med.*, vol. 34, pp. 1577–1586, 1993.

[64] R. J. Jaszczak, K. L. Greer and C. E. Floyd, "Improved SPECT quantification using compensation for scattered photons", *J. Nucl. Med.*, vol. 25, pp. 893–900, 1984.

[65] D. J. Kadrmas, *Application of Reconstruction-Based Scatter Compensation to Single- and Dual-Isotope SPECT Imaging.*, Ph.D. thesis, The University of North Carolina at Chapel Hill, 1997.

[66] D. J. Kadrmas, E. C. Frey, S. S. Karimi and B. M. W. Tsui, "Fast implementation of reconstruction based scatter compensation in fully 3D SPECT image reconstruction", *Phys.Med.Biol.*, vol. 43, pp. 857–873, 1998.

[67] D. J. Kadrmas, E. C. Frey and B. M. W. Tsui, "Application of Reconstruction-Based Scatter Compensation to Tl-201 SPECT: Implementations for Reduced Image Noise", *IEEE Trans.Med.Im.*, vol. 17(3), pp. 325–333, 1998.

[68] D. J. Kadrmas, E. C. Frey and B. M. W. Tsui, "Simultaneous technetium-99m/thallium-201 SPECT imaging with model-based compensation for cross-contaminating effects", *Phys.Med.Biol.*, vol. 44(7), pp. 1843–60, 1999.

[69] C. Kamphuis and F. J. Beekman, "Accelerated Iterative Transmission CT Reconstruction using an Ordered Subset Convex Algorithm", *IEEE Trans.Med.Im.*, vol. 17, pp. 1101–1105, 1998.

[70] C. Kamphuis, F. J. Beekman and M. A. Viergever, "Evaluation of OS-EM for 1D, 2D and fully 3D SPECT Reconstruction", *IEEE Trans.Nucl.Sc.*, vol. 43, pp. 2018–2024, 1996.

[71] C. Kamphuis, F. J. Beekman, M. A. Viergever and P. P. van Rijk, "Dual Matrix Ordered Subset Reconstruction for Accelerated 3D Scatter Correction in SPECT", *Eur. J. Nucl. Med.*, vol. 25, pp. 8–18, 1998.

[72] H. Kiat, G. Germano, J. Friedman, K. van Train, G. Silagan, F. Wang, J. Maddahi and D. Berman, "Comparative Feasibility of Separate or Simultaneous Rest Thallium-201/Stress Technetium-99m-Sestamibi Myocardial Perfusion SPECT", *J.Nucl.Med.*, vol. 35, pp. 542–548, 1994.

[73] K. Knesaurek, "A new dual-isotope convolution cross-talk correction method:A Tl-201/Tc-99m SPECT cardiac phantom study", *Med. Phys.*, vol. 21, no. 10, pp. 1577–1583, 1994.

[74] K. Knesaurek and J. Machac, "A transformation cross-talk technique for simultaneous dual radionuclide imaging: a myocardial perfusion Tl-201/Tc-99m sestamibi dog SPECT study", *British J. Rad.*, vol. 72, pp. 872–881, 1999.

[75] C. M. Kramer, "Integrated approach to ischemic heart disease. The one-stop shop.", *Cardiol Clin 1998 May;16(2):267-76*, vol. 16, pp. 267–76, 1998.

[76] T. Krause, W. Kasper, T. Meinertz, M. Schnitzler, H. Just, C. Schumichen and E. Moser, "Comparison in acute myocardial infarction of anisoylated plasminogen streptokinase activator complex versus heparin evaluated by simultaneous thallium-201/technetium-99m pyrophosphate tomography", *Am. J. Cardiology*, vol. 71, pp. 8–13, 1993.

[77] S. Kumita, K. Cho, H. Nakajo, M. Toba, T. Kijima, S. Mizumura, T. Oshina, T. Kumazaki, J. Sano, K. Sakurai and K. Munakata, "Serial assessment of left ventricular function during dobutamine stress by means of electrocardiography-gated myocardial SPECT: combination with dual-isotope myocardial perfusion SPECT for detection of ischemic heart disease.", *J. Nucl. Cardiol.*, vol. 8, pp. 152–7, 2001.

[78] C. G. Kwok, S. Wu, H. P. Tsang and H. W. Strauss, "Feasibility of simultaneous dual-isotope myocardial perfusion acquisition using a lower dose of sestamibi", *Eur. J. Nucl. Med.*, vol. 24, no. 3, pp. 281–285, 1997.

[79] K. J. LaCroix, B. M .W. Tsui and B. H. Hasegawa, "A Comparison of 180° and 360° Acquisition for Attenuation-Compensated Thallium-201 SPECT Images", *J. Nucl. Med.*, vol. 39, pp. 562–574, 1998.

[80] K. Lange and R. Carson, "E.M. Reconstruction algorithms for emission and transmission tomography", *J.Comput.Assist.Tomog.*, vol. 8, pp. 306–316, 1984.

[81] R. M. Leahy and J. Qi, "Statistical approaches in quantitative positron emission tomography", *Stat. Comput.*, vol. 10, pp. 147–65, 2000.

[82] M. Ljungberg, *The SIMIND Monte Carlo program*, In: Monte Carlo Calculations in Nuclear Medicine, M. Ljungberg and S. E. Strand and M. A. King eds, IOP Publishing, pp. 145–163, Bristol, UK, 1998.

[83] M. Ljungberg and S. E. Strand, "A Monte Carlo program for the simulation of scintillation camera characteristics", *Comp.Meth.Prog.Biomed.*, vol. 29, pp. 257–272, 1989.

[84] M. Ljungberg and S. E. Strand, "Attenuation and Scatter Correction in SPECT for Sources in a Nonhomogeneous Object: A Monte Carlo Study", *J.Nucl.Med.*, vol. 32, pp. 1278–1284, 1991.

[85] M. Ljungberg, S. E. Strand and M. A. King, *Monte Carlo Calculations in Nuclear Medicine*, IOP Publishing, Bristol, UK, 1998.

[86] V. J. Lowe, K. L. Greer, M. W. Hanson, R. J. Jaszczak and R. E. Coleman, "Cardiac phantom evaluation of simultaneously acquired dual-isotope rest Thallium-201/stress Technetium-99m SPECT", *J. Nucl. Med.*, vol. 34, no. 11, pp. 1998–2006, 1998.

[87] I. Lux and L. Koblinger, *Monte Carlo particle transport methods: neutron and photon calculations*, CRC-press, 1991.

[88] S. H. Manglos, D. A. Bassano, F. D. Thomas and Z. D. Grossman, "Imaging of the Human Torso Using Cone-Beam Transmission CT Implemented on a Rotating Gamma Camera", *J. Nucl. Med.*, vol. 33, pp. 150–156, 1992.

[89] S. H. Manglos, C. E. Floyd, R. J. Jaszczak, K. L. Greer, C. C. Harris and R. E. Coleman, "Experimentally measured scatter fractions and energy spectra as a test of Monte Carlo simulations", *Phys.Med.Biol.*, vol. 32, pp. 335–343, 1987.

[90] C. E. Metz, F. B. Atkins and R. N. Beck, "The geometric transfer function component for scintillation camera collimators with straight parallel holes", *Phys.Med.Biol.*, vol. 25, pp. 1059–1070, 1980.

[91] T. R. Miller and J. W. Wallis, "Clinically Important Characteristics of Maximum Likelihood Reconstruction", *J.Nucl.Med.*, vol. 33, pp. 1678–1684, 1992.

[92] S. C. Moore, R. J. English, C. Syravanh, D. E. Tow, R. E. Zimmerman, K. H. Chan and M. F. Kijewski, "Simultaneous Tc-99m/Tl-201 imaging using energy-based estimation of the spatial distributions of contaminant photons", *IEEETNS*, vol. 42, no. 4, pp. 1189–1195, 1995.

[93] S. C. Moore, R. E. Zimmerman, K. H. Chan, R. J. English and M. F. Kijewski, "Experimental and Monte Carlo characterization of spectral and spatial distribution of lead X-rays", *Proc. J. Nucl. Med.*, vol. 35, no. 5, p. 61P, 1994.

[94] M. Nakamura, K. Takeda, T. Ichihara, N. Motomura, H. Shimizu, Y. Saito, Y. Nomura, N. Isaka, T. Konishi and T. Nakano, "Feasibility of simultaneous stress Tc-99m/rest Tl-201 dual-isotope myocardial perfusion SPECT in the detection of coronary disease", *J. Nucl. Med.*, vol. 40, pp. 895–903, 1999.

[95] J. Narula, M. S. Dawson, B. K. Singh, A. Amanullah, E. R. Acio, F. A. Chaudhry, R. B. Arani and A. E. Iskandrian, "Noninvasive characterization of stunned, hibernating, remodeled and nonviable myocardium in ischemic cardiomyopathy.", *J. Am. Coll. Cardiol.*, vol. 36, pp. 1913–9, 2000.

[96] W. R. Nelson, H. Hiayama and D. W. O. Rogers, "The EGS4 code system", *Stanford Linear Accelerator Center Report SLAC-265*, 1985.

[97] J. Nuyts, *Quantification of SPECT images: simulation, scatter correction, reconstruction and automated analysis*, Ph.D. thesis, Catholic University of Leuven, 1991.

[98] M. K. O'Conner, "Evaluation of motion-correction techniques in cardiac SPECT", *J. Nucl. Med.*, vol. 41, p. 1298, 2000.

[99] J. M. Ollinger, "Model-based scatter correction for fully 3D PET", *Phys. Med. Biol.*, vol. 41, pp. 153–176, 1996.

[100] R. C. De La Pena, L. Ketonen and J. Villaneuve-Meyer, "Imaging of brain tumors in AIDS patients by means of dual-isotope thallium-201 and technetium-99m sestamibi single-photon emission tomography", *Eur. J. Nucl. Med.*, vol. 25, no. 10, pp. 1404–11, 1998.

[101] J. Peter, M. P. Tornai and R. J. Jaszczak, "Analytical versus voxelized phantom representation for Monte Carlo simulation in radiological imaging.", *IEEE Trans. Med. Imaging*, vol. 19, pp. 556–64, 2000.

[102] D. E. Raeside, "Monte Carlo principles and applications", *Phys. Med. Biol.*, vol. 21, no. 2, pp. 181–197, 1976.

[103] W. Rafflenbeul and M. Riedel, "Update on cardiac catheterization and coronary arteriography.", *Curr. Opin. Cardiol.*, vol. 8, pp. 572–80, 1993.

[104] T. A. Riauka and Z. W. Gortel, "Photon Propagation and Detection in Single Photon Emission Computed Tomography - An Analytical Approach", *Med.Phys.*, vol. 21, pp. 1311–1321, 1994.

[105] T. A. Riauka, H.R. Hooper and Z. W. Gortel, "Experimental and Numerical Investigation of the 3D SPECT Photon Detection Kernel for Non-Uniform Attenuating Media", *Phys.Med.Biol.*, vol. 41, pp. 1167–1189, 1996.

[106] H. Rief, "Generalized Monte Carlo perturbation algorithms for correlated sampling and a second-order Taylor series approach", *Ann. Nucl. Energy*, vol. 11, no. 9, pp. 455–476, 1984.

[107] L. A. Shepp and Y. Vardi, "Maximum likelihood Reconstruction for emission tomography", *IEEE Trans.Med.Im.*, vol. 1, pp. 113–122, 1982.

[108] H. J. Siebelink, D. Natale, A. J. Sinusas and F. J. Wackers, "Quantitative comparison of single-photon emission computed tomographic imaging for reversibility of defects", *J. Nucl. Cardiol.*, vol. 3, no. 6, pp. 483–493, 1996.

[109] E. T. P. Slijpen, H. W. A. M. de Jong and F. J. Beekman, "Utrecht Monte Carlo System for SPECT, Tech. Report 99-1", *Nuclear Medicine Physics Group, Utrecht University Hospital*, 1999.

[110] J. A. Sorenson and M. E. Phelps, *Physics in Nuclear Medicine*, The Saunders Company, 1987.

[111] J. Spanier and E. M. Gerbard, *Monte Carlo Principles and Neutron Transport Problems*, Addison-Wesley, 1969.

[112] R. Suneja and J. M. Hodgson, "Imaging in the catheterization laboratory.", *Curr. Opin. Cardiol.*, vol. 6, pp. 978–84, 1991.

[113] P. Tan, D. L. Bailey, S. R. Meikle, S. Eberl, R. R. Fulton and B. F. Hutton., "A scanning line source for simultaneous emission and transmission measurements in SPECT.", *J. Nucl. Med.*, vol. 34, pp. 1752–1759, 1993.

[114] B. M. W. Tsui, *Collimator design, properties and charateristics. In* The Scintillation Camera G. H. Simmons, The Society of Nuclear Medicine, New York, 1988.

[115] B. M. W. Tsui and G. T. Gullberg, "The geometric transfer function for cone and fan beam colllimators", *Phys.Med.Biol.*, vol. 35, pp. 81–93, 1990.

[116] B. M. W. Tsui, X. D. Zhao, G. K. Gregoriou, D. S. Lalush, E. C. Frey, R. E. Johnston and W. H. McCartney, "Quantitative Cardiac SPECT Reconstruction with Reduced Image Degradation Due to Patient Anatomy", *IEEE Trans Nuclear Science*, vol. 41, no. 6, pp. 2838–2844, 1994.

[117] B. M. W. Tsui, X. D. Zhao, G. K. Gregouri, D. S. Lalush, E. C. Frey, R. E. Johston and W. H. McCartney, "Quantitative cardiac SPECT reconstruction with reduced image degradation due to patient anatomy", *IEEE Trans.Nucl.Sci.*, vol. 41, pp. 2838–2844, 1994.

[118] C. H. Tung and G. T. Gullberg, "A Simulation of Emission and Transmission Noise Propagation in Cardiac SPECT Imaging with Nonuniform Attenuation Correction", *Med. Phys.*, vol. 21, no. 10, pp. 1565–1576, 1994.

[119] F. J. Wackers, D. S. Berman, J. Maddahi, D. D. Watson, G. A. Beller, H. W. Strauss C. A. Boucher, M. Picard, B. L. Holman and R. Fridrich et al., "Technetium-99m hexakis 2-methoxyisobutyl isonitrile: human biodistribution, dosimetry, safety, and preliminary comparison to thallium-201 for myocardial perfusion imaging.", *J. Nucl. Med.*, vol. 30, pp. 301–11, 1989.

[120] S. H. M. Walrand, L. R. van Elmbt and S. Pauwels, "Quantification in SPECT using an effective model of the scattering", *Phys.Med.Biol.*, vol. 39, pp. 719–734, 1994.

[121] H. Wang, R. J. Jaszczak and R. E. Coleman, "Solid Geometry-Based Object Model for Monte Carlo Simulated Emission and Transmission Tomographic Imaging Systems", *IEEE Trans.Med.Im.*, vol. 11, pp. 361–372, 1992.

[122] H. Wang, R. J. Jaszczak, J.W. McCormick, K. L. Greer and R. E. Coleman, "Experimental Evaluation of a Tellurium-123m Transmission source to determine Attenuation Maps for SPECT", *IEEE Trans.Nucl.Sci.*, vol. 42, no. 4, pp. 1214–1219, 1995.

[123] W. T. Wang, E. C. Frey and B. M. W. Tsui, "Parametrization of Pb X-ray contamination in simultaneous Tl-201 and Tc-99m dual isotope SPECT", *Conference Record of 1999 IEEE Nuclear Science Symposium and Medical Imaging Conference, Seattle*, 1999.

[124] H. Weinstein, M. A. King, C. P. Reinhardt, B. A. McSherry and J. A. Leppo, "A method of simultaneous dual-radionuclide cardiac imaging with Technetium 99m and Thallium 201. I: Analysis of interradionuclide crossover and validation in phantoms", *J. Nucl. Card.*, vol. 1, no. 1, pp. 39–51, 1994.

[125] R. G. Wells, A. Celler and R. Harrop, "Analytical Calculation of Photon Distributions in SPECT", *IEEE Trans.Nucl.Sci.*, vol. 45, pp. 3202–3214, 1998.

[126] H. Zaidi, "Relevance of accurate Monte Carlo modeling in nuclear medical imaging", *Med. Phys.*, vol. 26, no. 4, pp. 574–608, 1999.

[127] X. Zhang, X. J. Liu, Q. Wu, R. Shi, R. Gao, Y. Liu, S. Hu Y. Tian, S. Guo and W. Fang, "Clinical outcome of patients with previous myocardial infarction and left ventricular dysfunction assessed with myocardial (99m)tc-mibi spect and (18)f-fdg pet.", *J. Nucl. Med.*, vol. 42, pp. 1166–73, 2001.

[128] G. Zubal and C. Harrel, *Voxel Based Calculation of Nuclear Medicine Images and Applied Variance Reduction Techniques*, In: Information Processing in Medical Imaging, A.C.F. Colchester and D.J. Hawkes eds, Lecture Notes in Computer Science 511, Springer Verlag, Berlin, pp. 23-33, 1991.

Samenvatting

Met Single Photon Emission Tomography (SPECT) kunnen 2D projecties van de verdeling van een radio-actieve stof (die fotonen uitzendt) in een patiënt gereconstrueerd worden tot een 3D beeld. Een dergelijk 3D SPECT beeld kan bijvoorbeeld worden gebruikt om de plaatselijke doorbloeding en levensvatbaarheid van de hartspier te bepalen, maar ook om de bewegingen van de hartspier te meten. Om een beeld te krijgen van de levensvatbaarheid van de hartspier wordt in het algemeen een scan gemaakt van het hart in rust en na inspanning. Hiervoor wordt een radio-actieve stof ingespoten zoals Tc-99m (technetium) of Tl-201 (thallium). Elke scan duurt zo'n 20 tot 30 minuten.

Recentelijk werd een nieuw scanprotocol voorgesteld waarbij Tc-99m wordt gebruikt voor het inspanningsbeeld en Tl-201 voor de scan van het hart in rust, zodat rust en inspanningsbeeld tegelijkertijd opgenomen kunnen worden (*Simultane rust Tl-201/ inspanning Tc-99m dual-isotope myocard SPECT*). Hiertoe wordt eerst Tl-201 toegediend in rust, vervolgens levert de patient inspanning en wordt Tc-99m ingespoten, waarna simultaan een SPECT scan gemaakt kan worden van de Tl-201 en de Tc-99m verdeling. De voordelen van dit protocol in vergelijking met het huidige zijn indrukwekkend: de totale onderzoekstijd wordt bijna gehalveerd wat de wachtlijsten voor hartpatiënten verkort en een aanzienlijke kostenbesparing met zich mee brengt. Het feit dat het rust en inspanningsbeeld tegelijkertijd opgenomen worden voorkomt tevens dat deze beelden niet identiek georiënteerd zijn, iets wat nu een bron van foutieve diagnose kan zijn.

In het algemeen wordt de kwaliteit van de gereconstrueerde SPECT beelden negatief beinvloedt door diverse fysische factoren, zoals verzwakking en verstrooiing van de uitgezonden fotonen en de beperkte beeldscherpte van de SPECT camera's. Correctie hiervoor verbetert beeldkenmerken zoals contrast, kwantitatieve nauwkeurigheid en ruisniveau. Naast deze factoren speelt in simultane Tc-99m/Tl-201 dual-isotope SPECT ook *down-scatter* een rol; Fotonen uitgezonden door het radio-actieve Tc-99m verliezen energie door verstrooiing in de patiënt zodat hun energie overeenkomt met die van Tl-201 fotonen en het Tl-201 beeld verstoord wordt. Populair gezegd loopt het Tc-99m inspanningsbeeld als het ware door in het Tl-201 rustbeeld. Dit kan leiden tot flinke positiegerelateerde overschatting van de Tl-201 verdeling in het hart, en vermindering van het contrast van kleine defecten in het Tl-201 beeld.

Een nauwkeurige en algemeen toepasbare manier om te corrigeren voor fotonverzwakking, fotonverstrooiing, de beperkte beeldscherpte en down-scatter is het gebruik van een fysisch model tijdens de reconstructie, dat al deze factoren beschrijft. Dit fysische model voorspelt welke 2D projecties horen bij een bekende 3D verdeling van de radio-actieve stof. Hiervoor worden momenteel analytische modellen gebruikt welke het grote voordeel hebben dat ze weinig computertijd vereisen om tot een oplossing te komen. Deze modellen werken goed in lichaamsdelen met relatief uniforme dichtheden (zoals het hoofd) en in situaties waarin fotonen een wat hogere energie hebben (zoals fotonen uitgezonden door Tc-99m). Ze leveren echter een stuk minder goede resultaten wanneer

niet-uniforme dichtheden een grote rol spelen zoals in de thorax, wanneer de fotonen een wat lagere energie hebben zoals met Tl-201 het geval is, of wanneer gedetecteerde fotonen veel energie hebben verloren zoals in down-scatter.

In **hoofdstuk 2** wordt de invloed op 2D SPECT projecties onderzocht van *backscatter*, dat zijn fotonen die verstrooien via materiaal dat zich achter de radio-actieve stof bevindt. Uit dit onderzoek blijkt o.a. dat *backscatter* een grote rol speelt in *down-scatter* van Tc-99m fotonen in Tl-201 projecties (belangrijk in simultane Tc-99m/Tl-201 dual-isotope SPECT). Daarnaast blijkt backscatter ook een sigificante rol te spelen in Tl-201 SPECT. Omdat backscatter moeilijk te berekenen is met analytische modellen, zijn deze modellen niet of minder geschikt om te gebruiken voor down-scatter correctieberekeningen dan wel Tl-201 SPECT reconstructie. Om deze reden, en omdat een algemeen verstrooiingsmodel zeer bruikbaar is voor nauwkeurige SPECT reconstructies, is gekozen om Monte Carlo simulaties voor de modellering te gaan gebruiken. Monte Carlo simulatie is een stochastische manier (d.w.z. met gebruik van willekeurige of *random* getallen) om fotonpaden te bepalen en zo nauwkeurig de 2D projecties te voorspellen. Een groot nadeel van Monte Carlo simulatie is dat het veel rekentijd kost om tot een goed resultaat te komen. Dit is een van de belangrijkste redenen waarom het tot nu toe niet klinisch gebruikt is. In dit proefschrift wordt beschreven hoe Monte Carlo simulatie versneld kan worden door de stochastische methoden op enkele plekken te vervangen door analytische rekenmethoden.

In **hoofdstuk 3** wordt uitgelegd hoe fotonverstrooiing in SPECT snel en bijna exact bepaald kan worden door het resultaat dat berekend met een analytisch model, gebaseerd op een uniform dichtheidsverdeling in het lichaam, te transformeren tot de fotonverstrooiing welke het gevolg is van een realistische niet-uniforme dichtheidsverdeling zoals de thorax. Dit gebeurt door middel van twee korte Monte Carlo simulaties. Ruistoename tijdens de transformatie wordt sterk onderdrukt door (i) de twee Monte Carlo simulaties te correleren, en (ii) doordat een analytisch model gebruikt wordt in plaats van een stochastich model om de invloed van de cameraresolutie op het resultaat te berekenen *(Convolution-based Forced Detection (CFD))*. Door het gebruik van deze twee versnellingsmethoden kan de transformatie ruim honderd keer sneller worden uitgevoerd. Het gebruik van *alleen* CFD zorgt ervoor dat Monte Carlo simulatie van fotonverstrooiing zo'n 50 keer sneller een bijna ruisvrij resultaat levert dan standaard Monte Carlo simulatie (**hoofdstuk 4**).

De verbetering van simultane Tc-99m/Tl-201 dual-isotope SPECT reconstructie is het hoofdthema van het tweede deel van het proefschrift. Om zulke SPECT beelden nauwkeurig te reconstrueren is het nodig om te corrigeren voor down-scatter van fotonen afkomstig van Tc-99m in het Tl-201 beeld. Correctie is mogelijk door de Tc-99m down-scatter projecties te berekenen en mee te nemen tijdens de reconstructie van het Tl-201 beeld.

In **hoofdstuk 5** wordt een methode voorgesteld om Monte Carlo simulatie van down-scatter te versnellen (*Rotation-based Monte Carlo (RMC)*). De versnelling wordt bereikt door de down-scatter voor slechts een paar projecties te berekenen van de in totaal tientallen projecties waaruit een SPECT-studie bestaat. Dit resultaat kan dan efficient gebruikt worden om de down-scatter in de andere projecties te bepalen, wat veel rekentijd bespaart.

Gecombineerd met CFD versnelt RMC de Monte Carlo berekeningen van down-scatter met een factor van duizend, zonder dat hierbij de nauwkeurigheid significant afneemt.

Naast de verstrooiing van Tc-99m fotonen in het lichaam wordt down-scatter ook voor een belangrijk veroorzaakt door de emissie van Röntgen-stralen uit lood. Deze Röntgen-stralen ontstaan wanneer Tc-99m fotonen worden geabsorbeerd in het collimator lood, en hebben een energie die vergelijkbaar is met de energie van Tl-201 fotonen. In **hoofdstuk 6** wordt beschreven hoe de verdeling van deze Röntgen-straling berekend kan worden door een uitbreiding van de RMC-methode. In dit hoofdstuk is verder een zeer goede overeenkomst aangetoond tussen gemeten down-scatter projecties en down-scatter projecties berekend met de RMC-methode.

In **hoofstuk 7** wordt beschreven hoe de versnelde Monte Carlo methode gebruikt kan worden om te corrigeren voor down-scatter in simultane Tc-99m/Tl-201 dual-isotope SPECT; een bijna perfecte correctie kan worden bereikt voor de positie-gerelateerde activiteitsoverschatting en contrastvermindering in het Tl-201 beeld. Down-scatter veroorzaakt verder nog een verhoogd ruisniveau in het Tl-201 beeld, waarvoor gecorrigeerd kan worden door de SPECT-scantijd iets te verlengen en de toegediende Tl-201 en Tc-99m doses iets aan te passen.

Dit proefschrift sluit af met de conclusie dat simultane dual-isotope SPECT de realisatie van een 'one-stop shop' hart-afbeeldings techniek een stap dichterbij brengt. Zo'n 'one-stop shop' techniek maakt een nauwkeurigere diagnose mogelijk met verminderde kosten en verminderde belasting voor de patient.

Publications

Full papers in international journals.

H. W. A. M. de Jong, F. J. Beekman, M. Ljungberg and P. P. van Rijk, *The influence of backscatter on Tc-99m and Tl-201 line source responses*, Physics in Medicine and Biology, Vol. 44, pp. 665-679, 1999

H. W. A. M. de Jong, E. T. P. Slijpen and F. J. Beekman, *Acceleration of Monte Carlo SPECT simulation using Convolution-based Forced Detection*, IEEE Transactions on Nuclear Science, Vol. 48, pp. 58-64, 2001

H. W. A. M. de Jong and F. J. Beekman, *Rapid SPECT simulation of down-scatter in non-uniform media*, Physics in Medicine and Biology, Vol. 46, pp. 621 - 635, 2001

H. W. A. M. de Jong, W. T. Wang, E. C. Frey, M. A. Viergever and F. J. Beekman, *Fast Monte Carlo simulation of SPECT down-scatter including gamma interactions with crystal and lead*, submitted

H. W. A. M. de Jong, F. J. Beekman, M. A. Viergever, P. P. van Rijk, *Simultaneous Tc-99m/Tl-201 dual-isotope SPECT with Monte Carlo-based downscatter correction*, submitted

H. W. A. M. de Jong, M. Ljungberg F. J. Beekman, *Validation of a fast simulator for clinical SPECT simulation*, submitted

F. J. Beekman, H. W. A. M. de Jong and E. T. P. Slijpen, *Efficient SPECT Scatter Response Estimation in Non-Uniform Media using Correlated Monte Carlo Simulations*, Physics in Medicine and Biology, Vol. 44, pp. N183-N192, 1999

F. J. Beekman, H. W. A. M. de Jong and E. T. P. Slijpen, *Efficient SPECT Scatter Response Estimation in Non-Uniform Media using Correlated Monte Carlo Simulations*, Physics in Medicine and Biology, Vol. 44, pp. N183-N192, 1999

F. J. Beekman, E. T. P. Slijpen, H. W. A. M. de Jong, M. A. Viergever, *Estimation of the Depth Dependent component of Point Spread Function of SPECT*, Medical Physics, Vol. 26, pp. 2311-2322, 1999

F. J. Beekman, H. W. A. M. de Jong, S. van Geloven,*Efficient Monte Carlo based Fully 3D SPECT Reconstruction*, submitted

Dankwoord

Na de vorige 8 inleidende hoofdstukken ben ik nu aangekomen bij het belangrijkste gedeelte. Als ik terugkijk op de afgelopen ruim 4 jaren denk ik in eerste instantie niet direct aan de inhoud van mijn onderzoek maar eerder aan de mensen met wie ik heb mogen samenwerken en samenleven. Het feit dat ik de periode als succesvol beschouw komt dan ook voor het grootste deel door de mensen die ik hier de revue laat passeren. Ik wil daarom beginnen iedereen te bedanken met wie ik de afgelopen jaren heb samengewerkt op het UMC of daarbuiten.

Mijn begeleider Freek is de grote accelerator achter dit boekje. Altijd bereid om concept-concept stukken snel te corrigeren, had altijd volop ideëen, liet me gebruik maken van zijn uitgebreide internationale netwerk (wie kende Freek niet?) en regelde vanalles voor me waaronder een perfecte werkplek en een buitenlandse stage. Never a dull moment with Freek. Freek bedankt voor alles! Naast Freek waren er promotor Max Viergever en tweede copromotor Peter van Rijk die ik graag wil bedanken voor het feit dat ze een oogje in het zeil gehouden hebben. Max bedankt voor je opbouwende commentaar op mijn werk. Peter bedankt voor het uitstekend faciliteren van dit onderzoek.

Naast deze officiële begeleiders heb ik erg veel steun gehad aan mijn collega's uit de SPECT groep. Eerst waren daar Chris en Eddy: Chris was bijna vier jaar lang mijn maatje op het ziekenhuis. Chris, waar ben je!? Drie maanden na aanvang van mijn onderzoek werd ik veroordeeld tot de Researchkamer waar ook Eddy Slijpen zich had genesteld. Eddy maakte met zijn domme grappen de Researchkamer zowaar gezellig, en zonder zijn C++ enthousiasme was UMCS nimmer-nooit-niet van de grond gekomen. In de korte tijd dat Hans van den Heuvel onderzoek deed, heeft hij veel tijd gestoken in het installeren van Linux op mijn werkplek. Hans, ik heb er nog steeds erg veel plezier van! De lege plek die Chris achterliet werd ingevuld door Sander. Sander was niet alleen een uitstekend computer-expert, je kan er ook geweldig mee in de kroeg hangen of bijvoorbeeld een straat-dansfestijn mee organiseren. Sander, succes met je nieuwe carrierestappen, ennuh, je bent nog niet van me af! Mark wil ik bedanken voor de olijke noot, een onbekende hoeveelheid bijdehande grappen en uitstekend werk.

Dit bovenstaande SPECT groepje was ingebed in de afdeling Nucleaire Geneeskunde. Van deze afdeling wil ik gaarne de artsen bedanken: John de Klerk, Hans van Isselt, Jaap Kuyvenhoven en Henk Stevens maar zeker ook Maarten-Jan Cramer van het Hart-Long Centrum Utrecht voor getoond enthousiastme en klinisch commentaar op mijn werk. Voor de vele, soms dagenlang durende experimenten was ik afhankelijk van een uitstekende club laboratorium medewerkers: Don, Marian, Ursula, Ibolya, Sander, Inge en Henny bedankt voor het prepareren van al die minuscule bronnetjes, slangetjes, spuiten en fantomen! Ook aan de technische kant van deze experimenten ging natuurlijk van alles mis. Gelukkig kon ik rekenen op Bert, Oane en Wim. Terwijl we stonden te paniekeren omdat de scanner het begaf in het weekend na een nacht meten, hield Bert het hoofd koel en loste

het probleem telefonisch op. Heren, hartelijk dank voor uw steun! De Medisch Nucleair Werkers alsmede het administratieve personeel wil ik bedanken voor de hulp en de ruimte die me geboden werd om mijn experimenten te volbrengen.

Al zat de SPECT groep op de afdeling Nucleaire Geneeskunde, het groepje hoorde ook wel weer heel erg thuis bij het Image Sciences Institute. Aangezien ik maar een aantal maanden in het R-lab heb doorgebracht alvorens heengezonden te worden naar de Researchkamer ken ik de meeste ISI-collega's vooral via de frequente borrels en die waren over het algemeen erg gezellig! Van de ISI-collega's wil ik speciaal bedanken voor geleverde diensten: Josien, Clemens, Wilbert, Bram, Gerard, Koen, Margo en Sandra.

Many people made the months I stayed in Chapel Hill, North Carolina a fantastic time. I want to thank Eric Frey and Benjamin Tsui for their overwhelming hospitality and their excellent supervision over my research. I hope we can cooperate for many more years. I also want to thank the other students, in particularly Wen-Tun Wang for simulation support. Furthermore, I seldom did meet someone as relaxed as my roommate Brian Rucker. Brian thanks once more for your company and care. Hope you are doing fine.

Naast het werk op het ziekenhuis was er ook nog 'af en toe' tijd voor wat ontspanning: Ik wil mijn vrienden Jochen, Iemy en Olaf bedanken voor de sportieve tennis-ski-zeil-uitgaans activiteiten. Marielle bedankt voor de gezelligheid en het fantastische kunstwerk wat je gemaakt hebt van de omslag van dit boekje. Daarnaast zijn daar de vele huisgenoten die ik gehad heb in het AZU-huis in de Biltstraat (Berend en Birgit!) en huize Kopzorg in de Korte Lauwerstraat, ik zou echt niet meer weten hoeveel dat er zijn (meer dan 50), maar ze zijn verantwoordelijk voor een groot deel van mijn lol in Utrecht. De leden van het fysisch genootschap Nwyvre hebben er voor gezorgd dat ik Eindhoven nog steeds als uiterst gezellige thuishaven kan beschouwen. Voor de hechte vriendschap en voor de muzikale omlijsting van de afgelopen jaren wil ik graag mijn kameraden DJ Camiel en DJ Sjef Pils bedanken. Tenslotte wil ik mijn liefste zus Marieke alsmede mijn lieve ouders bedanken voor de altijd aanwezige en onvoorwaardelijke steun. En ja, het allerliefstelaatste plaatsje is gereserveerd voor mijn Julie ...